UMBC

DISSERTATION APPROVAL SHEET

Title of Dissertation: Improving Air Quality Forecasts of Ozone and Particulate Matter: Modeling-Observation Integrated Study

Name of Candidate: Zhifeng Yang

Doctor of Philosophy, 2021

Graduate Program: Atmospheric Physics

Dissertation and Abstract Approved:

Belay Demoz

Belay Demoz

Professor

Department of Physics - Atmospheric Physics

7/29/2021 | 9:30:01 AM EDT

NOTE: *The Approval Sheet with the original signature must accompany the thesis or dissertation. No terminal punctuation is to be used.

ABSTRACT

Title of dissertation: IMPROVING AIR QUALITY FORECASTS OF OZONE AND PARTICULATE MATTER: MODELING-OBSERVATION INTEGRATED STUDY

Zhifeng Yang, Ph.D., 2021

Dissertation directed by: Dr. Belay Demoz

Professor in the Department of Physics

Director of the Joint Center for Earth Systems Technology

This study investigates the dynamical influence of CB on the local O_3 pollution through weather modeling. WRF-Chem was employed to simulate the O_3 production and transportation near CB. One baseline experiment and one sensitivity experiment were carried out by changing the surface types over CB from water to land (loam). Due to the presence of CB, the O_3 mixing ratio increased during both day and night, resulting from bay breeze circulation. In addition, the bay breeze transported O_3 from CB to the western shore and increased the O_3 mixing ratio over the downwind regions of onshore winds. The modeled surface O_3 concentration mean increased by up to 10 % at night and 5 % during the day because of the bay dynamics effect. O_3 was produced, mixed and diluted up to 1.2 km over the northern CB in the day, while that height dropped to 0.4 km at night.

The integration of observations and models can improve air quality forecasts (in particular O_3 and particulate matter (PM)) for wildfires. This work is on a Canadian fire event on 6-12 June 2015 that impacted the air quality in the Mid-Atlantic region in the U.S. We use the WRF-Chem model and various measurements from both ground-based and spaceborne observations, including the U.S. Environmental Protection Agency (EPA) AirNow data, the National Aeronautics and Space Administration (NASA) operated TROPospheric OZone lidar (TROPOZ), wind radar, ceilometer, Moderate Resolution Imaging Spectroradiometer (MODIS), Cloud-Aerosol Lidar with Orthogonal Polarization (CALIOP). The model captured the O_3 diurnal variation and PM spatial distribution when comparing with EPA AirNow and MODIS/CALIOP observations, respectively. Wildfire smoke was transported from central Canada through Lake Michigan, passing the Ohio River Valley and down to the Baltimore-Washington D.C. metropolis.

This study uses the WRF-Chem/DART chemical transport forecasting/data assimilation system, to assimilate EPA AirNow surface and ground-based lidar vertical profile O_3 observations over the eastern U.S. to study the impact of smoke intrusion from a Canadian wildfire event in June 2015. The positive systematic bias of the operational surface O_3 forecasts motivated this work. To verify results, we use ozonesonde vertical profile observations.

IMPROVING AIR QUALITY FORECASTS OF OZONE AND PARTICULATE MATTER: MODELING-OBSERVATION INTEGRATED STUDY

by

Zhifeng Yang

Dissertation submitted to the Faculty of the Graduate School of the University of Maryland, Baltimore County in partial fulfillment of the requirements for the degree of Doctor of Philosophy

2021

Advisory Committee:

Dr. Belay Demoz, Chair, Professor in the Department of Physics and Director of the Joint Center for Earth Systems Technology

Dr. Pengwang Zhai, Associate Professor and Graduate Program Director in the Department of Physics, Joint Center for Earth Systems Technology

Dr. Ruben Delgado, Assistant Research Professor in the Department of Physics, Joint Center for Earth Systems Technology

Dr. Andrew Tangborn, Associate Research Professor in the Department of Physics, Joint Center for Earth Systems Technology

Dr. Pius Lee, Scientist at National Oceanic and Atmospheric Administration

Dr. John T. Sullivan, Scientist at National Aeronautics and Space Administration, Goddard Space Flight Center

Acknowledgements

Throughout the preparation and writing of my dissertation, I have received a great deal of support and assistance. First and foremost, I would like to thank my academic advisor, Dr. Belay Demoz who showed me his generosity in supporting my research. He provided me with tons of opportunities to let me explore my research topics and reach out to other scientists who could help on my dissertation. I also want to thank Dr. Milt Halem for supporting me financially. Dr. Halem showed me the enthusiasm to do research. I would like to thank my committee, Dr. Pengwang Zhai, Dr. Ruben Delgado, Dr. Andrew Tangborn, Dr. Pius Lee, Dr. John T. Sullivan, especially Dr. Pius Lee and Dr. John T. Sullivan for spending extra time on serving as readers of my dissertation. I would like to acknowledge Dr. Arthur Mizzi and Dr. Jeffery Anderson (NCAR/DAReS) for teaching me the data assimilation techniques. Dr. Nancy Collins (NCAR/DEReS), Dr. Tim Hoar (NCAR/DEReS), and Dr. Mohamad El Gharamti (NCAR/DEReS) for assistance on learning DART. I also thank Dr. Jonathnan Poterjoy and Dr. Eugenia Kalnay for their help in guiding me on understanding the fundamental knowledge of data assimilation. I want to thank Dr. Jason Kestner, Dr. Vanderlei Martins, Yanhua Shih for teaching me the physics classes. My classmates have been helping with my early learning on courses. Finally, I would like to thank my wife Xiaofang Xue for her support in the family.

This work was partly funded by the National Science Foundation award (AGS- 1503563) to the University of Maryland, Baltimore County and by a grant from the Maryland Department of Environment (MDE) to the University of Maryland, Baltimore County. This study was also partially funded by the National Oceanic and Atmospheric Administration – Cooperative Science Center for Atmospheric Sciences and Meteorology (NOAA-NCAS-M) and Center for Earth System Sciences and Remote Sensing Technologies (NOAA-CESSRST) under the Cooperative

Agreement Grants #NA16SEC4810006 and #NA16SEC4810008, respectively. In addition, NCAR Advanced Study Program Graduate Visitor Program partially funded this work. We also acknowledge the AirNow program for providing the surface O_3 observations.

Table of Contents

List of Tables

List of Figures

550 nm. Panels (g-i): WRF-Chem simulated surface $PM_{2.5}$ mass concentration (Ex2). The pink rectangles indicate where the smoke front is. Panels (j-l): CALIOP-derived vertical feature mask. Panels (m-o): WRF-Chem simulated $PM_{2.5}$ mass concentration vertical cross section along the CALIPSO ground track. The inset on the upper right shows the CALIPSO ground track (red curve).

Fig. 3.4 915 MHz wind radar and WRF-Chem simulated horizontal wind speed and direction vertical profiles at three sites on 8-12 June 2015. The top row is the wind radar observation. The bottom row is the WRF-Chem simulation. (a) and (e), Piney Run; (b) and (f), Beltsville; (c) and (g), Horn Point; (d), wind difference between Beltsville and Horn Point; (h), three site locations on the map.

Fig. 3.5 Diurnal variations of the surface O_3 mixing ratio of EPA AirNow, TROPOZ and WRF-Chem simulation at sites: (a) Hagerstown (rural), (b) Edgewood (coastal), and (c) Beltsville (suburban) on 12 June, 2015. The red shaded areas indicate standard deviations of the WRF-Chem simulation; and surface O_3 concentration daily averages are denoted as dashed lines. The location of the station is indicated by a red dot on a map in the upper right corner. Pearson correlation coefficients and RMSEs between EPA AirNow and WRF-Chem simulation are provided.

Fig. 3.6 Time series of ceilometer CL51 aerosol total attenuated backscatter at 910 nm (a-c) and WRF-Chem $PM_{2.5}$ mass concentration (d-f) on 10-12 June 2015. The pink curve is denoted as the model simulated PBLH. The upper right inserted map shows the location of the site (red dot).

Fig. 3.7 O_3 mixing ratio vertical profiles from TROPOZ and WRF-Chem model on 12 June. (a) TROPOZ O_3 mixing ratio vertical profile time series and the WRF-Chem simulated PBLH (pink

standard deviation are shown as a red thick curve and shade, respectively. The upper right inserted map shows the location of the Beltsville site (red dot).

List of Abbreviations and Math Symbols

Abbreviations

ACM2	Asymmetrical Convective Model version 2
AOD/AOT	Aerosol Optical Depth/Thickness
ASOS CL31	Automated Surface Observing System Ceilometer 31
BAQS	Border Air Quality and meteorology Study
BC	Black Carbon
CALIOP	Cloud-Aerosol Lidar with Orthogonal Polarization
CALIPSO	Cloud-Aerosol Lidar and Infrared Pathfinder Satellite Observation
CB	the Chesapeake Bay
CBM-Z	Carbon-Bond Mechanism Version Z
CMAQ	Community Multiscale Air Quality Modeling System
CTM	Chemical Transport Model
DA	Data Assimilation
DART	Data Assimilation Research Testbed
D.C.	District of Columbia

DIAL	Differential Absorption Lidar
DISCOVER-AQ-2011	Deriving Information on Surface Conditions from COlumn and VERtically Resolved Observations Relevant to Air Quality 2011
EAKF	Ensemble Adjustment Kalman Filter
EnKF	Ensemble Kalman filter
EPA	Environmental Protection Agency
EST	Eastern Standard Time
FINN	Fire INventory from NCAR
FIREX	Fire Influence on Regional and Global Environments Experiment
GEOS-CHEM	Goddard Earth Observing System – Chemistry model
GSFC	Goddard Space Flight Center
IPCC	Intergovernmental Panel on Climate Change
KF	Kalman Filter
LMOS	Lake Michigan Ozone Study
MD	Maryland state
MM5	fifth-generation Pennsylvania State University–National Center for Atmospheric Research Mesoscale Model
MODIS	Moderate Resolution Imaging Spectroradiometer

MOSAIC	Model for Simulating Aerosol Interactions and Chemistry
MOZART-4	Model for Ozone and Related chemical Tracers, version 4
MPLnet	Micro-Pulse Lidar Network
MYJ	Mellor-Yamada-Janjic
NAAQS	National Ambient Air Quality Standards
NARR	Northern American Regional Reanalysis
NASA	National Aeronautics and Space Administration
NCAR	National Center for Atmospheric Research
NCEP	National Centers for Environmental Prediction
NEI2011	National Emission Inventory 2011
NMOCs	nitrogen oxides and non-methane organic carbons
NOAA	National Oceanic and Atmospheric Administration
O_3	Ozone
OC	Organic Carbon
OMI	Ozone Monitoring Instrument
OWLETS	Ozone Water-Land Environmental Transition Study
PBL(H)	Planetary Boundary Layer (Height)
PDF	Probability Density Function

PM	Particulate Matter
RAOB	RAwinsond Observation
RMSE	root-mean-square error
RO_2	organic peroxy radicals
ROI	radius of influence
RRTMG	Rapid Radiative Transfer Model for General Circulation Models
SST	Sea Surface Temperature
TEMPO	Tropospheric Emissions: Monitoring of Pollution
TKE	Turbulent Kinetic Energy
TOLNET	Tropospheric Ozone Lidar NETwork
USGS	United States Geological Survey
UTC	Coordinated Universal Time
VA	Virginia state
VOCs	Volatile organic compounds
WRF-Chem	Weather Research and Forecast model coupled with Chemistry package
WRFDA	WRF Data Assimilation
YSU	Yonsei University

Math Symbols

A	transition matrix
B	transition matrix
C	transition matrix
ε_e	error in estimate
ε_{est_t}	new estimate error
ε_m	error in measurement
E_t	current estimate
E_{t-1}	previous estimate
h	boundary layer height diagnosed using the critical R_B
H	transition matrix
k	von Karman constant
K	Kalman gain
K_m	momentum eddy diffusivity
M	measurement
P_0	initial process covariance matrix
P_{k_p}	predicted process covariance matrix
Q_k	process noise covariance matrix

R	measurement error matrix or sensor noise covariance matrix
u’	east-west velocity turbulent part
U_k	control variable matrix
v’	south-north velocity turbulent part
W_k	predicted state noise matrix
w_s	velocity scale
w’	vertical velocity turbulent part
X_0	initial state matrix
X_k	new state matrix
X_{k_p}	predicted state matrix
Y_k	measurement of the state
z	height above ground
Z_k	measurement noise or uncertainty
θ_v	virtual potential temperature

Chapter 1

Introduction, motivation, and objectives

1.1 Introduction

The air quality is both influenced by local and long-range transported pollutants. In the Mid-Atlantic region, the main air pollutants are ozone (O_3) and particulate matter (PM). The local pollutant source is the Chesapeake Bay (hereafter referred to as CB). The pollutants transported from outside are from the Ohio River Valley and Canadian wildfires. This study is to quantify the contribution of these two air pollutant sources to the local air pollution.

1.2 Local O_3 pollution

Tropospheric (ground-level or surface) O_3, has significant environmental and human health impacts. Long-term exposure to the high O_3 concentration air leads to serious health issues, such as irritating lungs, aggravating bronchitis, emphysema, and asthma (Lippmann 1991; Mudway and Kelly 2000; Forouzanfar et al., 2016). In order to mitigate surface pollution in the U.S., the Clean Air Act requires the Environmental Protection Agency (EPA) to set the National Ambient Air Quality Standards (NAAQS, Martineau and Novello 1997). The current NAAQS, in effect since 2015, sets an ambient 8-hour O_3 mixing ratio criterion of 70 parts per billion by volume (ppbv, NAAQS for O_3, 2015; Cooper et al., 2015). In particular, the ground-level O_3 mixing ratio over some coastal regions exceeds NAAQS relatively more frequently than other inland regions. Examples of such regions include CB (Loughner et al., 2014; Sullivan et al.,

2019), the Galveston Bay (Daum et al., 2004), the Great Lakes (Lyons and Cole 1976; Dye et al., 1995; Lyons et al., 1995; Brook et al., 2013), the Great Salt Lake (Blaylock et al., 2017). All these locations are in close proximity to water bodies surrounded by land, and related research is ongoing to investigate the causes for the exceedance of O_3 concentration (Sullivan et al., 2019; LMOS 2017 Study Team 2019). As a secondary pollutant, ground-level O_3 depends on its precursors, chemical reactions, and meteorological conditions (PROG 1997; Jenkin and Clemitshaw 2000; Karle et al., 2020). Understanding them helps to track O_3 pollution sources and sinks and is critical for improving the accuracy of O_3 pollution forecasting.

Field campaigns provide insights to physical and chemical processes in the atmosphere under a diverse set of meteorological conditions over the aforementioned locations. A number of campaigns have been conducted to investigate bay/lake effects on the local meteorology and air quality, e.g. Deriving Information on Surface Conditions from Column and Vertically Resolved Observations Relevant to Air Quality from 27 June to 31 July 2011 (DISCOVER-AQ), (Crawford and Pickering 2014), The Border Air Quality and Meteorology Study from 20 June to 10 July 2007 (BAQS-Met, Brook et al., 2013), the Ozone Water-Land Environmental Transition Study from 5 July to 3 August 2017 (OWLETS) and from 6 June to 6 July 2018 (OWLETS2, Sullivan et al., 2019), Lake Michigan Ozone Study (LMOS, Lyons and Cole 1976; Dye et al., 1995; LMOS 2017 Study Team 2019). Findings on the impacts of CB on O_3 from both dynamics and chemistry perspectives and a link to the bay/lake water body have also been suggested by these field campaign studies (Lyons and Cole 1976; Dye et al., 1995; Loughner et al., 2011; Foley et al., 2011; Brook et al., 2013; Blaylock et al., 2017; LMOS 2017 Study Team 2019).

One of the most important contributions in the previous studies is the role of dynamics originating from the local bay/lake and coastal circulations. The bay/lake dynamical effects

contributing to the local meteorology and air quality are: (1) the developing land/bay breeze and resulting diurnal dynamics that alters the near-shore meteorology through small scale circulations, e.g. the bay breeze yields high pressure over CB and low pressure inland nearby CB (Goldberg et al., 2014); (2) associated changes in cloud formation which in turn modifies the radiation environment thereby causing shielding for O_3 photolysis (Loughner et al., 2011), e.g. the presence of clear skies over CB and later development of cumulus clouds due to higher surface temperature and elevated boundary layer (Goldberg et al., 2014); (3) changes of vertical mixing of gases, associated with changes in plume updraft velocity over land compared to water, that impact O_3 concentration, e.g. the bay breeze developed during the late morning and early afternoon along the western shore of CB converged the pollutants (Loughner et al., 2014); and (4) modification of the inversion layer (strong inversion over land at night as opposed to over the bay/lake) and its impact on the dilution and venting of gases.

Most of these previous studies utilize observations from field campaigns to analyze the effects of the bay/lake and evaluate the model performance by comparing model results with observations (Goldberg et al., 2014; He et al., 2014; Loughner et al., 2011; 2014). To our knowledge, not many have taken advantage of recent model improvements, especially online coupling of meteorology and chemistry to specifically address the dynamical role of CB on the O_3 concentration.

Even though some previous reports have discussed the numerous possible dynamic and chemical processes that alter the near-shore pollution, they focus on the model resolution sensitivity and model performance evaluation (Anderson et al., 2014; Goldberg et al., 2014; He et al., 2014; Loughner et al., 2014; 2011; Flynn et al., 2016; Sullivan et al., 2019). Primary impacts among the dynamical processes are the development of breeze (bay and land) and the

differential sensible heating resulting in the land-bay horizontal temperature gradients. In shallow parts of the CB, the SST can change considerably even in the course of hours to days. Thus the modification of SST gradient over time can be relevant to this study. The modelled sea breeze depends on the land surface sensible heat flux, ambient geostrophic wind, atmospheric stability and moisture, water body dimensions, terrain height and slope, SST gradients, Coriolis parameter, surface roughness length, and shoreline curvature (Crosman and Horel, 2010). In order to capture these features in the model simulation, the spatial resolution is a key factor to determine the model performance on simulating different scales. Studies demonstrated that finer horizontal spatial resolution (0.5 km, Loughner et al., 2011; 1.33 km, He et al., 2014) model runs agreed better with the pollutant observation at the top of the boundary layer and resolved the structure of the bay breeze better, in contrast to the coarser model resolutions (13.5 km, Loughner et al., 2011; 12 km, He et al., 2014). Similar results were also reported by Jimenez et al. (2006) which concluded that O_3 simulation during sea breeze from the fine model resolution is better than the coarse resolution.

This study further investigates the influence of CB on the O_3 mixing ratio distribution by employing a mesoscale model, the Weather Research and Forecasting model coupled with Chemistry (WRF-Chem; Grell et al., 2005). It aims to quantify the relative influence of the bay-land dynamics on the O_3 concentration nearby bay areas. One baseline experiment ("water") and one sensitivity experiment ("nowater") were performed with the normal configuration and by altering the model configuration of the underlying water over CB to land (loam), respectively. First, the baseline model simulation performance was evaluated by the surface O_3 mixing ratio observations to make sure that model simulations were reliable. Then, both horizontal and vertical O_3 distribution differences between "water" and "nowater" over CB, were analyzed to

study the resulting dynamics and its influence on the temporal-spatial O_3 concentration distribution.

1.3 Transported O_3 and particle pollutions

Wildfires influence O_3 and PM, which play vital roles in air quality, climate change and human health (Intergovernmental Panel on Climate Change (IPCC), 2013). Wildfires burned from forest, savanna and grassland, caused by lightning and/or humans (prescribed burns or accidents), are sources of both primary and secondary pollutants (trace gases and aerosol particles), including CO, H_2, CH_4, N_2O, NOx, O_3, and fine particles ($PM_{2.5}$) (Crutzen et al., 1979; Crutzen and Andreae, 1990; Andreae and Merlet, 2001). Long-term exposure to high concentrations of O_3 leads to health issues, i.e., irritates lungs, aggravates bronchitis, emphysema, and asthma (Lippman, 1991; Gan et al., 2020). The subject of this study is becoming increasingly important for the reason that future trend of wildfire events, the frequency and averaged area burned each year is predicted to increase due to warmer, drier climate (Liu et al., 2010; Schoennagel et al., 2017). Climate change is expected to increase the wildfires occurrences over the regional and/or global scale. Thus, long-term smoke transport effects on human health increases are likely. Estimates are that global warming has already impacted the frequency and intensity of wildfires for Canadian and U.S. forests over the past century (Gillett et al., 2004; Westerling et al., 2006; Roberts et al., 2020).

Model simulations of O_3 and PM from across scales were performed in several previous studies. In the recent decade, the most common air quality models employed for air quality research are CMAQ (Community Multiscale Air Quality Modeling System, Loughner et al., 2011; Dreessen et al., 2016) and WRF-Chem (Weather Research and Forecast model coupled with Chemistry package, Hu et al., 2012, 2013; Yang et al., 2013; Su et al., 2017). In addition to air

quality models, atmospheric transport model, and back trajectories are often combined with WRF-Chem simulations and utilized to track the regional transport of O_3 (Su et al., 2017). Specifically, O_3 pollution near CB and Baltimore-Washington area was investigated through field campaigns and model simulation experiments (Loughner et al., 2011; Hu et al., 2012, 2013). While a general agreement is reported between observations and modeling, in general, there are a number of issues that are actively being studied and need further investigation. The issues and discrepancy that arise are partially attributed to the underestimation of the Planetary Boundary Layer Height (PBLH) and dry deposition (Zhang et al., 2009) as well as the emissions data used. An important problem of forecasting air quality is transport and mixing of external O_3 sources, as could occur because of fire smoke. Understanding how the smoke from fires transports, what is the chemical composition of the smoke plume, and how it mixes within the PBL is essential to improve air quality forecast. Not accounting for the smoke emission model simulation would result in an output that underestimates the O_3 concentration compared with observations (Dreessen et al., 2016). On the other hand, inclusion of the smoke emission may overestimate the O_3 concentration forecast. Understanding the physics and dynamics of meteorology as well as its associated phenomenon of long-range transport is an important scientific and operational forecasting problem. For the regions other than the U.S., most recently, Su et al. (2017) utilized both ground-based and airborne O_3 lidars to measure the O_3 vertical profiles in early September, Hangzhou, China, and found that the O_3 concentration reached a peak at the top of the boundary layer. Wang et al. (2013) and Yang et al. (2013) studied the wildfire smoke particle transport using the optical properties captured by Moderate Resolution Imaging Spectroradiometer (MODIS) and Cloud-Aerosol Lidar with Orthogonal Polarization (CALIOP).

The long-range transport of smoke and its contribution to local air pollution is difficult to quantify and thus forecast (Kunzli et al., 2006; Wu et al., 2018). The physics of how the long-range transported smoke mixes into the boundary layer from the upper atmosphere is not well understood. Satellite observations of such long-range transport smoke is readily available, which help the modeling of physical processes on how the long-range transported smoke mixes down to the surface (Campell et al., 2016). The synoptic steering flows, the physical development, and dynamics of wildfires from the local-to-regional scales govern how the smoke transport impacts downwind regions at the local pollution scale.

Several previous studies have investigated the influence of Canadian boreal forest wildfires on trace gases and particles (Wotawa and Trainer, 2000; McKeen et al., 2002; Colarco et al., 2004; DeBell et al., 2004; Morris et al., 2006). An extensive wildfire event, which occurred over northwestern Canada in June 1995, resulted in the increase of CO and O_3 concentrations over the midwestern and eastern U.S. (Wotawa and Trainer, 2000; McKeen et al., 2002). Both models and observations showed that O_3 concentration increased by 15-18% over the eastern U.S., due to both photochemistry and transport (Wotawa and Trainer, 2000). Since O_3 is sensitive to the NO_X/CO emission ratios as reported in Crutzen et al. (1979), the urban area which has high NOx concentrations, is more sensitive to the aged smoke compared to that in the rural area (McKeen et al., 2002). Another Canadian wildfire happened in Quebec, Canada early July 2002 (Colarco et al., 2004; DeBell et al., 2004; Morris et al., 2006). Smoke and other pollutants were transported to the U.S. at low altitudes behind advancing cold fronts (Colarco et al., 2004). The significant enhancements of CO, $PM_{2.5}$, organic and black carbon (OC and BC), and the soluble aerosol species NO_3^+, Ca^{2+}, and the biomass burning tracer K^+ marked this wildfire event. The study reported that the smoke plumes were transported to New England,

which depended on a combination of factors, among which are the altitude of transport, the degree of enhancements and chemical composition of aerosols varied with sampling station elevation and latitude (DeBell et al., 2004). Overall, these studies utilized a variety of observations and models to explore the origin of Canadian wildfires and their impacts on the U.S. air quality.

An example of the effect of long-range transport Canadian wildfire smoke in June 2015 and its effect on air quality was reported by Dreessen et al. (2016), which investigated its impact on BC, OC, O_3 and PM concentrations in Maryland. Following this report, Sullivan et al. (2017) reported a focused study on the lesser-characterized night-time transport and vertical mixing/entrainment of O_3 in the context of "next-day" O_3 exceedances. Although these two studies described the pollution episode caused by the Canadian wildfires at the local region in Maryland, a coordinated mesoscale model-assisted study of this event had not been performed to date. In this work, we examine this impactful Canadian wildfire event by combining the advanced ground-based in-situ and remote sensing observations, together with the WRF-Chem model to explore the smoke transport path and validate its impact on the local-to-regional air pollution. These include details of the arrival of the transported smoke, the satellite-model comparisons, the regional surface, and remote sensed measurements and in particular the evolution of measurements and model simulations within the PBL.

This chapter follows the structure below. First, we set up the study domain and model configuration, including the parameterization schemes and designed model experiments. Second, a description of the standard surface and upper-air O_3 data, ground-based remote sensing data, and satellite data employed in the analysis, followed by the results and discussion section. The

result analysis includes smoke large-scale transport and local O_3 and PM enhancement due to smoke. Finally, we complete this study with a conclusion.

1.4 Data assimilation

Data assimilation (DA) is the approximation of the true state of some physical system at a given time by combining time-distributed observations with a dynamic model in an optimal way (Asch et al., 2016). More specifically, it combines information from three different sources: the physical and chemical laws of evolution (encapsulated in the model), the reality (as captured by the observations), and the current best estimate of the distribution of pollutants in the atmosphere (all with associated errors) (Carmichael et al., 2008). The DA methods include variational methods, statistical methods, and hybrid methods which combine variational and statistical methods (Fig. 1.1). Both variational and statistical methods seek an optimal solution, while variational methods seek a solution that minimizes a suitable cost (or error) function, and statistical methods seek a solution with minimum variance. In fact, in most cases these two methods provide exactly the same solution.

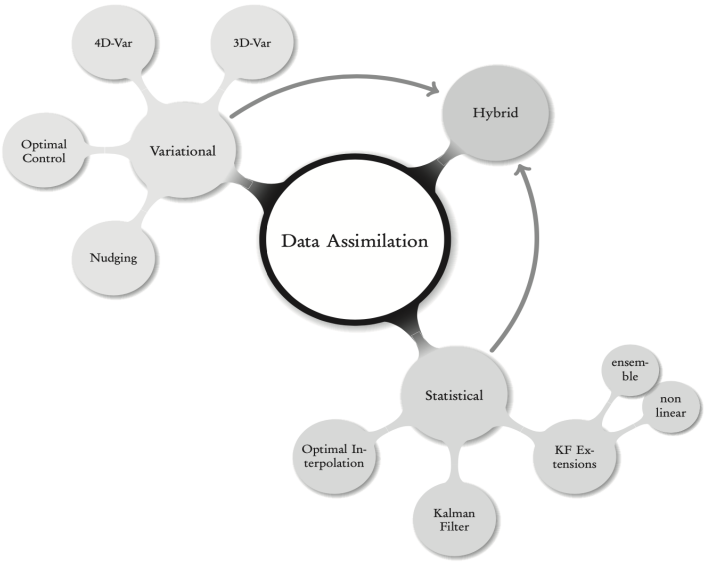

Fig. 1.1 The big picture for DA methods and algorithms (Asch et al., 2016)

DA integrates both model forecasting and observations to better estimate the state of a physical system (Daley 1991; Kalnay 2003). The DA techniques are broadly used in different fields under different names. The output of the updated analysis data after combining observations and model forecasts acts as the initial conditions for the time step model forecast. After observing the true state of the atmosphere, DA can produce reanalysis, the best available estimate of the atmospheric state, by repeating the numerical weather prediction process. DA can act as a simulator to estimate the value of existing or historical observations, i.e., satellite simulator. In addition, the applications of DA include evaluating forecast models, identifying quantities that are poorly predicted and comparing models to assess relative strengths and weaknesses (Anderson et al., 2009). Finally, DA constrains the emission input data by solving the inverse problem (Xu et al., 2013).

The DA method employed in this study is the Ensemble Adjustment Kalman Filter (EAKF), which computes a linear operator that is applied to the prior ensemble estimate of the state, resulting in an updated ensemble whose mean and covariance are consistent with the theory (Anderson, 2001; 2003). In this section, I will elaborate on its mathematical background and applications, with some general introduction to DA.

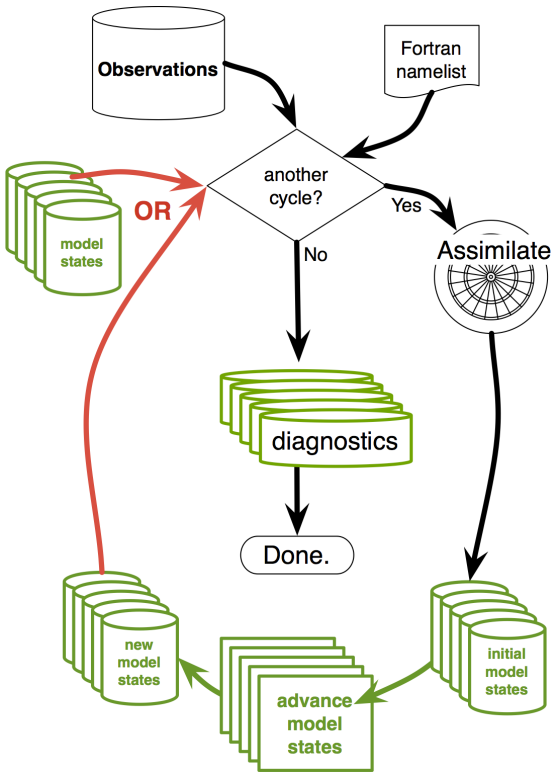

Fig. 1.2 Data assimilation flowchart

DA procedure includes two steps: forecast/prediction step, analysis step. In the forecast/prediction step, models are initiated by the initial condition/boundary condition (IC/BC). For the regional models, i.e., WRF-Chem, the IC/BC is from the global models. The output of the forecast/prediction step is called background or prior. Then the data assimilation system will determine whether to continue to the next cycle. If this is the first cycle, next will be the assimilation/analysis step. If this is not the first cycle and the data assimilation objective has not been achieved, then it will carry out the assimilation/analysis step. Otherwise, it will stop assimilation.

The assimilation/analysis step combines the observations and models. The DA methods are employed in this step to assimilate observations into models. The output of the analysis step is named analysis or posterior. After the assimilation/analysis step, the model will advance to the next step or assimilation window.

1.4.1 Sequential data assimilation methods

1.4.1.1 Kalman Filter

Kalman filter, also known as linear quadratic estimation, is a recursive approach to estimate the unknown variables, by estimating a joint probability distribution over the variables for each timeframe (Kalman, 1960; Kalman and Bucy,1961). It is a probabilistic-based method. Initially, it was developed to solve theoretical and practical problems in communication and control by using statistical methods. Such problems include (i) Prediction of random signals; (ii) Separations of random signals from random noise; (iii) Detection of signals of known form in the presence of random noise (Kalman, 1960).

1.4.1.1.1 Kalman filter in scalar form

(1) Calculation of Kalman gain

Let K be the Kalman gain, ε_e be error in estimate, ε_m be error in measurement, E_t be the current estimate, E_{t-1} be the previous estimate, and M be the measurement. The Kalman gain, K can be obtained from equation (1.1) (van Biezen, 2015).

$$K = \frac{\varepsilon_e}{\varepsilon_m + \varepsilon_e} \tag{1.1}$$

The Kalman gain provides the weight between estimate and measurement for updating the new estimate. Its value is between 0 and 1. When the Kalman gain approaches 1, the measurement becomes more accurate and the estimate is unstable (with high uncertainty). Otherwise, when the Kalman gain is closer to 0, the measurement gets inaccurate and the estimate is stable.

(2) Update the new estimate error

First, we need to update the new estimate using eq (1.2).

$$E_t = E_{t-1} + K(M - E_{t-1}) \tag{1.2}$$

Then use eq (1.3) to update the new estimate error based on the measurement error and the previous estimate error.

$$\varepsilon_{est_t} = \frac{\varepsilon_m \varepsilon_{est_{t-1}}}{\varepsilon_m + \varepsilon_{est_{t-1}}} = (1 - K)\varepsilon_{est_{t-1}} \tag{1.3}$$

Then output the new estimated value. if the variation becomes small, then terminate the iteration. Otherwise, continue to the next iteration if the variation is still very large (Fig. 1.1).

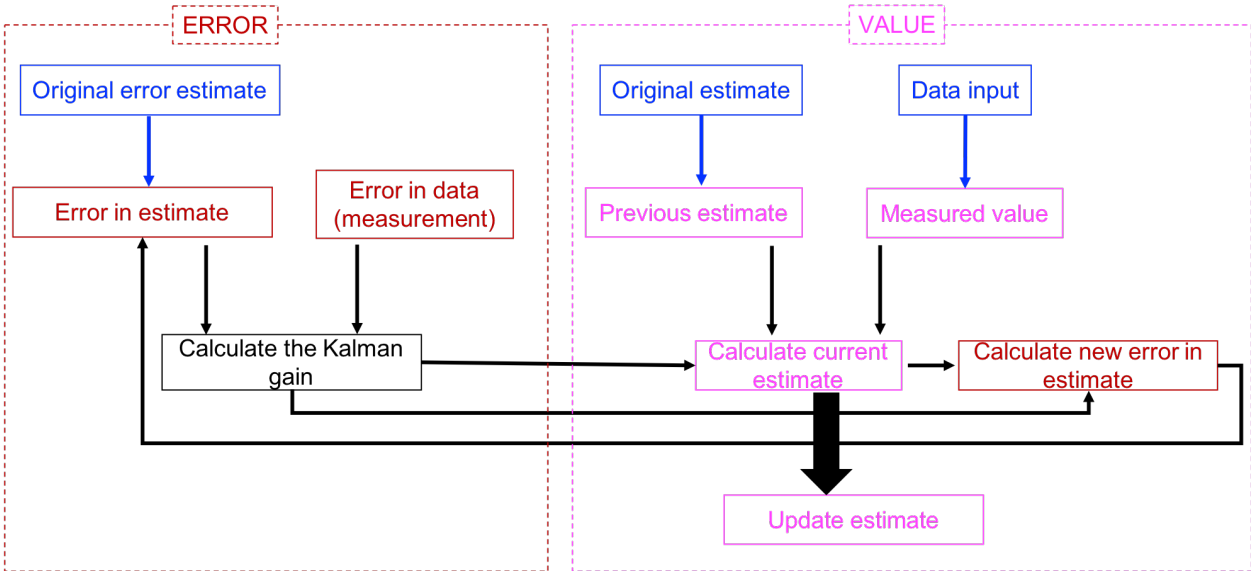

Fig. 1.1 General conceptual Kalman Filter flow chart. Blue ones are initial values; Red ones are errors; Pink ones are values.

1.4.1.1.2 Mathematical form of Kalman Filter

Let X_0 be the initial state matrix and P_0 be the initial process covariance matrix. For the first cycle, the initial state is treated as the previous state. Let U_k be the control variable matrix and W_k be the predicted state noise matrix, where k is the cycle number. A and B are transition matrices which are used to transform X_{k-1} and U_k to be the same size of the predicted state matrix X_{k_p}. As a matter of fact, A is a unit upper tridiagonal matrix. Then, we can calculate the predicted state

matrix, X_{k_p} based on the physical model and previous state from eq (1.4), and the predicted process covariance matrix, P_{k_p} from eq (1.5), where Q_k is the process noise covariance matrix.

$$X_{k_p} = AX_{k-1} + BU_k + W_k \tag{1.4}$$

$$P_{k_p} = AP_{k-1}A^T + Q_k \tag{1.5}$$

Now calculate the Kalman gain K using eq (1.6), where H is the transition matrix and R is the measurement error matrix (or sensor noise covariance matrix).

$$K = \frac{P_{k_p}H}{HP_{k_p}H^T+R} \tag{1.6}$$

Now update the new measurement, and combine with predicted state matrix X_{k_p} and the Kalman gain K. Then use eq (1.7) to calculate new state matrix X_k

$$X_k = X_{k_p} + K[Y_k - HX_{k_p}] \tag{1.7}$$

Here Y_k the measurement of the state, which is computed using eq (1.8)

$$Y_k = CH_{k_m} + Z_k \tag{1.8}$$

Where, H_{k_m} is the transformation matrix that maps the state vector parameters into the measurement domain. And Z_k is the measurement noise (or uncertainty).

After getting X_k, use eq (1.9) to compute the process covariance matrix P_k.

$$P_k = (I - KH)P_{k_p} \tag{1.9}$$

The last step for every cycle is to check the values of the state matrix and process covariance matrix. If they satisfy the stopping criterion, then cycle and output them. Otherwise continue to the next cycle.

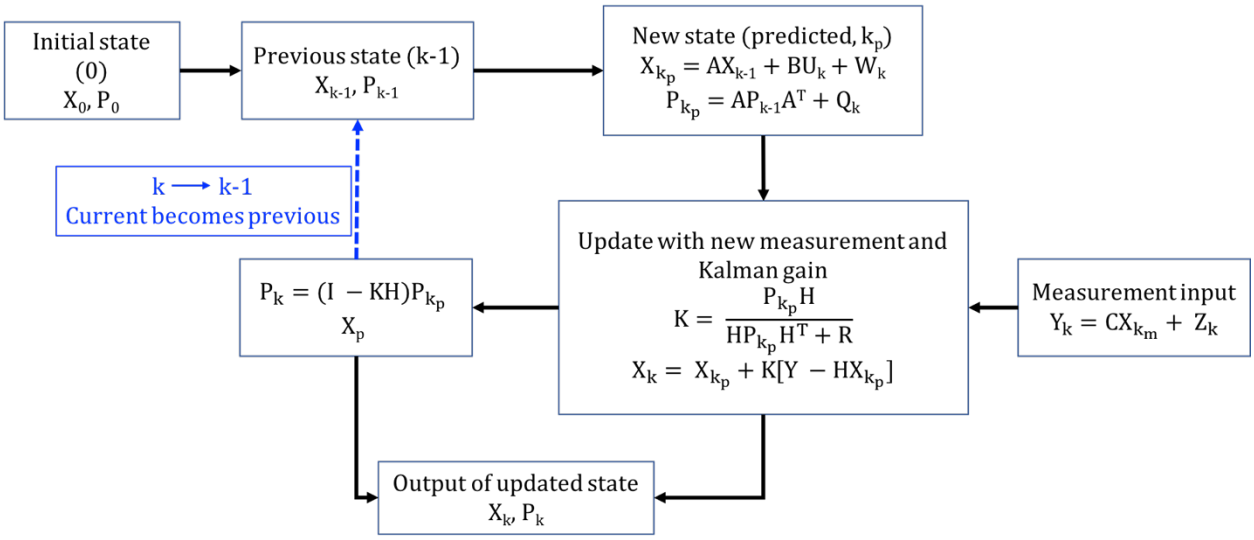

Fig. 1.2 Mathematical Kalman Filter (in matrix form) flow chart

1.4.1.2 Ensemble Kalman Filter

Based on the Kalman filter (KF) and extended Kalman filter (EKF), which is used to solve linear and nonlinear systems, respectively, Evensen further developed the capability of Kalman filter for processing the nonlinear systems by unifying the data assimilation and ensemble generation problem (Evensen, 1992; 1994; 2003), which leads to the ensemble Kalman filter (EnKF). The EnKF is based on a statistical linearization or closure approximation that is too severe to be useful for some cases with strongly nonlinear dynamics (Evensen, 1992). The EnKF is a sequential data assimilation method using Monte Carlo or ensemble integrations (Burgers et al., 1998). It uses the traditional update equation of the KF, except that the gain is calculated from the error covariances provided by the ensemble model states. There are several benefits of EnKF. For example, it is relatively computationally efficient, since the ensemble size does not require too big, which will be sufficient for reasonable statistical convergence. However, the observations must be treated as random variables. The EnKF generates a random sample of the observational distribution, called “perturbed observations” (Houtekamer and Mitchell, 1998).

1.4.1.3 Ensemble Adjustment Kalman Filter (EAKF)

The ensemble adjustment Kalman filter (EAKF) is derived as Monte Carlo approximations to the nonlinear filter without perturbing observations, developed by Anderson (2001). It is a deterministic scheme of the EnKF and performs better than the classical (stochastic) EnKF in a general framework. It is assumed that the prior ensemble forecast distribution follows the Gaussian distribution.

1.4.2 Inflation and variance divergence

1.4.2.1 Errors

1.4.2.1.1 Observational Error

Observational error includes measurement error and representative error. The representative error is normally larger than the measurement error (Daley, 1991; Chai et al., 2007).

1.4.2.1.1.1 Measurement error

Measurement error is the difference between a measured value of a quantity and its true value. It can be divided into two components: random error and systematic error.

1.4.2.1.1.2 Representative Error

Representative error comes from the difference in resolutions between individual measurements and the model, which could degrade the data assimilation performance. The representative error includes deficiencies in the equations representing the processes of the system as well as the error introduced by representing a continuous system using a series of discrete points. In the same model grid, there are several measurements with different observation values. During the data assimilation, observations are trusted as ground-truth. If representative errors are random

and large numbers of observations are assimilated, their impact could be negligible (Koshin et al., 2020).

1.4.2.1.2 Random error

Random error (or random variation, or stochastic error) is a measurement of inconsistent data (a constant attribute or quality) when repeatedly measured or taken. It is always present in a measurement and may vary from observation to observation. Random error can be caused by unpredictable fluctuations in the readings of a measurement apparatus, or in the experimenter's interpretation of the instrumental reading; these fluctuations may be in part due to interference of the environment with the measurement process. The concept of random error is closely related to the concept of precision. The higher the precision of a measurement instrument, the smaller the variability (standard deviation) of the fluctuations in its readings.

1.4.2.1.3 systematic error (or statistical bias)

For instrument observations, the systematic error is from the measuring instruments, due to the instrument or its data handling system or wrong operation. The systematic error is the error that is not determined by chance but is introduced by an inaccuracy inherent to the system. Systematic errors are caused by imperfect calibration of measurement instruments or imperfect methods of observation, or interference of the environment with the measurement process, and always affect the results of an experiment in a predictable direction. Systematic error refers to an error with a nonzero mean, the effect of which is not reduced when observations are averaged. It always occurs, with the same value, when we use the instrument in the same way and in the same case. The sources of systematic error are imperfect calibration of measurement instruments (zero error), quantity, and measurement drift.

1.4.2.1.4 Sampling Error:

Sampling error is introduced by observing a sample instead of the entire population. It is the difference between a sample statistic used to estimate a population parameter and the actual but unknown value of the parameter, since the ensemble size is small. The limitation of sampling error is the supposedly representative sample population in reflecting the total population.

Sampling bias is a possible source of sampling errors, wherein the sample is chosen in a way that makes some individuals less likely to be included in the sample than others. It leads to sampling errors which either have a prevalence to be positive or negative. Such errors can be considered to be systematic errors. It can also be quantified by the margin of error. The larger the margin of error, the larger the sampling error, which means that the less confidence one should have that a sample result would reflect the result of the whole population.

1.4.2.1.5 Correlated observational error

The uncorrelated observational error can be achieved when the observations are taken with separate immovable instruments such as those from the surface stations (Daley, 1991). The radiosonde usually has the vertical correlated observational errors, while satellite observations have both horizontal and vertical correlated observational errors.

1.4.2.2 Inflation

The above-mentioned errors influence the quality of data assimilation. In order to compensate for these errors (i.e., sampling errors), an inflation factor is often used to multiply to the background covariances and enlarge the background error. The inflation concept was first introduced by Anderson and Anderson (1999). Usually the inflation factor can be tuned for different models and observations. When properly tuned, the inflation factor can improve the convergence of the analysis during data assimilation.

1.4.3 localization

Due to the computational cost, the ensemble size is set much smaller than the dimension of the model state. It leads to the correlations among spatially remote variables in the prior ensemble being regarded as spurious correlations in the ensemble methods. The limited ensemble size causes the sample estimated prior error covariance to be rank deficient, and results in the covariance between observation and model state to be contaminated with sampling noises when they are at a larger distance. To compensate for this under-sampling issue, localization is introduced to reduce the prior correlations based on the distance between the observed and modeled state variables (cutoff distance or radius of influence (ROI)) by localizing the impact from distant observations and rectifying the negative impact from sampling noises (Houtekamer and Mitchell, 2001). We apply a typical choice of localization function, Gaspari and Cohn (1991) fifth-order polynomial, to reduce the spurious impact of observations on spatially remote state variables.

1.4.4 Observation forward operator

The observation forward operator is a bridge linking the model state variable and observations in a data assimilation system. It interpolates the model state variables to the location of observation. Since the model data are gridded and the observations are data points, an interpolation of the model fields from the grid to the locations of the observations needs to be performed. If the observed variable is not the model state variable, the observation forward operator will perform transformations and convert the model state variable to the observed variable, which may be nonlinear. In this case, the observation forward operator allows the comparison between observations and model state variables (both background/prior and

analysis/posterior). For instance, satellites measure radiances/brightness temperatures/reflectivities, etc., not directly temperature, humidity, and ozone.

1.1.3.7 Advantages and challenges of application of EnKF

The advanced features of EnKF include that (1) it can propagate the probability density functions (PDFs) through highly nonlinear systems; (2) it does not require additional modeling efforts such as the construction of tangent linear model and its adjoint; and (3) the method is highly parallelizable (Carmichael et al., 2008). The challenges also exist while applied to solve the data assimilation problems. First, the rank of the estimated covariance matrix is smaller than its dimension. Second, the random errors in the statistically estimated covariance decrease only by the square-root of the ensemble size. Third, the subspace spanned by random vectors for explaining forecast error is not optimal. Fourth, the estimation and correct treatment of model errors is possible but difficult. Fifth, a careful implementation is required for efficiency (Carmichael et al., 2008).

1.5 Motivation and Objectives

The motivations of this study are the air quality sources tracking. The Maryland Department of Environment puts effort on understanding the O_3 pollution contribution from CB. The O_3 concentration in Maryland during Summer often exceeds the NAAQS. However, the sources of the pollutants are unknown. Two possibilities on tracking the sources. One is the local sources; the other is transported from outside of Maryland. In order to guide the local factories and manufacturers, it is very important to identify the pollutant sources.

Chapter 2

The influence of the Chesapeake Bay on the ozone pollution

This Chapter is organized as follows: a description of the model configuration and study domain is given in section 1, followed by a discussion of the background, case study, and data sets in section 2. Results and analysis are given in section 3 and concluding remarks are presented in section 4.

2.1 Model Configuration and Study Domain

WRF-Chem (version 3.7) integrates the air quality component consistent with the meteorological components (Grell et al., 2005). The gas-phase chemistry and aerosol module were based on the Carbon-Bond Mechanism Version Z (CBM-Z, Zaveri and Peters 1999) and the Model for Simulating Aerosol Interactions and Chemistry (MOSAIC, Zaveri et al., 2008), respectively. The Yonsei University (YSU) planetary boundary layer scheme (Hong et al., 1996; 2006) was used here based on the model performance evaluation and recommendation for such an area (Hu et al., 2010). Radiation treatment utilized the Rapid Radiative Transfer Model for General Circulation Model (RRTMG) short-wave and long-wave radiation schemes (Iacono et al., 2008). The radiation scheme was in line with what was recommended for the model simulations over the continental U.S. by the WRF developer team (Peckham et al., 2015).

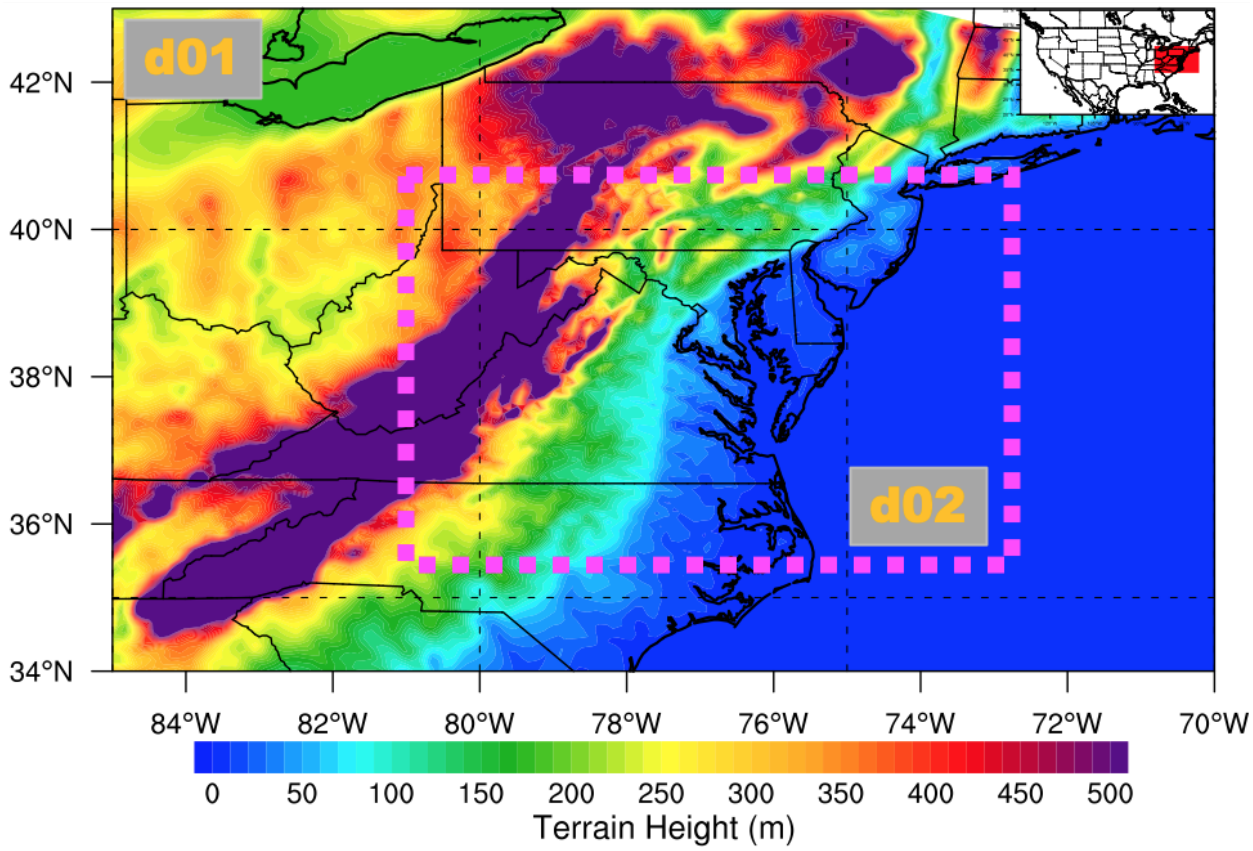

Fig. 2.1 Terrain height of the area surrounding CB over the eastern U.S. The outer domain is denoted as d01 and the nest domain is encoded with the pink dashed rectangle (d02). The insert map on the top-right shows the location of the study region (red shade) over the Continental U.S. (NCAR Command Language)

Figure 2.1 shows the model domain, with the outer study area set to include the eastern U.S. The outer domain was further resolved by one two-way nested grid region that progressively focuses and centers on the study region, CB. The outer domain (d01) was set at 9 km × 9 km horizontal spatial resolution, while the nested inner domain (d02) had a higher horizontal spatial resolution (3 km × 3 km) because it exclusively focused on the detailed investigation of O_3 concentration and its evolution. 35 vertical levels were used with about 15 levels set below 800 hPa to resolve the PBL and the model top was at 100 hPa.

2.2 Background, Case Study, and Data Sets

2.2.1 Topography of the CB Surrounding Region

CB is located at the western coast of the Atlantic Ocean and surrounded by the states of Maryland, Virginia, and Delaware. It is approximately 320 km long from north to south, 4.5 km wide at its narrowest from west to east, and 48 km at its widest point. The average depth is 6.4 m with a maximum of 53 m (National Centers for Environmental Information, 2017). The terrain towards the east of CB is flat, and its terrain height is less than 50 m. Mountains are located 100 km away west of CB, with the terrain height more than 1000 m (Fig. 2.1). CB alters moisture, wind speed and direction, and atmospheric stability. Due to the evaporation of the water body over CB, the air moisture level near it is higher than the surrounding area. It has relatively high temperature at night and makes the atmosphere unstable, while in the day, it has relatively low temperature and stabilizes the atmosphere.

2.2.2 Case Study

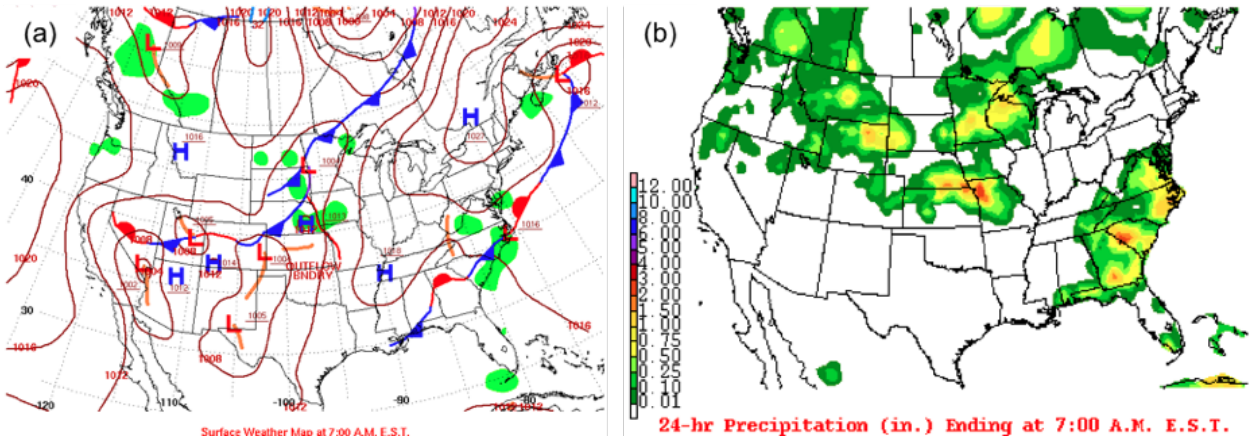

Fig. 2.2 (a) Surface weather map at 7:00 AM EST (11:00 UTC) on 3 June 2015, with low-pressure systems and high-pressure systems indicated by L (red) and H (blue), respectively; (b)

24-hour precipitation at 7:00 AM EST on 4 June 2015

(http://www.wpc.ncep.noaa.gov/dailywxmap/)

This study focuses on the case of 3 June 2015, which was picked for the following reasons. First, since O_3 is mostly a summertime problem, and early June is the beginning of summer. Second, a cold front from the northwest encountered a warm front from the southeast in the Mid-Atlantic region (Fig. 2.2a). There was a low-pressure system near North Carolina, which formed clouds and precipitation over the study region (Fig. 2.2b & 2.3). The cloud fraction was 100 % from the MODIS cloud product (Fig. 2.3c, d). The 24-hour precipitation map shows that the rainfall was around 0.1 - 0.5 in (or 0.25 - 1.25 cm, Fig. 2.2b). This means that less solar radiation was expected over CB which would reduce the photochemical reactions of O_3 and its precursors. So the chemistry influence on O_3 generated was limited due to the absence of sunlight. Third, the prevailing winds on this day were northeast, rather than the typical northwest. This would avoid the influence of pollutants transported from the Ohio River Valley.

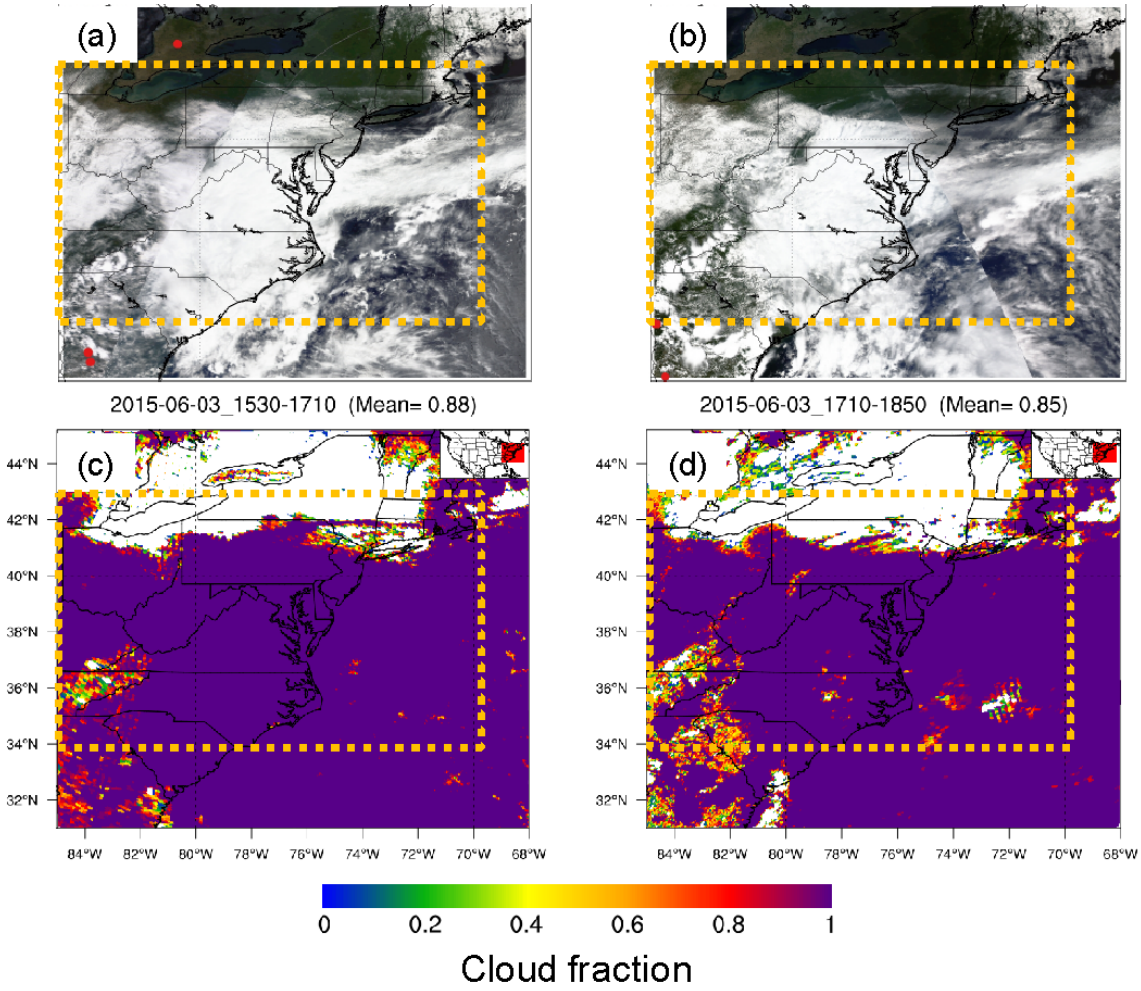

Fig. 2.3 MODIS three-band color overlay images (band 1—red, band 4—green, and band 3—blue) from Terra (a) and Aqua (b) satellites on 3 June 2015. Red dots indicate the locations of daytime fires detected by MODIS. Note that the fire dot scale has been enlarged in order to portray the fires more clearly in the figure. Bottom images are MODIS cloud fraction from Terra (c) and Aqua (d). The orange dashed rectangle is the outer domain (d01)

2.2.3 Data Sets

Relevant information on data used in the simulation and sensitivity studies as well as model evaluation is presented in Table 2.1.

Table 2.1 Data used as inputs to WRF-Chem simulations and evaluations

Data type	Description
Meteorology	Northern American Regional Reanalysis (NARR) dataset, which is a high-resolution model-assimilated observation dataset from National Centers for Environmental Prediction (NCEP). The NARR covers the time period from 1979 to near present and provides 3-hourly and monthly data at a resolution of approximately 32 km with 29 pressure levels, from 1000 to 100 hPa.
Anthropogenic emission	National Emissions Inventory 2011 (NEI2011) from the U.S. EPA. The NEI2011 is a comprehensive and detailed estimate of the air emissions for criteria pollutants, precursors, and hazardous air pollutants. It includes point sources and area sources with resolution of 4 km by 4 km, covering all the 48 contiguous states as well as selected regions of Canada and Mexico
AirNow	The EPA AirNow program provides forecasts and near real-time observed air quality information across the U. S., Canada, and Mexico (http://www.epa.gov/AirNow). It receives air quality observations from over 1000 monitoring stations and collects forecasts for more than 300 cities. For this study, the O_3 mixing ratio measured near the surface is used as evaluation data sets to estimate the model simulation performance.
Soil type	United States Geological Survey (USGS) soil types with 16 categories are used in the model. Further, in the model sensitivity analysis CB is replaced by the nearest and lowest altitude soil type (see detailed discussion below)

Both land use and water land mask data sets are used in this study. The land use (soil type) dataset from the United States Geological Survey (USGS) has 16 soil categories (Fig. 2.4). Since the spatial resolution of the land mask dataset is 30 arcsec, it can't resolve the fine streams and branches feeding into CB. As a result, the shape of the water mask doesn't exactly follow the CB outline which may lead to uncertainties to the size of CB. In the sensitivity experiment, the land mask was altered from water to land over CB (Fig. 2.4a, b). The land use index was modified to loam, since the land over the eastern shore of CB is loam (Fig. 2.4c, d). The CB surface temperature was from NARR reanalysis data. In the following comparison, we only considered the O_3 mixing ratio difference between baseline and sensitivity experiments, except for the model performance evaluation where the O_3 mixing ratio was used.

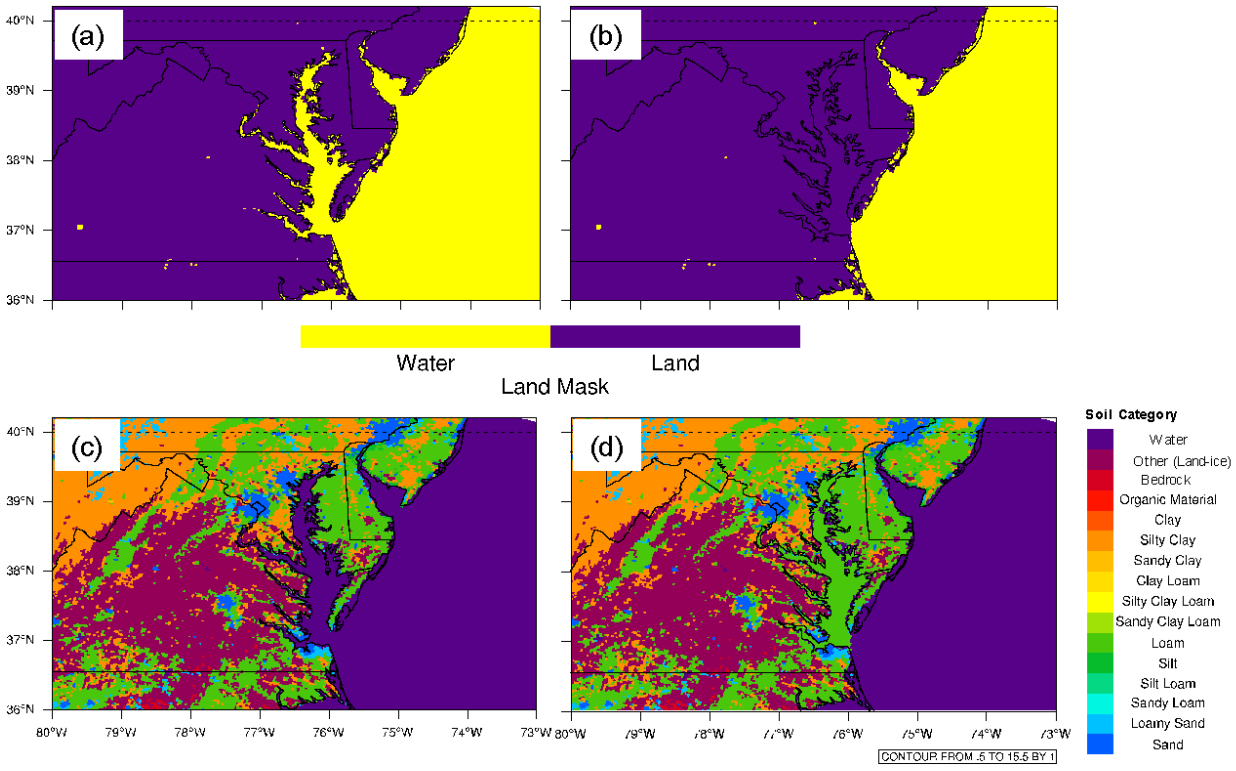

Fig. 2.4 (a) WRF USGS land mask; (b) Same as (a), but modified water to land over CB; (c) WRF USGS 16 soil categories; (d) Same as (c), but modified water to loam over CB

2.3 Evaluation and Results of Model Simulations

2.3.1 Evaluation of Model Performance

In order to stabilize the meteorological and chemical fields, the baseline experiment was conducted from 1200 UTC, 1 June to 0000 UTC, 4 June 2015. The first 36 h simulations were treated as spin-up, and the remaining 24 h simulations (from 0000 UTC, 3 June to 0000 UTC, 4 June) were selected for analysis. The sensitivity experiment was the same as the baseline experiment, except the surface land type over CB. The surface land type was changed from water to land (loam) on 0000 UTC, 2 June 2015. After the alternation, the sensitivity experiment continued to run until 0000 UTC, 4 June 2015. In the following comparison between the baseline and sensitivity experiments, we selected the simulations from 0000 UTC, 3 June to 0000 UTC, 4 June 2015.

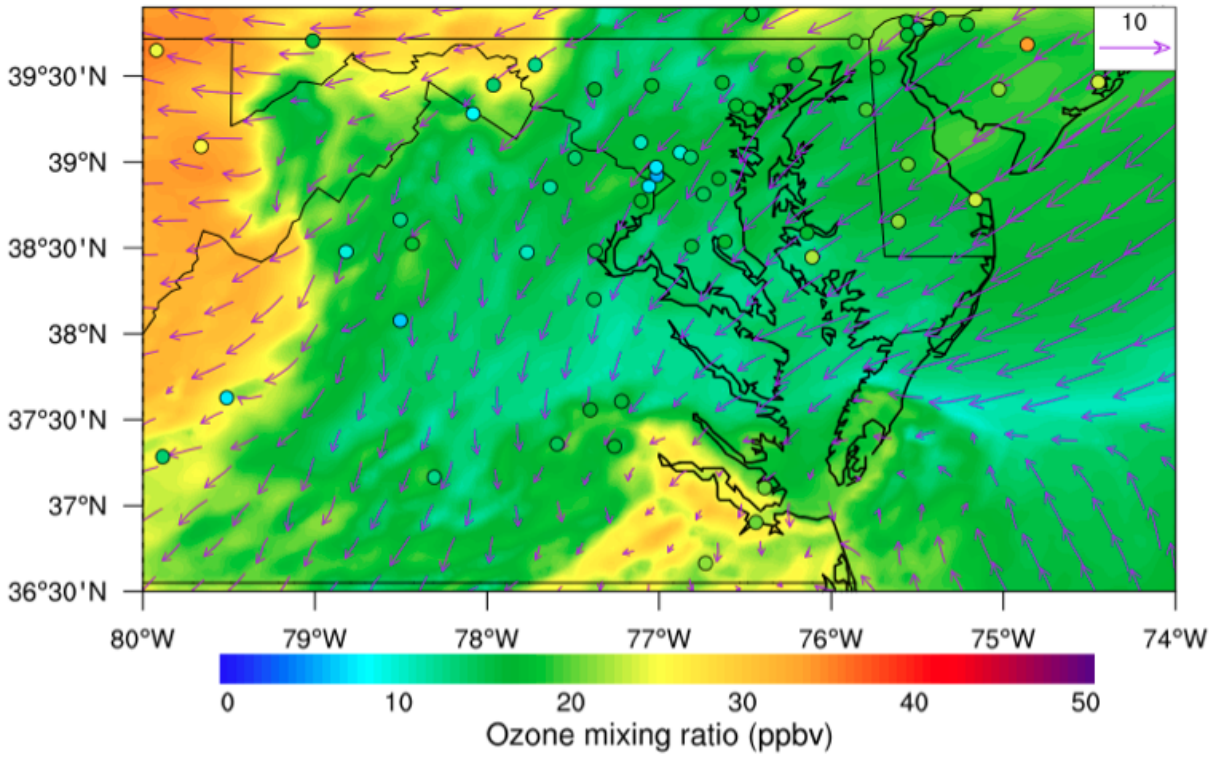

Fig. 2.5 WRF-Chem simulated surface O_3 mixing ratio and EPA AirNow observed surface O_3 mixing ratio (color filled circle) at 1500 UTC on 3 June 2015. The streamline is the surface wind. The wind magnitude is indicated by the length of streamline shown in the top-right insert, with unit of m s^{-1}

The wind patterns influenced the instantaneous surface O_3 mixing ratio horizontal spatial distribution. The prevailing winds were northeast in the northeastern domain, east over mountains, and north over Virginia state and south over the Atlantic Ocean in the southeastern domain. For example, the high O_3 mixing ratio (around 35 ppbv) over east of Appalachian Mountains was primarily due to the accumulated O_3 transported by the northeast winds from the polluted region nearby. When O_3 reached the eastern side of the mountains, it was blocked, accumulated, and lofted, leading to the apparent increase of the O_3 concentration (Fig. 2.5). On the other hand, the uniform northeast wind (5-15 m s^{-1}) over the relatively flat coastal terrain of Delaware-Maryland-Virginia favored a uniform surface O_3 mixing ratio spatial distribution. At the northern CB, the model simulated O_3 mixing ratio agreed with the AirNow O_3 observation well. The relatively high O_3 concentration (> 25 ppbv) existed over the south of CB. The high wind speed transported O_3 from CB, and local stagnant wind and weak convergence also contributed to the high O_3 concentration. Even though the influence of prevailing winds on the O_3 concentration distribution was important, the sensitivity experiment was able to capture the O_3 concentration differences due to the dynamics of CB. This is different from the study conducted by Stauffer et al. (2015), in which conclusions are based on the condition that the mesoscale or synoptic-scale wind must be absent. In comparison to the AirNow surface O_3 concentration, model results overestimated the surface O_3 mixing ratio over the middle and west of the study region, while underestimated O_3 in Delaware and New Jersey regions, due to the

clean air from the Atlantic Ocean. Overall, the model simulation showed O_3 mixing ratio surface spatial distribution patterns agree with observations (Fig. 2.5).

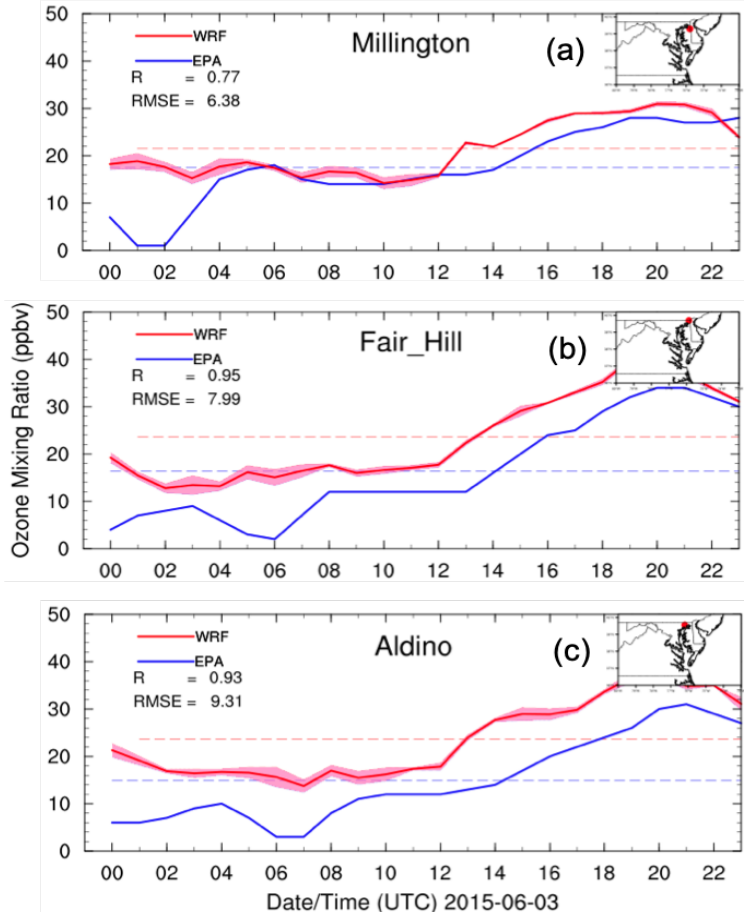

Fig. 2.6 Hourly surface O_3 mixing ratio diurnal variations from EPA AirNow observations (blue curves) and WRF-Chem simulations (red curves) at three AirNow sites. The light red shaded areas are standard deviations. Surface O_3 mixing ratio daily averages are denoted as dashed lines for AirNow (blue) and WRF-Chem (red). R is the Pearson correlation coefficient and RMSE is the root mean square error.

We investigated the hourly surface O_3 mixing ratio diurnal evolution of model-observation. In order to compare the model simulation with the observation, the simulated O_3 mixing ratio in nine 3 km × 3 km grids surrounding the AirNow station were aggregated to one 9 km × 9 km grid region and their mean and standard deviation were calculated. Figure 2.6 shows

hourly surface O_3 mixing ratio diurnal variations from three AirNow stations (Millington, Fair Hill, and Aldino) close to CB. As expected, the hourly surface O_3 mixing ratio diurnal variation had the lower O_3 mixing ratio at night (around 10 ppbv at 0600 UTC, sunrise was at 1030 UTC), and the higher O_3 mixing ratio at daytime (around 30 ppbv at 2000 UTC, sunset was at 0000 UTC). During the night, the absence of sunlight and less O_3 precursors (NO_X, etc) emissions prevented the required O_3 forming chemical reactions from being initiated. The correlation coefficients (R) and root mean square errors (RMSE) are 0.77, 0.95, 0.93 and 6.38, 7.99, 9.31 for Milington, Fair Hill, and Aldino, respectively. In general, the WRF-Chem model captured the AirNow measured O_3 mixing ratio diurnal variation trend pattern, but overestimated the O_3 concentration by 5-10 ppbv, or 20-30 %.

2.3.2 Overview of the O_3 Mixing Ratio Difference

The observational and modeled O_3 mixing ratio diurnal variation revealed the transition between the minimum and maximum of O_3 mixing ratio (Fig. 2.6). By separating the night-time modeled O_3 mixing ratio difference from daytime, the absolute and relative influences of CB can be analyzed explicitly. The relative difference is calculated using the equation

$$Diff_{rel} = \frac{W_{water} - W_{nowater}}{W_{nowater}} \times 100\ \%. \quad (2.1)$$

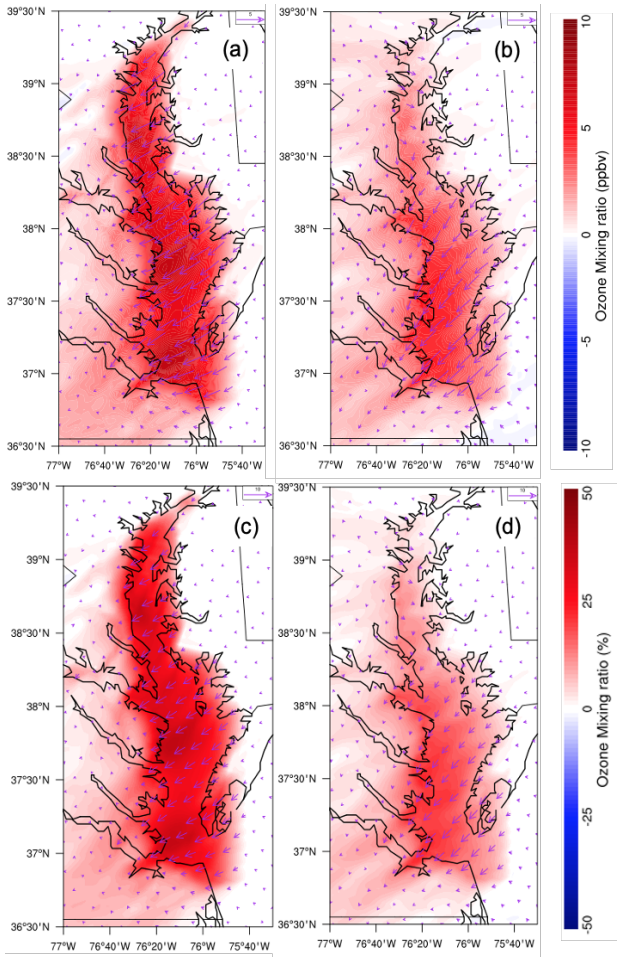

Fig. 2.7 WRF-Chem modeled absolute and relative O_3 mixing ratio difference between water and nowater for both night-time (a and c) and daytime (b and d). (a) absolute O_3 mixing ratio difference at night; (b) same as (a) but at daytime; (c) relative O_3 mixing ratio difference at night; (d) same as (c) but at daytime

On 3 June, the averaged surface O_3 mixing ratio over CB increased by 10 ppbv (30 %) at night and 5 ppbv (20 %) during the day (Fig. 2.7). The shallow stable nocturnal boundary layer "trapped" O_3 from venting to higher altitudes at night, while the deep mixed layer lofted O_3 to the free troposphere during daytime. At daytime, the O_3 mixing ratio difference was distributed semi-homogeneously over CB with more O_3 over the southern CB than the northern CB (Fig. 2.7b, d). The higher O_3 increase over the southern CB was due to the larger area of the water

body in the southern CB, which led to stronger bay breeze and photochemical reactions during the day. The O_3 mixing ratio difference increased slightly from east to west across CB consistent with the direction of the prevailing winds. The wind difference over CB indicated the wind increase due to the less surface friction over the water surface than land and contribution from bay breeze. In addition, the westward pooling of pollution created an elevated O_3 that extended into the Baltimore-Washington D.C. urban corridor (Loughner, et al., 2014). Figure 2.8 shows the O_3 mixing ratio difference gradient whose direction is from west to east (Fig. 2.8). At night, the O_3 mixing ratio difference gradient gradually decreased and approached the minimum at -1×10^{-5} ppbv m^{-1} close to the eastern shore (Fig. 2.8a). At daytime, the O_3 mixing ratio difference gradient had a pattern analogous to night-time, but had smaller magnitude (Fig. 2.8b).

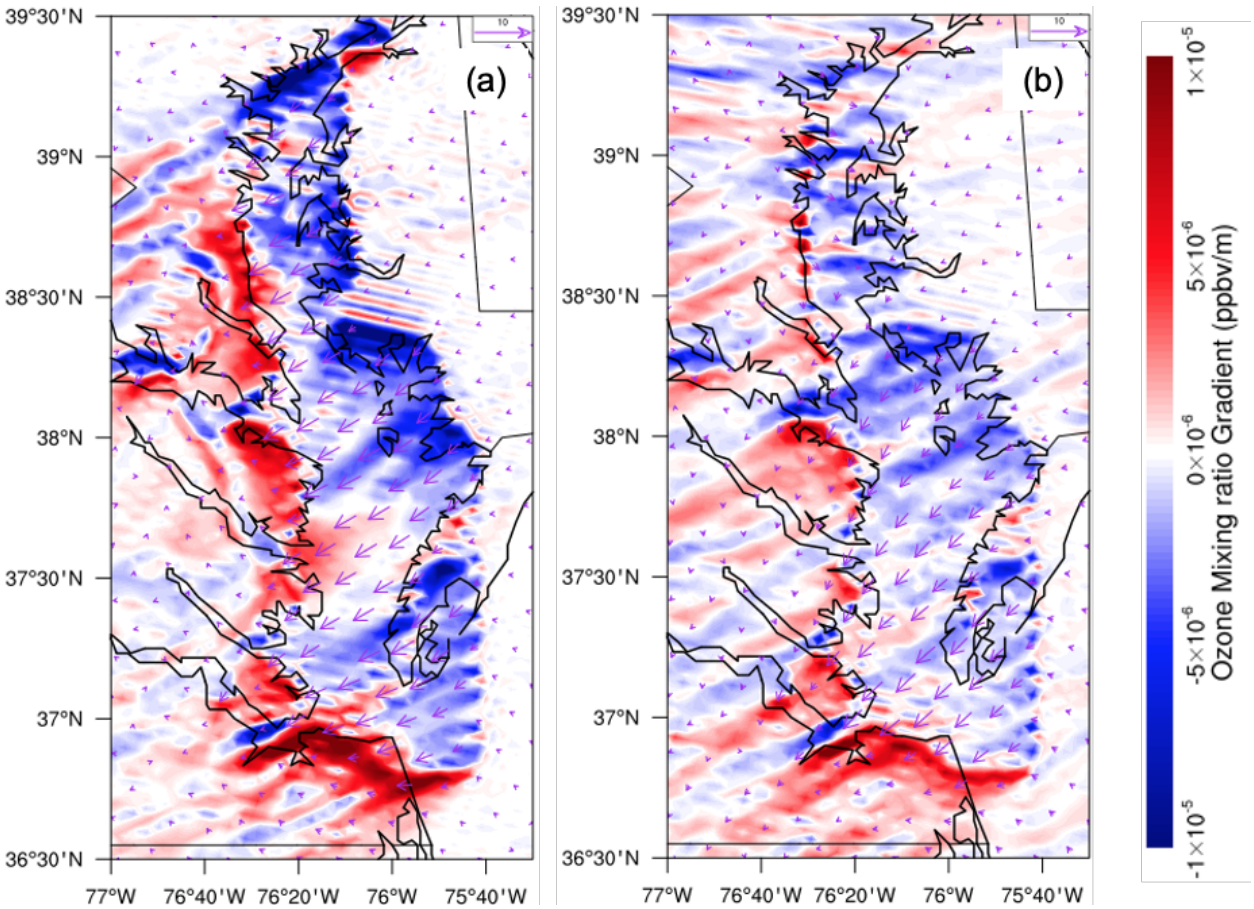

Fig. 2.8 WRF-Chem simulated surface O_3 mixing ratio difference gradient at both night-time (a) and daytime (b). The gradient direction is from west to east. The unit of O_3 mixing ratio difference gradient is ppbv per meter (ppbv m^{-1})

The surface O_3 mixing ratio diurnal variations of both the baseline and sensitivity experiments and their differences above CB are shown in Fig. 2.9. It shows that the surface O_3 mixing ratio above CB from the baseline and sensitivity experiments had a similar diurnal variation trend. The surface O_3 mixing ratio at night (about 20 ~ 25 ppbv) was lower than daytime (about 25 ~ 30 ppbv). The larger surface O_3 mixing ratio difference occurred at night (about 5 ppbv or 25 %), rather than daytime (about 2 ppbv or 15 %), due to the longer residence time of O_3 over CB at night. The wind speed over CB at night is lower than daytime, recorded 8 m s^{-1} and 12 m s^{-1}, respectively. At night, the residence of this higher O_3 air over CB tended to be longer. In addition, O_3 accumulated at the southern CB (and western shore of CB) where it was more impacted, and differences would add to the chance of exceeding O_3 mixing ratio limits. In fact, Goldberg et al. (2014) indicated that the 8-hour O_3 mixing ratio over CB exceeded the NAAQS at most twice during the DISCOVER-AQ-2011 project (27 June – 31 July 2011), while the surrounding land exceeded the NAAQS four (4) times, reinforcing the O_3 increase effect due to CB, especially over the downwind region.

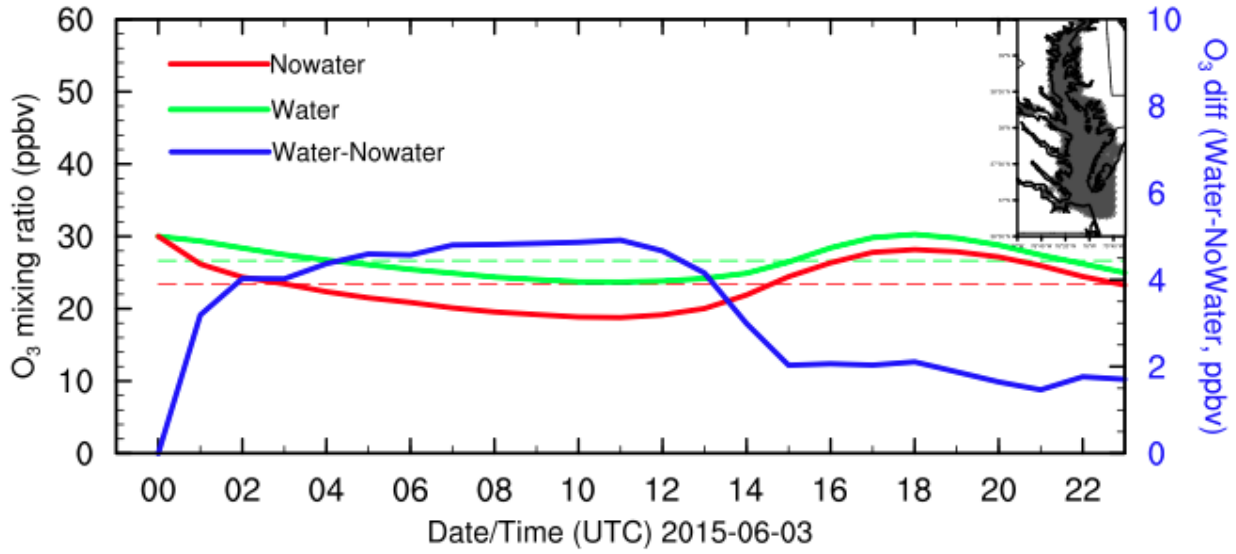

Fig. 2.9 WRF-Chem simulated surface O_3 mixing ratio for water (green) and nowater (red), and surface O_3 mixing ratio difference (water-nowater, blue) diurnal variation above CB on 3 June 2015. The dashed lines are surface O_3 mixing ratio means for water (green) and nowater (red). The grey shade in the top-right map indicates the location of CB

2.3.3 Dynamical Influence on O_3 Mixing Ratio

2.3.3.1 Horizontal Dynamical Influence

We analyzed the dynamic mechanism that increased the simulated O_3 mixing ratio solely due to the change of the land surface type. First, the thermal properties of water and land (loam) are different. The volumetric heat capacity of land (loam) is around 2.0×10^6 J m^{-3} K^{-1}, much smaller than water, 4.18×10^6 J m^{-3} K^{-1}. This implies that the loam temperature increases/decreases about twice as water by absorbing/emitting the same amount of heat during the day/night. This fundamental physical property controls the model lower boundary surface temperature difference in our experiments. Due to the presence of water body over CB, the temperature increased by 2.0 - 3.0 K at night, while temperature decreased by 1.0 K in the day at

the northern CB (Fig. 2.10a, b). The night-time temperature increase over CB was distributed homogeneously across the northern and southern CB. However, the daytime temperature change showed a regional variation that temperature over the northern CB decreased by about 1 K compared to a decrease of only 0.1 K or even an increase of 0.1 K over the southern CB. The absolute value of temperature increase was larger than the temperature decrease. The obvious reason was that land (loam) emits longwave radiation and its temperature decreases fast, no matter of night or day. The absence of the shortwave radiation at night led to the temperature decrease over land relatively large. During the day, besides the longwave radiation emission, there was also shortwave radiation absorption. Land increased temperature faster than water while absorbing the same amount of heat. Thus, the water temperature was slightly lower during the day. The regional temperature variation also led to water vapor mixing ratio variability over CB. The resulting water vapor mixing ratio differences increased both at night (~ 2 g kg^{-1}) and in the day (~ 0.5 g kg^{-1}) (Fig. 10c, d). Similarly, the vertical velocity difference also changed from night to day (Fig. 10e, f). The vertical velocity changes were located at the western CB and also mostly at the northern CB. A velocity increase of about 0.005 m s^{-1} at the western shore of the northern CB at night and decreased by 0.002 m s^{-1} at the same location during the day, which was corresponding to the temperature difference shown in Fig. 10a, b. The positive water surface temperature change led to air ascending at night, while the negative water surface temperature change caused air to descend. The experiment showed that the water body modified the meteorology and dynamics of CB in a major way leading to the mixing and advection (via the prevailing winds). The higher surface temperature led to instability near the surface and more water vapor flux through the relatively higher vertical velocity, and hence flux that resulted.

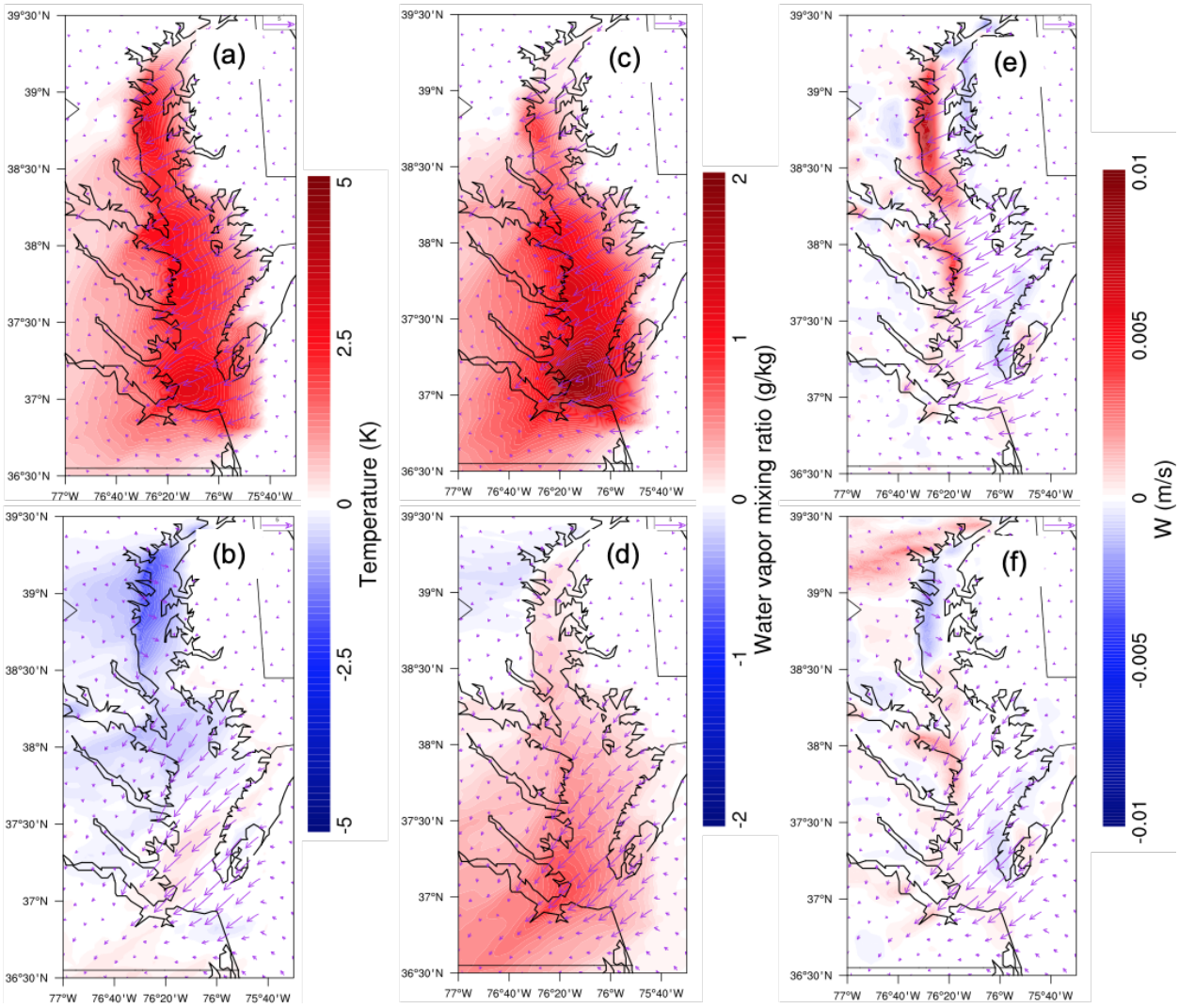

Fig. 2.10 WRF-Chem simulated absolute difference of temperature (a, b), water vapor mixing ratio (c, d), and vertical velocity (e, f) between simulations of baseline (water) and sensitivity (no water) experiments over CB

Pressure differences were observed from the baseline and sensitivity experiments. At night, the effect of CB increased the surface pressure over the western shore of northern CB, leading to the pressure gradient force pointing from west to east (Fig. 2.11a, c). This is consistent with Goldberg et al. (2014). The pressure gradient was a manifestation and contributed to the land breeze from the western offshore to CB. The resulting increased land breeze blew in opposition to the northeastern prevailing wind minimizing the wind difference over CB due to

the water body (Fig. 2.11a, c). During the daytime CB decreased pressure. The pressure gradient favored the prevailing wind and worked to reinforce the flow (Fig. 11b, d).

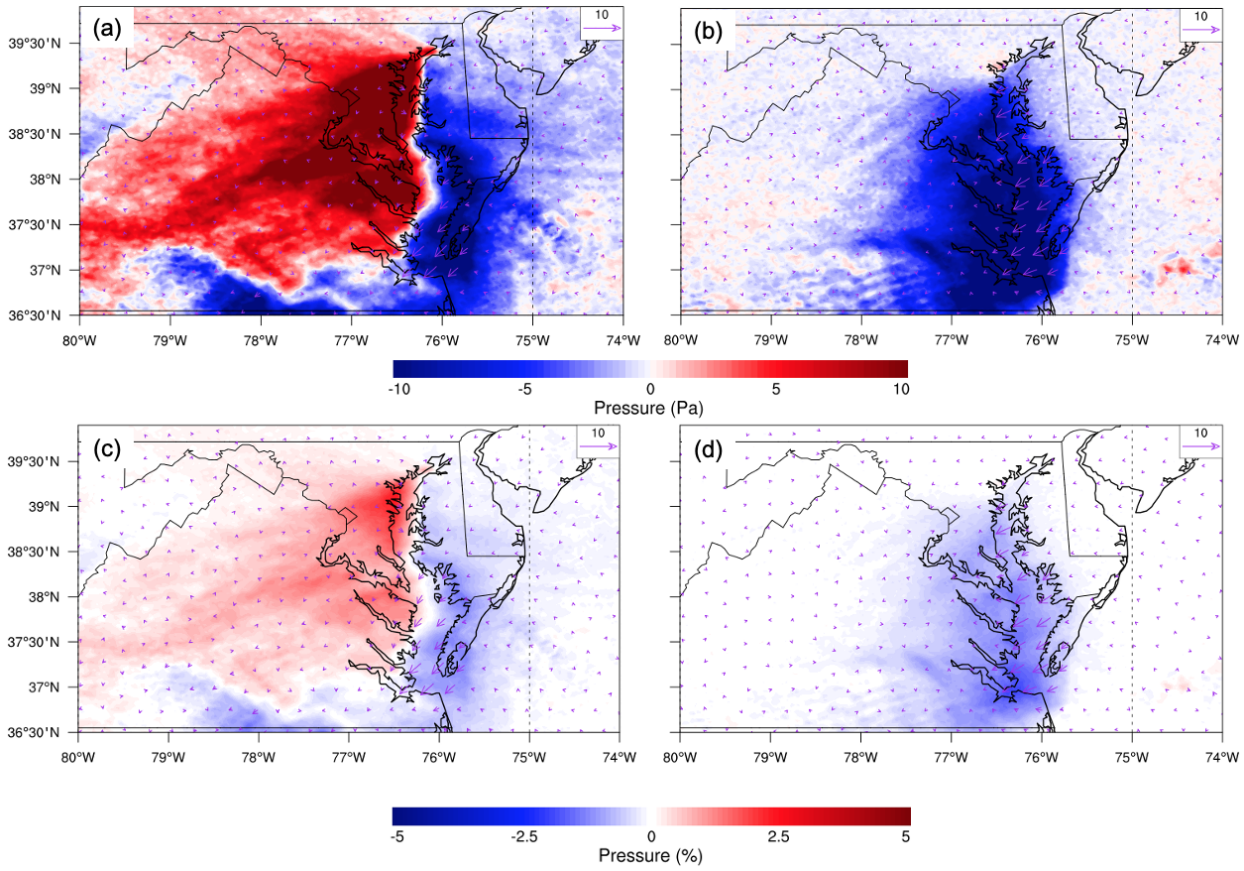

Fig. 2.11 (a) Averaged absolute surface pressure difference at night; (b) Same as (a), but in the day; (c) Averaged relative surface pressure difference at night; (d) Same as (c), but in the day

The differences of surface temperature, moisture, and vertical velocity have important influences on the stability and dynamics of the boundary layer. To investigate the stability consequences of these meteorological quantities, stability parameters were investigated. First, *gradient Richardson number (Ri)* defined as

$$Ri = \frac{\frac{g}{\theta_v}\frac{\partial \theta_v}{\partial z}}{[(\frac{\partial U}{\partial Z})^2 + (\frac{\partial V}{\partial Z})^2]} \quad (2.2)$$

The *gradient Richardson number* is a dynamical stability measure to determine if turbulence exists. g = 9.8 m s^{-2} is the *gravitational acceleration*. U and V are *horizontal velocities*. θ_v is the *virtual potential temperature* and can be calculated as

$$\theta_v = \theta(1 + 0.61r - r_L) \tag{2.3}$$

r is the *water vapor mixing ratio*, and r_L is the *liquid water mixing ratio* in the atmosphere. For the unsaturated atmosphere, $r_L = 0$. And $(\frac{\partial U}{\partial Z})^2 + (\frac{\partial V}{\partial Z})^2$ is the *wind shear squared*.

The root of the numerator in the eq (1) is the *Brunt-Väisälä frequency (N)*, a measure of buoyancy, is calculated by

$$N = (\frac{g}{\theta_v}\frac{\partial \theta_v}{\partial z})^{\frac{1}{2}} \tag{2.4}$$

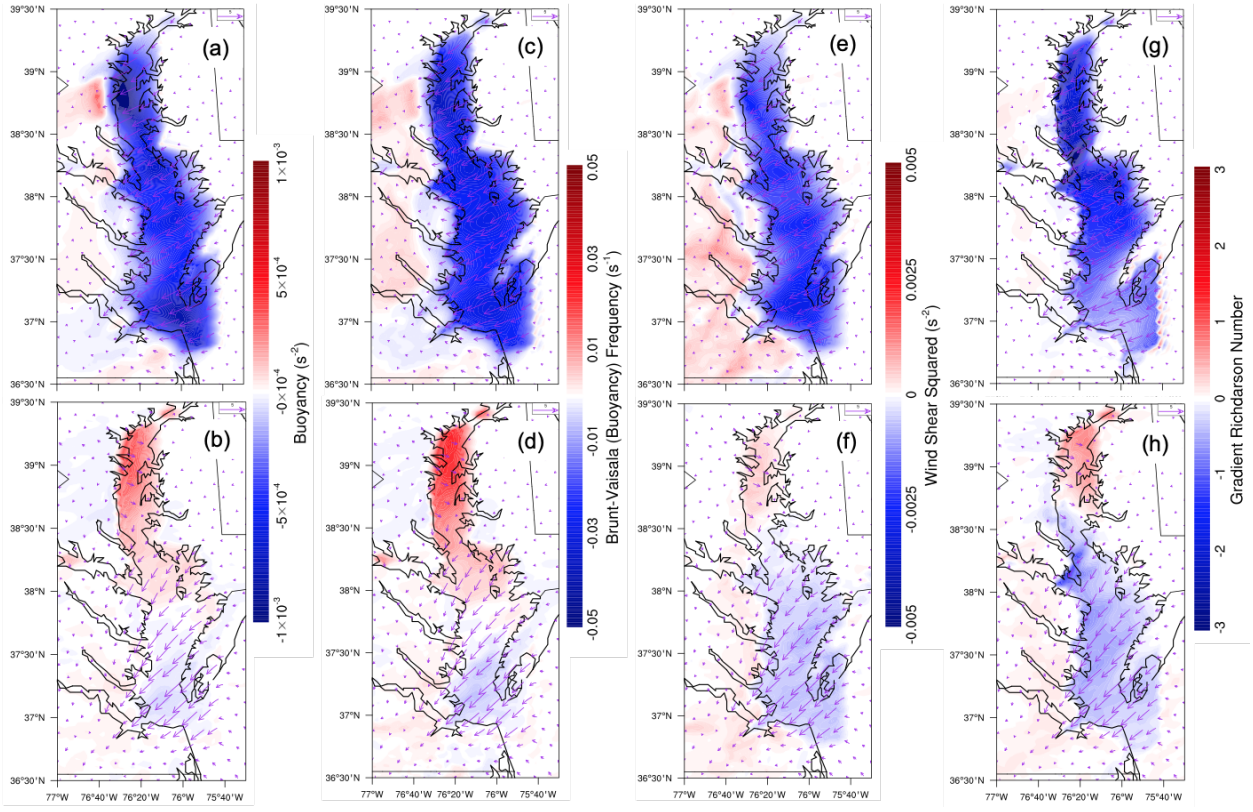

Fig. 2.12 Difference of WRF-Chem simulated variables related to stability during both night-time (1st row) and daytime (2nd row). (a) and (b) buoyancy; (c) and (d) Brunt-Väisälä (buoyancy) frequency; (e) and (f) wind shear squared; (g) and (h) gradient Richardson number

Figure 2.12 shows buoyancy, Brunt-Väisälä (buoyancy) frequency, wind shear squared, and gradient Richardson number at the surface, with relative decrease in magnitude and no regional preference at night. However, during the day, positive values for all parameters were found located over the northern CB while negative values at the southern CB.

At night, the buoyancy, Brunt-Väisälä (buoyancy) frequency, wind shear squared, and gradient Richardson number decreased due to the presence of CB (Fig. 2.12a, c, e, g). A relatively small water body surrounded by a large landmass over the northern CB led to a significant thermally induced perturbation in contrast to the southern CB. Relatively small surface wind differences were due to the water body and contributed to the atmospheric stability through wind shear. There was no regional preference of surface horizontal wind difference and thus its contribution to the instability was uniform over the entire CB (Fig. 2.12a, c, e, g). In addition to the surface temperature increase, the vertical velocity difference was positive over the northern and middle CB which contributes to the unstable condition (Fig. 2.10e). In the day, the surface wind differences at the northern CB were smaller than at night-time. The differences of buoyancy, Brunt-Väisälä (buoyancy) frequency, wind shear squared, and gradient Richardson number kept negative at the southern CB, and shifted to positive at the northern CB (Fig. 2.12b, d, f, h).

2.3.3.2 Vertical dynamical influence

Apart from the O_3 mixing ratio horizontal distribution, its vertical distribution also helps to understand how CB influences the O_3 three-dimensional distribution. The cross sections

should pass through the east-west, north-south, and center of CB. We selected six cross sections to visualize the vertical pictures around CB. The vertical cross sections of O_3 mixing ratio and water vapor mixing ratio were selected to characterize the role of CB on impacting their vertical distributions.

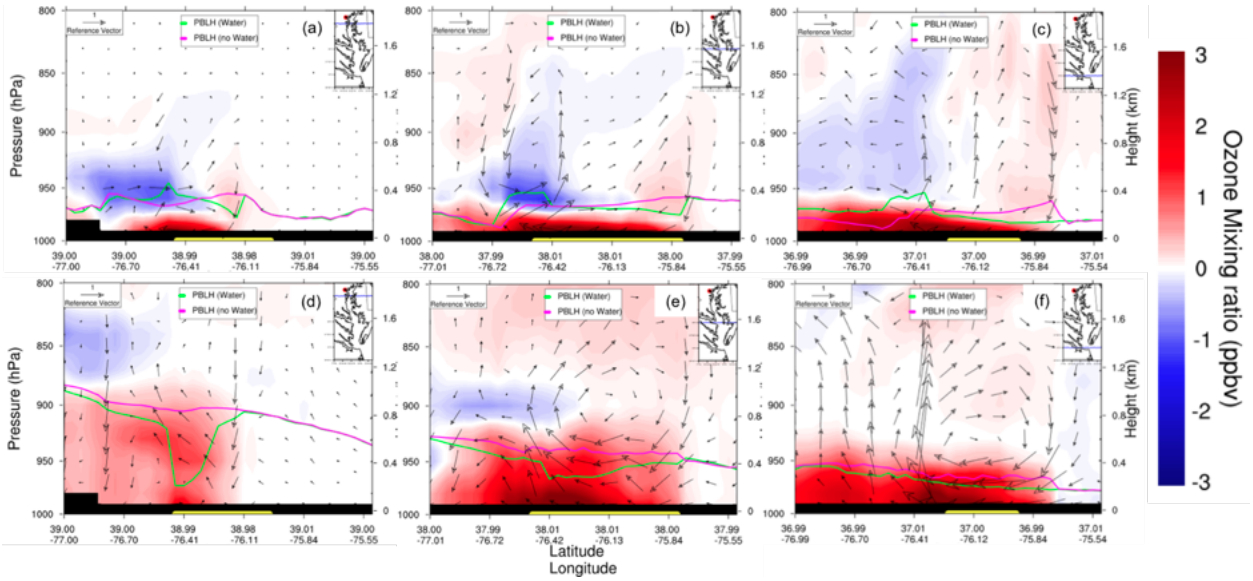

Fig. 2.13 WRF-Chem simulated O_3 mixing ratio vertical cross section (from west to east) difference (night: a, b, c; day: d, e, f). The green curve is the PBLH of water, and the pink curve is the PBLH of nowater. CB is denoted as the yellow bar. The upright insert map shows the location of the vertical cross section (blue line). Note that vertical wind is magnified by 50 times for the illustration purpose

Figure 2.13 shows the O_3 mixing ratio vertical distribution difference through the northern, central, and southern CB to distinguish the possible dynamic variations due to different parts over CB. The PBLHs are shown for both the baseline and sensitivity experiments. At night, O_3 was constrained within the shallow nocturnal boundary layer and the PBLH was less than 0.4 km, which led to the O_3 increase at night compared to daytime (Fig. 2.13a-c). The increased O_3 mixing ratio was found near the surface to increasingly intrude over the western shore via

transport by the night-time breeze and the northeast prevailing wind. The water body of CB increased the PBLH by about 0.1 km over the west shore of the northern CB. A subsidence of about 0.1 km in PBLH over the eastern CB was also evident due to, presumably, the resulting subsidence (Fig. 2.13a). Similar dynamics were observed at the cross sections over the middle and southern CB (Fig. 2.13b-c). After sunrise, resulting instability and convection increased the PBLH from 0.4 to 1.0 km. PBLHs were tilted from west to east of CB. The west is close to land terrain, which led to higher temperature during the day. While the east is near the Atlantic Ocean which had lower temperature during the day. All these factors diluted the O_3 mixture and transported O_3 to the free troposphere leading to surface O_3 mixing ratio difference decrease.

Another interesting point is the strength of the wind circulation in the vertical cross sections shown in Fig. 2.13. As the bay breeze moved from north to center to south, it became well defined and stronger (shown as circulations in Fig. 2.13e, f). At the northern CB transect, surrounded by land and far from the Atlantic Ocean, the simulated PBLH increased dramatically when the water body was replaced by land (loam), implying that the land surface contribution to the PBLH was large. This indicated the ability of absorbing large amounts of heat (shortwave radiation) with relatively little temperature change and resulting subsiding air over CB. The overall result was that the maximum O_3 mixing ratio difference was localized over the western CB, due to the shallow PBL with relatively weak bay breeze to ventilate the O_3 buildup. The change of PBLH was smaller in the central and southern transects where a much stronger breeze and shallower PBLH were observed.

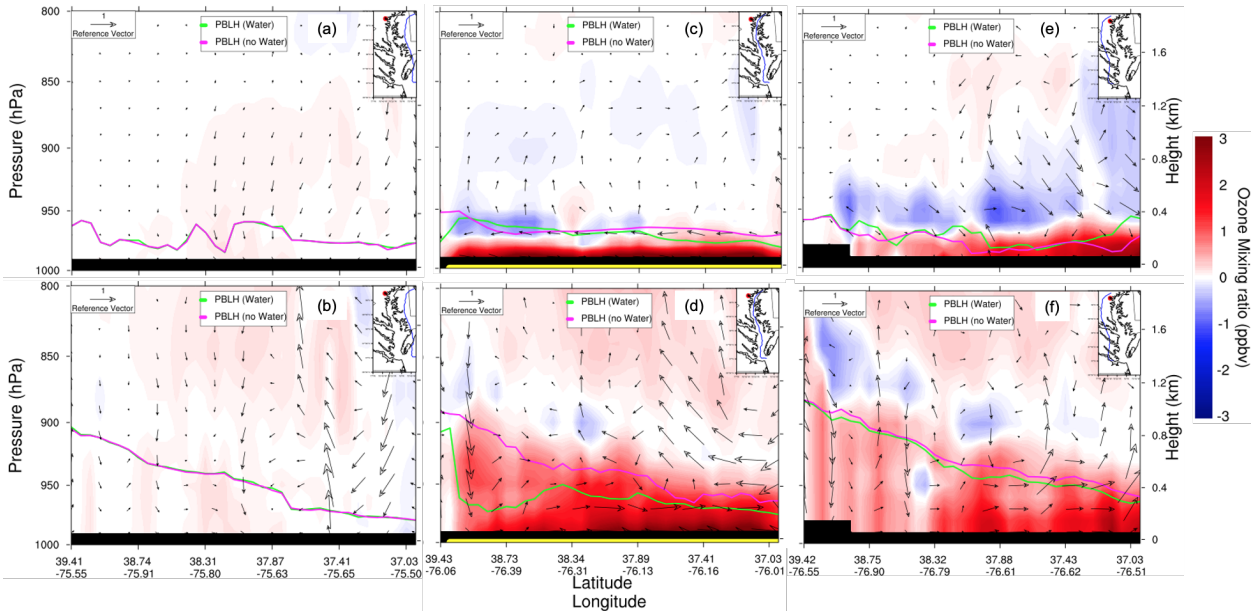

Fig. 2.14 WRF-Chem simulated O_3 mixing ratio vertical cross section (from north to south) difference (night: a, c, e; day: b, d, f). The green curve is the PBLH of water, and the pink curve is the PBLH of nowater. CB is denoted as the yellow bar. Note that vertical wind is magnified by 50 times for illustration purposes

Figure 2.14 shows O_3 mixing ratio north-south transects at the east, over, and west of CB, which confirms the significant influence of the water surface and associated bay dynamics on the O_3 mixing ratio and its distribution over and west of CB (Fig. 2.14c-f). While no influence is visible at the east of CB (Fig. 2.14a-b). The northeastern prevailing wind blew O_3 to the west after its generation from CB. In addition, Figure 2.14 shows the shallow and flat nocturnal PBLH (~ 0.2 km) at night as compared to the tilted and large PBLH in the day. We did not find the significant PBLH difference between water and nowater simulations at night-time. Whereas a totally different scenario unfolded for daytime PBLH over CB (Fig. 2.14d). While the water-influenced PBLH was similar to the sensitivity simulations on both west and east of CB, decreasing sharply from north to south, perhaps due to the water body area difference between northern and southern CB (Fig. 2.14b, f). The PBLH over CB from the baseline experiment was

much lower than the sensitivity experiment, approximately 0.8 km lower (Fig. 2.14d). This fact, as previously discussed, was the significant impact of the much smaller water body area over the northern CB.

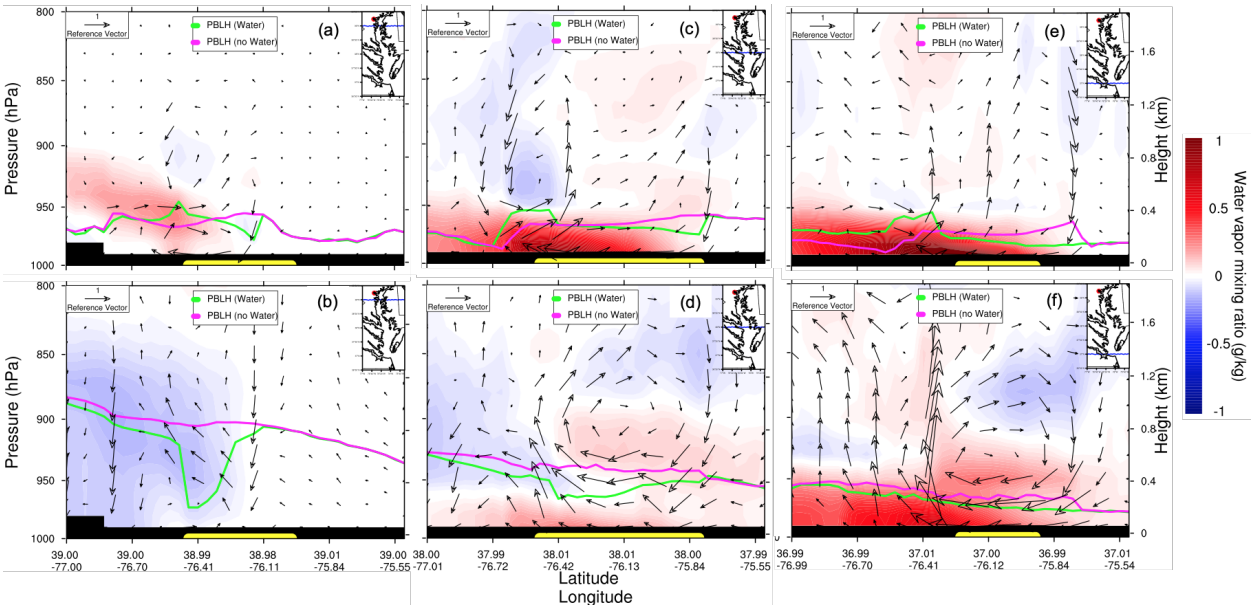

Fig. 2.15 Same as Fig. 14, but for water vapor mixing ratio

The water body in CB influenced the water vapor mixing ratio vertical distribution (Fig. 2.15). At night, the presence of CB increased the water vapor mixing ratio from north to south CB (Fig. 2.15a, c, e). The water vapor increased much less at the northern CB than the southern CB (Fig. 2.15a, e). While during the day, the water vapor mixing ratio increased less than night-time (Fig. 2.15d, f), or even decreased over the northern CB (Fig. 2.15b). The possible reason is that the temperature decreased (Fig. 2.10b).

2.4 Discussions and Conclusions

This paper investigates the influence of CB on the local O_3 pollution by employing the WRF-Chem model to simulate the O_3 concentration on 3 June 2015. In order to ensure the model accuracy, we first validated the model performance on simulating O_3 spatial distribution and time

evolution using AirNow surface O_3 observations. Through the comparison between baseline and sensitivity experiments over CB by altering the surface type of CB from water to land (loam), dynamical differences due to CB are analyzed thoroughly from both horizontal and vertical directions. The findings show that CB elevates the O_3 mixing ratio both at night-time and daytime, but with discrepant reasons.

The model simulated O_3 mixing ratio overall agreed with AirNow O_3 observations, even though it overestimated near mountains and underestimated over New Jersey and Delaware. The higher O_3 mixing ratio over CB had been decidedly confirmed from the perspective of model simulation, which was consistent with the previous studies over CB (Loughner et al., 2011; He et al., 2014; Goldberg et al., 2014). Shallower boundary layer decreased the surface O_3 vertical dilution, especially at the northern CB, which led to relatively high O_3 concentration close to the surface. Strong bay breeze caused O_3 accumulating in the downwind region near CB. Taking the model uncertainty into account, the surface O_3 mixing ratio increased by 10 % at night and 5 % in the day. The O_3 mixing ratio difference gradient was negative over the eastern shore while positive over the western shore, which indicated the O_3 mixing ratio difference increased from the eastern shore to the western shore due to the northeastern prevailing winds. From the O_3 mixing ratio diurnal variation difference between baseline and sensitivity experiments, water increased O_3 by 5 ppbv (25 %) at night and 2 ppbv (15 %) during the day. The water body increased temperature by 2 ~ 3 K at night and decreased it by 1.0 K during the day, and increased water vapor mixing ratio by 2 g kg^{-1} at night and 0.5 K in the day, and increased vertical velocity by 0.005 m s^{-1} at night and decreased it by 0.002 m s^{-1}.

The vertical distributions of O_3 mixing ratio and water vapor mixing ratio shows the vertical influence of CB. The west-east cross sections located at the northern, central, and

southern CB showed that O_3 was confined within PBL, which reached 0.2 km at night and extended to 0.8-1.0 km in the day (tilted PBL). Due to mountains located over the west and north of CB and water (the Atlantic Ocean) over the east of CB, PBL was tilted with higher PBL over the west and north and lower PBL over the south in the day. The bay breeze was relatively stronger at the central and southern CB in the day than other locations and at night.

Apart from field campaigns, this work shines a light on how to employ models to study the influence of CB on O_3 mixing ratio thoroughly, since models provide us the flexibility to eliminate CB. This helps us to quantify the O_3 concentration difference between with and without CB, even though the model error attributes some uncertainties to this estimation which is the limitation of this study. The merits are providing us a novel method to study the CB influence on O_3 in three dimensions, which could not be deployed by field campaigns. As models are further developed, the model errors become smaller, analogous work in the future will be more reliable.

In addition, due to the existence of CB, it is possible that cloud fraction increases or decreases. From the sensitivity experiment, CB increases the water vapor both night and day, which may increase the cloud fraction. In this case, cloud blocks sun light (solar radiation) during daytime, and less sun light arrives at the surface. It will reduce the photochemical reactions, which can be treated as the potential 2nd order effects beyond dynamics. On the other hand, the CB lowers the boundary layer, which may reduce the cloud coverage. To quantify the impacts of the CB on the cloud fraction, more experiments need to be done.

Chapter 3

Long-range transported Canadian wildfire influence on ozone and particle pollution

This chapter is organized as follows: a description of the model configuration and study domain is given in section 3.2, followed by a discussion of the background, case study, and data sets in section 3.3. Results and analysis are given in section 3.4 and concluding remarks are presented in section 3.5.

3.1 Study region, model configuration, and experiment design

3.1.1 Study region

The model study area includes southern Canada and the contiguous U.S. to cover the wildfire source region (Saskatchewan, Canada) and smoke transport paths (indicated by the yellow line in Fig. 1) and provide lateral boundary conditions for the nested domains. This outer domain is further resolved by two nested regions that progressively focus and center at the local study region, Baltimore-Washington, D.C. metropolis. Thus, three domains are established with the spatial resolution of 27 km (d01) and two nested domains at 9 km (d02) and 3 km (d03), respectively. The first nested domain (d02) is designed to capture the path of the smoke transport through the Great Lakes and the Ohio River Valley which borders the study region in the immediate Northeast and on the path of several space lidar data transect observations used for comparison. The second nested domain (d03) is selected to allow for focused and detailed comparisons with air quality investigation and observation over the Baltimore-Washington, D.C. metropolis. The model vertical grid uses 65 levels with a model top at 100 hPa and about 35 levels were set below 700 hPa, in order to provide model output that would resolve the PBL.

Fig. 3.1 WRF-Chem study area with outer domain (southern Canada and the contiguous U.S.) two nested domains (white rectangle (d02) and red rectangle (d03)). The fire icons indicate the wildfire source locations and the yellow line indicates the approximate smoke transport path as can best be deduced from satellite observations.

3.1.2 Model configuration and emissions

3.1.2.1 Model configuration

WRF-Chem version 3.9 has the air quality components consistent with the meteorological components (Grell et al., 2005; Fast et al., 2006). In this study, the gas-phase chemistry and aerosol module employs the Carbon Bond Mechanism-Version Z (CBM-Z, Zaveri and Peters, 1999) and Model for Simulating Aerosol Interactions and Chemistry (MOSAIC, Zaveri et al., 2008), respectively. The Yonsei University PBL scheme is selected (YSU, Hong et al., 1996; 2006). An extended discussion of the different model PBL parameterization schemes and their success in comparison with lidar observed PBL data in this study region is reported by Lopez et al. (2020). Model radiation treatment utilizes the Rapid Radiative Transfer Model for General Circulation Models short-wave and long-wave radiation schemes (RRTMG, Iacono et al., 2008), including the aerosol radiation feedback.

3.1.2.2 Emission data sets

All the emission data sets used in this study are listed in Table 3.1. Wildfire emissions are the Fire INventory from NCAR (FINN). It is retrieved from satellite observations (MODIS) of active fires and land cover, together with emission factors and estimated fuel loadings to provide daily, 1-km resolution open burning emissions estimates (Wiedinmyer et al. 2006; 2011). Anthropogenic emissions are from the 2011 National Emission Inventory (NEI2011). The NEI2011 is a comprehensive and detailed estimate of the air emissions for criteria pollutants, precursors, and hazardous air pollutants. It includes point sources and area sources with resolution of 4 km, covering all the 48 contiguous states as well as selected regions of Canada and Mexico. Biogenic emissions are from the Model of Emissions of Gases and Aerosols from Nature (MEGAN), which is a modeling system for estimating the net emission of gases and aerosols from terrestrial ecosystems into the atmosphere (Guenther et al., 2006). It is driven by land cover, weather, and atmospheric chemical composition and has 1 km resolution globally.

Dataset	Full Name	Resolution	Parameters	Availability
FINN	Fire Inventory from NCAR	$1\times1km^2$ (H) hourly	CO, CO_2, NOx, SO_2, VOC, PM, OC, BC, etc	2002-2018
NEI2011	National Emission Inventory (2011)	$4\times4km^2$ (H) hourly	CO, NOx, SO_2, VOC, PM, OC, BC, etc	2011

Table 3.1. Emission data sets as inputs of WRF-Chem.

H: Horizontal

3.1.3 Experiment design

Three numerical experiments were performed to investigate and quantify the impacts of different emissions (Table 3.2). The first numerical experiment (Ex1) is designed to quantify the

anthropogenic and biogenic emission influence on O_3 and PM. This experiment helps us understand the O_3 and PM pollution without the transported Canadian wildfire smoke. The second numerical experiment (Ex2) is conducted with only fire emissions to quantify the contribution of the Canadian wildfire smoke to the elevated O_3 and PM pollution in the Mid-Atlantic region. The third numerical experiment (Ex3) includes anthropogenic, biogenic, and fire emissions, to evaluate the model performance with observations, since this is the closest situation to reality.

Experiment	Biogenic emission	Anthropogenic emission	Fire emission	Purpose
Ex1	MEGAN	NEI2011	N/A	anthropogenic and biogenic emission influences
Ex2	N/A	N/A	FINN	fire emission influences
Ex3	MEGAN	NEI2011	FINN	anthropogenic, biogenic, and fire emission influences

Table 3.2. Experiments designed to quantify the emission influences on the air quality.

3.2 Data

A summary of the observation data used in this study is given in Table 3.3 followed by a brief explanation of each data set.

Dataset	Full Name	Spatial & Temporal Resolution	Parameters	Availability
AirNow	EPA AirNow	hourly (H)	O_3, $PM_{2.5}$, PM_{10}, SO_2, CO, NO_2, VOC, NOx, NOy, lead,	1980-2020

			pressure, temperature, relative humidity, wind	
Ozonesonde			O_3 mixing ratio, O_3 partial pressure, altitude, water vapor mixing ratio, relative humidity, pressure, and temperature	12 Jun 2015
TROPOZ DIAL	TROPospheric OZone DIfferential Absorption Lidar	15m (V) 6min	O_3 mixing ratio, pressure, temperature, etc	10-12 Jun 2015
Vaisala Ceilometer CL51		15m (V) 15s	Attenuated backscatter, Cloud base height, Cloud depth	10-12 Jun 2015
MODIS	Moderate Resolution Imaging Spectrora - diometer	$1\times1km^2$ (H)	AOD	Dec 1999~Now (Terra) May 2002~Now (Aqua)
CALIOP	Cloud-Aerosol Lidar with	5km, 40km/60m, 120m (H/V)	Extinction Coefficient, Vertical Feature Mask	Apr 2006

	Orthogonal Polarization

Table 3.3. Observation data sets used in this study.

H: Horizontal; V: Vertical

3.2.1 Standard surface and upper air O_3 data

The U.S. Environmental Protection Agency (EPA) collects observation data from a network of surface O_3 and PM monitoring and detection that covers a large spatial region within the U.S. in the last few decades (Dye et al., 2004). The EPA's AirNow program provides real-time forecast and observed surface air quality information across the U.S. over 1000 monitoring stations. AirNow data from surface stations in Maryland within the inner nested domain (d03) is used for the surface validation of the WRF-Chem model simulation.

Ozonesonde relies on the oxidation reaction of O_3 with potassium iodide in solution launched by the Howard University Beltsville Campus routinely (HUBC, 39.06°N, 76.87°W, 52 meters above sea level, Komhyr et al., 1995). Ozonesonde observed O_3 vertical profiles resolve the O_3 vertical distribution and evaluate model simulated O_3 vertical distribution.

3.2.2 Ground-based remote sensing data

This work uses data from a ground-based lidar and ceilometer: the NASA Goddard Space Flight Center TROPospheric OZone DIfferential Absorption Lidar (TROPOZ O_3 lidar; Sullivan et al., 2014) and a Vaisala Ceilometer CL51. During the deployment, the TROPOZ and CL51 were operated from HUBC.

The TROPOZ O_3 lidar has been developed in a transportable trailer to take routine measurements of tropospheric O_3 (Sullivan et al., 2014). The laser wavelength is 289 nm, and the pulse frequency is 50 Hz to measure the differential absorption of atmospheric backscatter

profiles and retrieve the O_3 number density (which can be converted to mixing ratio) vertical distribution whose native sampling resolution is 15 m with an effective vertical resolution between 100-500 m throughout the free troposphere and boundary layer. Its O_3 vertical profile extends from 100 m above the surface to 12 km. But this study only employs TROPOZ O_3 profiles from 0.1025 km to 2.5 km, where its data are available. TROPOZ O_3 lidar is a charter member of the ground-based Tropospheric Ozone Lidar NETwork (TOLNET) which is designated to improve the current number of tropospheric O_3 profiles (Newchurch et al., 2016; https://www-air.larc.nasa.gov/missions/TOLNet/). In this study, TROPOZ O_3 profiles are used to resolve the O_3 profile temporal evolution and evaluate model simulated O_3 vertical distribution.

Vaisala Ceilometer CL51 is designed to measure the total backscatter profile from the atmosphere and reach up to cirrus cloud heights. The aerosol backscatter profile could be retrieved after applying the correction for the molecular atmosphere and filtering clouds out. It is a commercial lidar that uses a low power indium gallium arsenide laser diode (InGasAs) laser at the wavelength of 910 nm and is primarily used for cloud base reporting with its range reaching up to 13 km. It is one of the candidate instruments for mixed layer height detection and reporting over EPA's Photochemical Assessment Monitoring Stations (PAMS, Caicedo et al., 2020). CL51 backscatter profile observations have been used to study the evolution of the PBL and indicator for air mass change associated with atmospheric dynamics (Carroll et al. 2019). In this study, Ceilometer CL51 data is used to indicate the approximate range of the transported wildfire smoke and its mixing down into the surface as well as to visually indicate the PBL height (PBLH) evolution

3.2.3 Satellite-based data: AOD and VFM profile

The Moderate Resolution Imaging Spectro-radiometer (MODIS) instruments aboard Terra (launched in December 1999) and Aqua (launched in May 2002) satellites measure spectral radiance in 36 channels, with resolutions ranging from 250 m to 1 km at nadir. Three of these channels (470 nm, 660 nm, and 2130 nm) are used to retrieve standard AOD, which is interpolated in the mid-visible spectrum (550nm). MODIS AOD is reported to have an uncertainty of $\pm (0.05 + 0.15\tau)$ over dark land and $\pm (0.04 + 0.10\tau)$ over ocean, where τ is the MODIS retrieved AOD (Levy et al., 2015). In this work, MODIS aerosol Level 2 Collection 6.1 products (MOD_04 and MYD_04 from Terra and Aqua, respectively) are used to track the large-scale smoke transport and compare with model simulations.

The Cloud-Aerosol Lidar with Orthogonal Polarization (CALIOP) is a two-wavelength polarization active lidar aboard the CALIPSO satellite (Cloud-Aerosol Lidar and Infrared Pathfinder Satellite Observations, Winker et al., 2009). CALIOP performs global profiling of aerosols and clouds in the troposphere and lower stratosphere. CALIOP Level 2 processing involves separating the aerosol and cloud layers followed by determining the aerosol types (smoke, polluted dust, clean continental, polluted continental, dust, and clean marine) and cloud ice-water phase (Liu et al., 2004; 2009; Omar et al., 2009; Winker et al., 2009). The CALIOP Vertical Feature Mask (VFM) Level 2 products are selected to track the smoke vertical distribution and evaluate model vertical profile simulations of the aerosol mass concentration.

3.3 Results

3.3.1 Case description: wildfire event of 6 June 2015

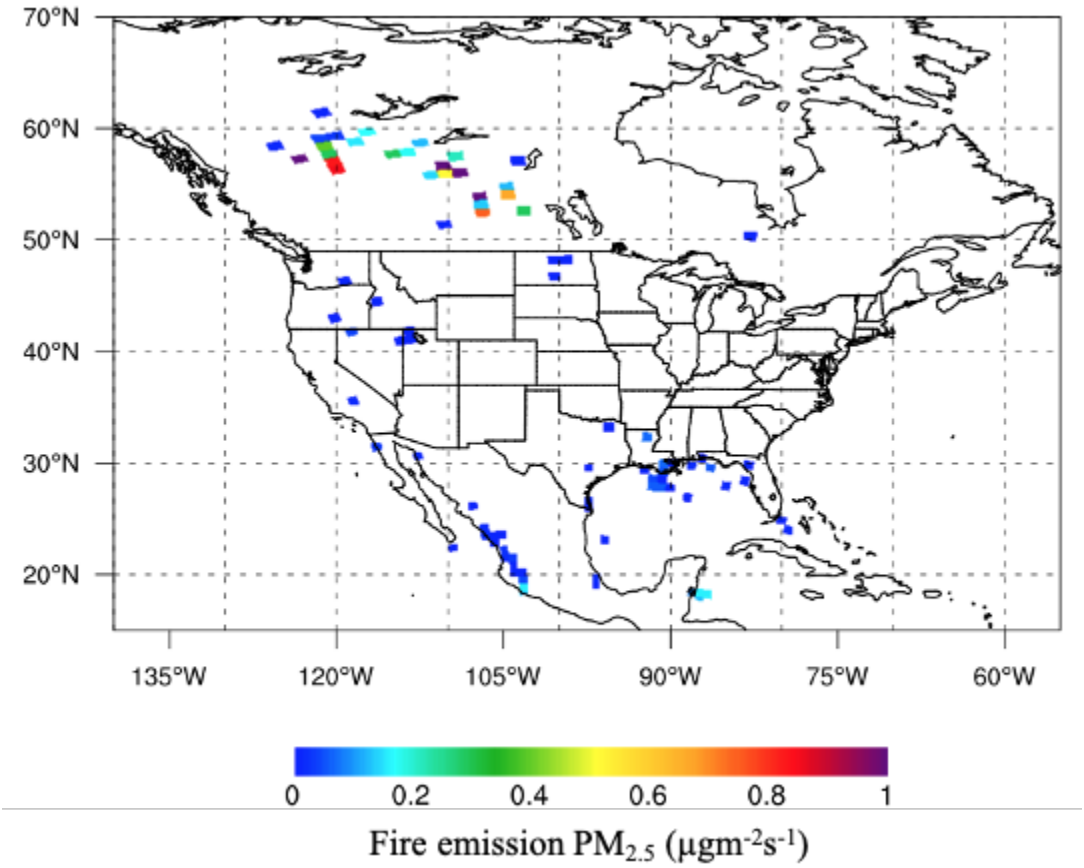

Fig. 3.2 The $PM_{2.5}$ mass flux rate of FINN fire emission at 2200 UTC on 6 June 2015.

This case is a long-range transported smoke generated by wildfires over the western Canada. This Canadian wildfire event was ignited by lightning at the southwest of the Great Slave Lake and south of the Lake Athabasca in the Alberta and Saskatchewan Provinces on 6 June 2015 (Canadian Interagency Forest Fire Centre [CIFFC], 2020). Abnormally warm and dry weather readily resulted in conditions that favor lightning-induced wildfire over the boreal forest in Canada (Dreessen et al., 2016). The fire source region was identified from the FINN fire emission $PM_{2.5}$ mass flux rate, which was over 1.0 μg m^{-2} s^{-1} at 2200 UTC on 6 June 2015 (Fig. 2).

3.3.2 Long-range transport of fire-induced smoke

3.3.2.1 Smoke horizontal transport from the source to the study region

A combination of MODIS AOD and CALIOP VFM profile imagery as well as model simulations are used to diagnose and reveal the three-dimensional (3D) long-range transport path of the smoke from the source region to the U.S. The shortcomings of the polar-orbiting satellite imagery that are limited to only twice daytime snapshots daily are augmented by the capability of model simulations with fine integral time intervals and output results from every hour to a few minutes. Careful analysis of these satellite images and model simulations revealed four key regions as the smoke was transported from Canada to the U.S. (not shown here): the source region, Lake Michigan, Ohio River Valley, and Mid-Atlantic and Northeast.

After emitted from the wildfire, the smoke was lifted via positive buoyancy, driven by the fire radiative power as described in Peterson et al. (2013) and Freeborn et al. (2014). Associated physics, due to radiative cooling combined with efficient heat transport by convection, led to a rapid decay of temperature above the burning area. The WRF-Chem model simulates this process in which smoke emissions are lifted to a certain vertical model level due to heat flux (Grell et al., 2011). In the WRF-Chem plume rise module, land cover types include tropical forest, boreal forest, Cerrado (or woody savanna), and grassland (or cropland), each of which has its own minimum and maximum heat fluxes. For example, boreal forest has the minimum and maximum heat fluxes of 30.0 kW m^{-2} and 80.0 kW m^{-2}, respectively. Thus, the plume injection height in the model is determined by a combination of factors including the land cover types, their fractions in each model mesh, and burned area. The spatial span of the wildfire source region was 105° W - 115° W and 55° N - 60° N, which included multiple fire events, leading to the tremendous amount of smoke emissions. At the time, the northwest prevailing winds and a

cold front impacted the fire source region from the northwest advecting the smoke further southeast as can be seen in the daily weather maps available from NOAA (available at https://www.wpc.ncep.noaa.gov/dailywxmap/index_20150606.html).

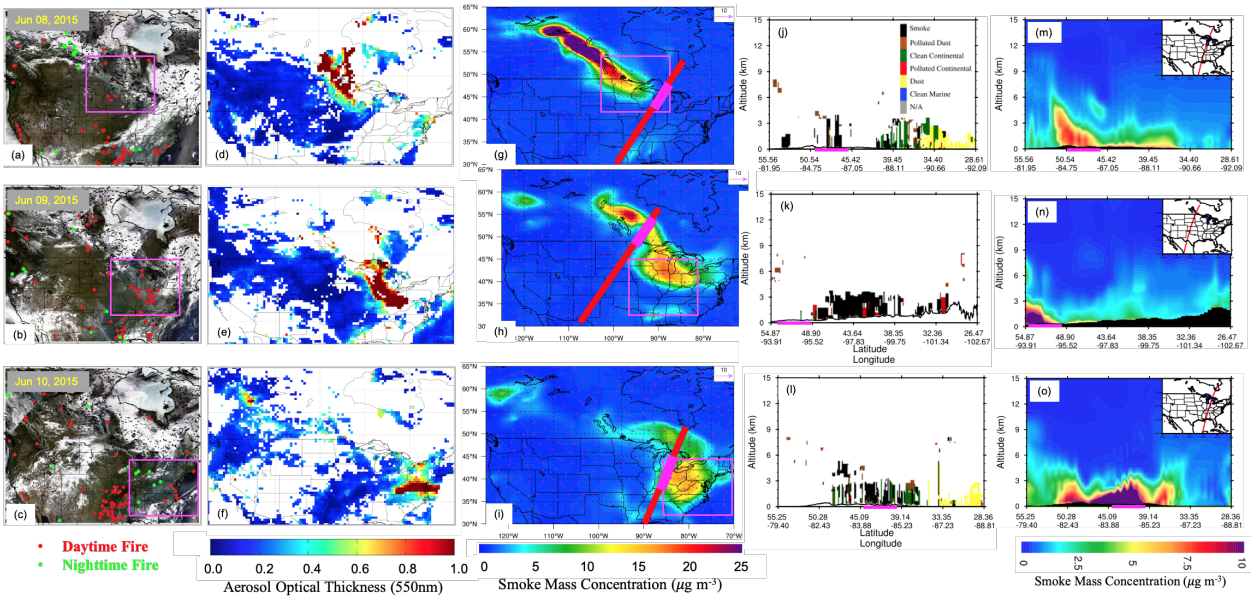

Fig. 3.3 Panels (a-c): MODIS three-band color overlay images (band 1—red, band 4—green, and band 3—blue) from Terra on 8, 9, and 10 June 2015. Red and green dots indicate the locations of fires detected by MODIS at daytime and nighttime, respectively. Panels (d-f): MODIS AODs at 550 nm. Panels (g-i): WRF-Chem simulated surface $PM_{2.5}$ mass concentration (Ex2). The pink rectangles indicate where the smoke front is. Panels (j-l): CALIOP-derived vertical feature mask. Panels (m-o): WRF-Chem simulated $PM_{2.5}$ mass concentration vertical cross section along the CALIPSO ground track. The inset on the upper right shows the CALIPSO ground track (red curve).

The model simulation (Ex2) revealed that the enhanced surface $PM_{2.5}$ mass concentration contributed by smoke was about 15 μg m^{-3} in Minnesota on 8 June (Fig. 3.3a, d, g). 9 June, the fire-induced smoke arrived at the Ohio River Valley, located over Indiana and Ohio. The surface wind was west and wind speed was 10 m s^{-1} (Fig. 3.3b, e, h). Nevertheless, the wind direction

shifted towards south at midnight on 10 June and lasted for 12 h before shifting back to southwest at noon on 10 June. Because of the wind shift, the smoke was trapped over the Ohio River Valley for more than one day, leading to the stagnant smoke and mixing with the local air pollutants. Despite both wet and dry deposition, the PM concentration kept stable and did not decrease much. On 10 June, the transported smoke arrived at the Mid-Atlantic region (Fig. 3.3c, f, i). An opposing flow from the southeast over the region blocked the smoke-filled air mass and concentrated it along a relatively narrow band region as observed on 11 June.

3.3.2.2 Evolution of the smoke-laden air vertical structure

CALIOP data was used to track the smoke vertical distribution as it was transported to the Mid-Atlantic region. The CALIOP VFM product which classifies aerosol types, e.g., smoke, dust, polluted dust, clean continental, polluted continental, and clean marine is shown in Fig. 3.3j-l. The black color indicates smoke.

The CALIPSO ground track passed over the southeast of Wisconsin and CALIOP detected the smoke in the afternoon of 8 June, around 0830 UTC (1330 CDT[1]). The smoke transport path overlaid with the CALIPSO ground track is indicated with a pink line in Fig. 3.3g and as a pink bar in Fig. 3.3j & m. The smoke between 45° N and 50° N was about 5 km deep, similar to the simulation with FINN fire emissions (Ex2) results (Fig. 3m). In addition, the model simulation showed the continuous smoke vertical distribution along the CALIPSO ground track. As the smoke drifted further south into the U.S., with the bulk of it over the Mid-Atlantic, CALIOP showed very little smoke detected, primarily because clouds blocked detection of the smoke beneath (Fig. 3.3k).

[1] CDT: Central Daylight Time, CDT = UTC - 5:00

The CALIOP data intercepted the smoke layer as it passed Lake Michigan and arrived over the Mid-Atlantic showing a general "settling" of the smoke plume layer to about 3 km deep (pink bar, Fig. 3l). The model simulation captured the general vertical smoke transport compared with the CALIOP product, as well as the plume height (Fig. 3.3o).

3.3.3 Local O_3 and PM enhancement

3.3.3.1 Local wind profile evolution

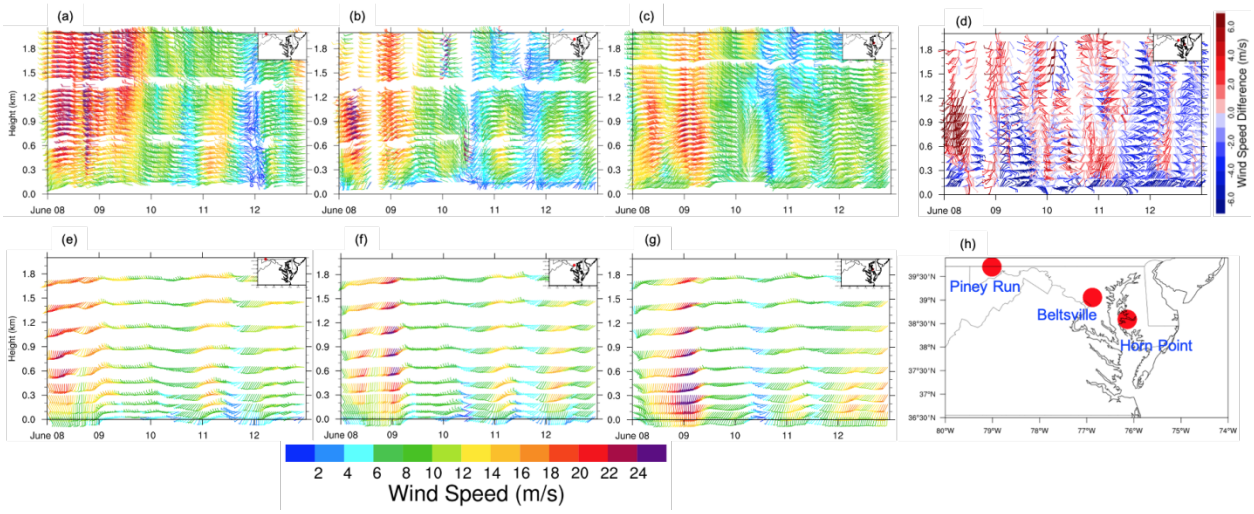

Fig. 3.4 915 MHz wind radar and WRF-Chem simulated horizontal wind speed and direction vertical profiles at three sites on 8-12 June 2015. The top row is the wind radar observation. The bottom row is the WRF-Chem simulation. (a) and (e), Piney Run; (b) and (f), Beltsville; (c) and (g), Horn Point; (d), wind difference between Beltsville and Horn Point; (h), three site locations on the map.

Transport of the smoke plume in any numerical weather model primarily depends on the quality of the 3D wind simulations, at least on the average large-scale character. Small scale perturbations are not easy to reproduce by a regional model. The simulated vertical wind profile is evaluated using 915 MHz wind radar profiler observations. Figure 3.4 shows the observed and simulated vertical wind profiles on 8-12 June at Piney Run, Beltsville, and Horn Point. Also,

shown is the observed vertical wind profile differences between Beltsville and Horn Point (Fig. 3.4d). The radar profile data is missing at 0.6 km and 1.3 at Piney Run and Beltsville, and 1.6 km at Horn Point. The Piney Run station is located in the rural area over a mountain range in the Appalachian mountains. The Beltsville station is located in the suburban area between Baltimore and Washington D.C., and the western shore of the Chesapeake Bay. While the Horn Point station is in the coastal area at the eastern shore of the Chesapeake Bay (Fig. 3.4h).

The wind speed at three stations appeared low near the surface and increased with altitude, from 10.0 m s^{-1} at 0.3 km to over 20.0 m s^{-1} at 2.0 km on 8-9 June. Starting late 9 June, the wind speed further decreased to 2.0-4.0 m s^{-1} from the surface to 2.0 km. This decrease was pronounced over Beltsville and Horn Point veering from south near the surface to west aloft. The wind speed followed significant diurnal variations, with low wind speed near 0000 UTC and high wind speed at 0600 UTC. The overall wind direction was west, shifted to south close to the surface on 8-12 June, and this is the reason that the fire smoke was advected from the Mid-Atlantic region to the Northeast.

The wind direction at Beltsville was south near the surface while shifted to west above 0.6 km. Its wind speed was lower than Piney Run, while they had similar wind patterns (Fig. 3.4b, f). The strongest wind happened on 8 June, with relatively low wind speed around 10.0 m s^{-1} from surface to 0.3 km, and reached 20.0 m s^{-1} at higher levels. Other than that, the wind speed was around 10.0-12.0 m s^{-1} on 10-12 June. Its wind speed diurnal variation was similar to Piney Run.

The wind direction at Horn Point was south near the surface and shifted slightly to west above 0.3 km (Fig. 3.4c, g). Its wind speed was lower than Piney Run and Beltsville on 8 June. While it had stronger wind afterwards, due to the contribution of the south wind over CB. It also

maintained the wind speed diurnal variation but with smaller wind speed contraction between daytime and nighttime. This was caused by the water body over CB. The high relative heat capacity of water kept the surface temperature change smaller than the land surface between daytime and nighttime.

The vertical wind profile differences between Beltsville and Horn Point show north winds below 0.3 km, indicating stronger south wind over Horn Point while the differences were east during daytime and west or south at nighttime. This change was influenced by the occurrence of the bay breeze which frequently occurs (Loughner et al., 2011). The stronger and opposing winds at Horn Point compared to Beltsville acted in such a way to block the efficient air mass advection and transport from west-to-east and lead to stagnation of smoke.

The WRF-Chem simulated winds at these three stations agree with the observed winds evolution (Fig 3.4e, f, g). The wind direction, strength, and character as well as the periodicity and strength of the lowest 2 km of the troposphere is simulated well and hints at a correct simulation of the smoke advection and timing. The model-observation comparison is a reason for strong confidence on the validity of the WRF-Chem smoke transport location and character used here for discussion of its impact on O_3 and PM measurements at surface and profile over the Beltsville station.

3.3.3.2 Surface O_3 diurnal variation

The observed and simulated surface O_3 mixing ratios show significant diurnal variations. Ex1 and Ex3 simulation results were employed to analyze the impacts of smoke on the O_3 diurnal variation. The WRF-Chem model simulated surface O_3 mixing ratio was generated by averaging three by three model meshes surrounding the selected station (nine meshes in total). The TROPOZ O_3 lidar data is included for comparison purposes. This lidar profile starts at 102.5 m

above ground level and has uncertainty of about 10 % (Sullivan et al., 2014). What is plotted is an average of the first 10-levels of TROPOZ data (102.5-237.5 m). The larger TROPOZ data compared to AirNow surface measurements is expected as the TROPOZ O_3 profile shows O_3 mixing ratio increased from the surface to 500 m in Fig. 3.7d, but is indicative of near-surface O_3 concentration.

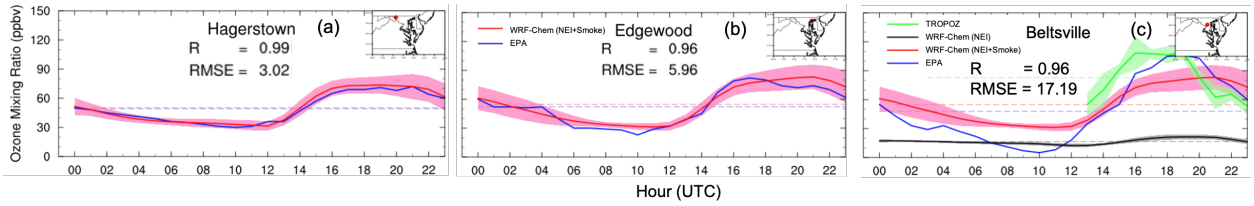

Fig. 3.5 Diurnal variations of the surface O_3 mixing ratio of EPA AirNow, TROPOZ and WRF-Chem simulation at sites: (a) Hagerstown (rural), (b) Edgewood (coastal), and (c) Beltsville (suburban) on 12 June, 2015. The red shaded areas indicate standard deviations of the WRF-Chem simulation; and surface O_3 concentration daily averages are denoted as dashed lines. The location of the station is indicated by a red dot on a map in the upper right corner. Pearson correlation coefficients and RMSEs between EPA AirNow and WRF-Chem simulation are provided.

The surface O_3 diurnal evolutions on 12 June at Hagerstown, Edgewood, and Beltsville are shown in Fig. 3.5. The diurnal variability shows generally a similar trend and the daily average values are very small. At Hagerstown, the magnitude and diurnal pattern of model simulated and AirNow observed O_3 mixing ratio diurnal variations agree well, with slight and consistent model overestimation during daytime (Fig. 3.5a). The model-observation Pearson correlation coefficient and root mean square error (RMSE) was 0.99 and 3.02 ppbv, respectively. At Edgewood, a well-known and significant O_3 pollution station (see Crawford and Pickering, 2014), the model simulated surface O_3 agreed well with the observed O_3, although the model

simulated O_3 diurnal variation was relatively smooth. The model-observation Pearson correlation coefficient was 0.96 and RMSE was 5.96 ppbv. The daily model averaged O_3 mixing ratio was 55 ppbv. The comparison between Hagerstown and Edgewood showed the similarities and differences between two stations. The similarity was the O_3 mixing ratio diurnal variation, while the difference was the maximum O_3 mixing ratio. The daytime maximum O_3 mixing ratio was 70 ppbv at Hagerstown, while 85 ppbv at Edgewood. Another difference is the time when the maximum O_3 occurred and how long it lasted. At Hagerstown, the daytime O_3 mixing ratio was very smooth after reaching maximum at 1600 UTC and lasted until the end of day (1200 EST, Fig. 5a). However, at Edgewood, the O_3 mixing ratio reached the maximum at 1600 UTC (1200 EST) and lasted until 1800 UTC (1400 EST), then decreased from the maximum of 85 ppbv to 60 ppbv (Fig. 3.5b).

The diurnal variation at Beltsville includes TROPOZ O_3 lidar, EPA AirNow, and simulations of Ex1 and Ex3. Ex1 simulation underestimated the O_3 mixing ratio significantly due to the lack of fire emissions. Its maximum O_3 mixing ratio was only 25 ppbv at daytime, while the TROPOZ and AirNow maximum observed O_3 mixing ratio was 120 ppbv, which is due to its suburban location. Previous studies reported that the O_3 concentration in urban regions was elevated in the presence of the wildfire smoke (Brey et al., 2016). Dreessen et al. (2016) and Sullivan et al. (2017) reported that the O_3 concentration increased after the arrival of the Canadian wildfire smoke over the Baltimore-Washington D.C. metropolis. Brey et al. 2016 reported that the enhanced O_3 was due to the mixture of smoke particles with local NO_X emissions. After considering the FINN fire emissions, Ex3 matched the observed O_3 mixing ratio much better, but still underestimated the O_3 mixing ratio from 1500 to 1900 UTC. The Pearson correlation coefficient was 0.96, while the RMSE was 17.19 ppbv.

3.3.3.3 Vertical profile

In this section, the evolutions of aerosol and O_3 vertical profiles at Beltsville are discussed. We will focus on the model performance evaluation and its comparison with observations and the onset of the long-range transported smoke mixing-down into the PBL and influence on the local air quality.

3.3.3.3.1 Smoke vertical profile evolution

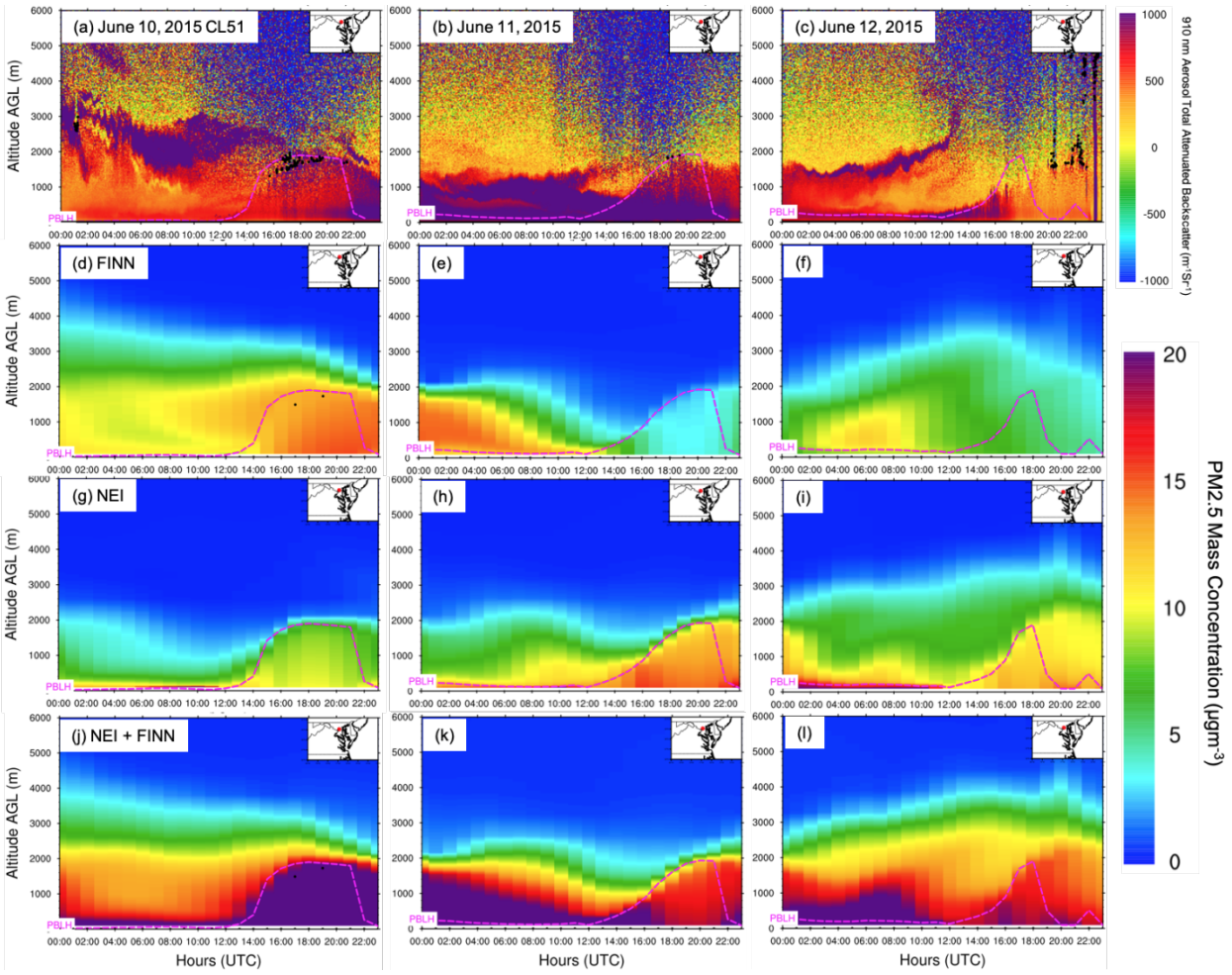

Fig. 3.6 Time series of ceilometer CL51 aerosol total attenuated backscatter at 910 nm (a-c) and WRF-Chem $PM_{2.5}$ mass concentration (d-f) on 10-12 June 2015. The pink curve is denoted as the model simulated PBLH. The upper right inserted map shows the location of the site (red dot).

The ceilometer CL51 aerosol backscatter profiles and the WRF-Chem simulated $PM_{2.5}$ mass concentrations of Ex1, Ex2, and Ex3 on 10-12 June are shown in Fig. 3.6. The plots clearly show smoke arrived on 10 June at 2-4 km and slowly descended and later mixed down into the PBL, meanwhile convective boundary layer grew, and wildfire smoke and precursors entrained into it (Fig. 3.6a and d). Eventually it was reported as increased BC concentration measurements reported by Dreessen et al. (2016). The elevated BC concentration was consistent with the growth of the PBL and merging with the smoke laden layer. The strength of the lidar backscatter was indicative of the increased particle concentration as it started to mix down to the PBL.

The model simulations did capture the large-scale structure revealed by the ceilometer observations: the continued descent and intrusion into the PBL and down to the surface. The model shows air was clean at low levels prior to 1600 UTC then smoke concentration increased in the afternoon on 10 June. The simulated PBL reached 2 km, where the smoke layer was located, supporting the idea that the convective overturning was responsible. While the general large-scale trend of the smoke layer descent and PBL growth and decay was well simulated by the model.

The descent in altitude of the smoke layer continued on 11 June (Fig. 3.6b), as would be expected following the shallow nocturnal PBL development. The smoke laden air mass remained below 1 km on 11 June. Starting 0000 UTC 12 June, a clear lifting and detachment from the surface of the smoke carrying air mass was noticed. This lifting continued through the night from 1 km to 2 km by sunrise (1200 UTC) and was associated with the arrival of the air mass from the south due to increased wind speeds discussed above. The model captured the continued PBL collapse and PBL growth on 11 June and later the arrival of the air mass and associated $PM_{2.5}$ mass concentration. It did not capture the small-scale structures, like the high aerosol

concentration indicated by the ceilometer between 1-2 km altitude throughout the night of 12 June. The simulated PBL development on 12 June did not perform well, collapsing earlier than the previous two days.

Ex2 shows that the upper boundary of the smoke particles reached 3.5 km, consistent with the ceilometer backscattering observations (Fig. 3.6d). The arrival of the smoke laden air mass on 10 June, the continued descent of the layer, and the overall pattern agreed with the observations. The nocturnal and daytime PBL development on 11 June, and the pattern of the subsequent lifting of the smoke laden air mass on 12 June were indicated in the model simulations. However, while the ceilometer data indicated a similar smoke concentration within the daytime well mixed within the PBL on 10-11 June the model indicated a much lower concentration (5 $\mu g\ m^{-3}$) on 11 June compared with 10 June.

Similar trends in the general descent of the atmosphere early on 10 June followed by lifting associated with air mass flow over the measurement location were shown by the simulations of Ex1 and Ex3. Ex1 did not show the level of concentrations that would indicate smoke particles (Fig. 3.6g, h, i). However, the model captured the surface anthropogenic pollutants below 0.2 km with concentration around 10 $\mu g\ m^{-3}$, much lower than the smoke particle concentration. On the other hand, Ex3 shows a much better performance in matching the ceilometer observations and overall particle vertical distribution, consistent with what is expected to be contributed from smoke particles added to local pollutants (Fig. 3.6j).

3.3.3.3.2 O_3 vertical profile evolution

Along with WRF-Chem simulations, the O_3 mixing ratio vertical profile analysis employs TROPOZ O_3 lidar measurements at the Beltsville station on 12 June, which was six days later after the wildfire event in Canada on 6 June. Figure 3.7a shows TROPOZ O_3 mixing ratio

measurements and the WRF-Chem simulated PBLH (pink curve in the Fig. 3.7a). No data was collected from 0900-1400 UTC and above cloud base. An enhanced O_3 layer (~1.2 km) at and prior to sunrise was corresponding to the elevated smoke layer (Fig. 3.7a). The WRF-Chem simulated O_3 mixing ratio vertical profiles at this time show an overall good agreement with the TROPOZ lidar measurement trends, including the elevated O_3 signal at 1.2 km (Fig. 3.7b).

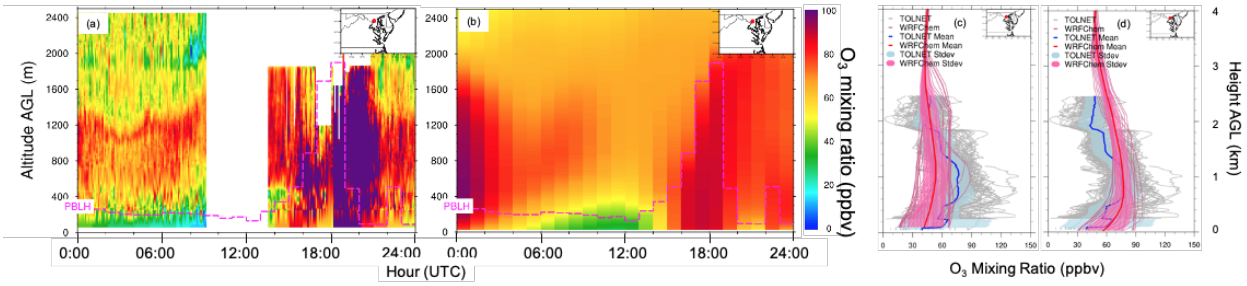

Fig. 3.7 O_3 mixing ratio vertical profiles from TROPOZ and WRF-Chem model on 12 June. (a) TROPOZ O_3 mixing ratio vertical profile time series and the WRF-Chem simulated PBLH (pink curve); (b) model O_3 mixing ratio vertical profile time series from Ex3; (c) Overall TROPOZ (blue and gray) and WRF-Chem (pink, Ex1) O_3 mixing ratio vertical profiles; (d) Overall TROPOZ (blue and gray) and WRF-Chem (pink, Ex3) O_3 mixing ratio vertical profiles. The upper right inserted map shows the location of the site (red dot).

The individual TROPOZ O_3 mixing ratio profiles and mean together with WRF-Chem simulated O_3 mixing ratio vertical profiles and mean are shown in Fig. 3.7c and d. The O_3 mixing ratio vertical profiles varied with time and altitude. The simulated O_3 mixing ratio increased from 30-40 ppbv near the surface to 70-80 ppbv at 1 km, followed by a smooth decrease to 50 ppbv at 3 km. The standard deviations of the simulated O_3 vertical profiles varied 5-10 ppbv. Similarly, the ozonesonde O_3 mixing ratio at 0800 UTC 12 June also increased gradually from 15 ppbv at the surface to 70 ppbv at 1.5 km, then decreased to 50 ppbv (Fig. 3.8). O_3 mixing ratios generally increased with altitude near the surface, mainly because of the lack of

chemical loss in the upper troposphere (water vapor and hence low HOx concentrations). The model simulated PBLHs were 0.1-0.3 km (Fig. 3.8), which confined water vapor and HOx vertical mixing. The WRF-Chem simulation profiles, although revealed a similar trend, were about 10 ppbv or less over the ozonesonde data. The largest difference was centered around 1-1.4 km, where the narrow wind sheared, aerosol/smoke enhanced, layer seen in the ceilometer data above (Fig 3.7c). The lidar data agreed with the ozonesonde values at about 0.3-0.5 km, the lowest available data points for lidar, and increased to 70 ppbv at 1 km, then decreased sharply to 20 ppbv at 2 km followed by an increase to almost 50 ppbv at 2.5 km. However, the WRF-Chem-TROPOZ agreement centered at 1-1.5 km was more than what the ozonesonde measured by about 15 ppbv. This difference could be caused by balloon drift out of the area due to the increased shear and wind speed present at the time. While the TROPOZ O_3 mixing ratio sharply decreased at 1.4-2 km, which was primarily caused by inability of O_3 lidar to probe in heavy aerosol and/or cloud layers because of the very low signal to noise ratio. Nevertheless, despite the elevated enhancement and the trend with altitude, the observed and simulated O_3 mixing ratios are fairly in agreement.

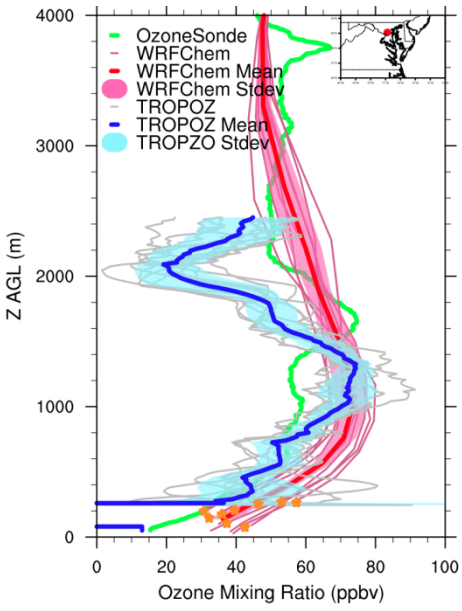

Fig. 3.8 O_3 mixing ratio vertical profiles of WRF-Chem (thin red curves, Ex3), ozonesonde (thick green curve), and TROPOZ O_3 lidar (thin grey curves) at 0800 UTC 12 June 2015. The WRF-Chem simulated O_3 mixing ratio profile mean and standard deviation are shown as a red thick curve and shade, respectively. The TROPOZ O_3 mixing ratio profile mean and standard deviation are shown as a blue thick curve and shade, respectively. The orange stars denote the WRF-Chem simulated PBLH for the corresponding O_3 mixing ratio profiles. The upper right inserted map shows the location of the Beltsville site (red dot).

3.4 Concluding Summary

This study focuses on the Canadian wildfire smoke event on 6 June 2015, and its transport pathway and influence on the local/regional air quality (O_3 and PM) in the U.S. An integrated study using WRF-Chem model simulations, ground-based observations, and satellite data identifies the source of the wildfire in Alberta and Saskatchewan provinces of Canada, its transport path through the U.S.-Canada border, its stagnation over the Ohio River Valley, and final arrival and manner of mixing to the surface over the sampling site in Beltsville, Maryland.

The key findings include characterization of the large-scale long-term smoke transport and the local air pollution impacts.

The FINN fire emission revealed significant wildfire emission was ejected into the atmosphere at 2200 UTC 6 June near south of Lake Athabasca in Saskatchewan Province, Canada. The smoke was transported and detected over North Dakota and Minnesota on 7 June and drifted further south arriving over the Ohio River Valley by 9 June. The smoke transport path changed from south heading to east and stagnated, owing to the wind direction zonal change before it crossed the Appalachian Mountain region and started to mix-down to the surface over Beltsville late on 10 June and transported out further east on 11-12 June. According to the smoke

vertical structure, the simulated smoke vertical profiles agreed well with the CALIOP VFM measurements, both of which showed the smoke plume height around 3 km at the Mid-Atlantic. Due to the block of clouds, the CALIOP did not detect the smoke continuously on 9 June. Fortunately, the model simulation reproduced the smoke vertical profile along the CALIPSO ground track.

Ground-based profile measurements of wind and O_3 were used to interrogate the model results. The wind radar profile evolution observed at Piney Run, Beltsville, and Horn Point showed the temporal wind velocity vertical variation and associated diurnal cycle. On 8-12 June, the wind direction was west above 0.5 km and wind speed reduced gradually from 20 m s^{-1} to 10 m s^{-1}. The model simulated wind direction and speed profiles generally agreed well with the wind radar observations, as well as diurnal cycle, which led to strong confidence on the validity of the WRF-Chem model simulated smoke transport. At Piney Run, the west wind speed was 10-20 m s^{-1}, due to its location over mountains. At Beltsville, the wind speed was 10-12 m s^{-1} on 10-12 June when smoke was transported to this region. The wind direction shifted from west to south and favored the smoke further transported to the Northeast. Surface measured O_3 diurnal variation showed that the general tendency of the WRF-Chem model simulated O_3 agreed with the EPA AirNow surface O_3. Three surface stations were selected for quantification and comparison of the modeled and measured impact by the aged smoke on the O_3 concentration, i.e., Hagerstown, Edgewood, and Beltsville. Hagerstown, as a rural station, was less impacted by the smoke on its O_3 concentration. Its daytime maximum was 70 ppbv which was slightly higher than the day without smoke. Edgewood, close to the Chesapeake Bay, reached the maximum O_3 mixing ratio of 85 ppbv in the day, exceeding the NAAQS O_3 standard. Beltsville had the highest O_3 peak among three stations, which reached 120 ppbv due to the aged transported smoke mixed

with the local urban pollutants. Overall, the model simulated surface O_3 diurnal variation maintained the high correlation with EPA AirNow surface O_3 observations over three stations. Their Pearson correlation coefficients were over 0.95 and RMSEs were as low as 5.0 ppbv. These results demonstrate the WRF-Chem model simulation skill and show great performance in capturing the O_3 mixing ratio diurnal variation.

Aerosol backscatter data from ceilometers revealed that transported Canadian wildfire smoke intruded into the Baltimore-Washington D.C. area from 3.5 km at 0000 UTC on 10 June. Smoke entrained to the PBL and mixed with the anthropogenic pollutants and the model experiments (Ex1 and Ex2) indicated that the smoke particle contributes about 60 % to the total particle pollution. The contribution was slightly reduced the next night (~50 %) attributed to the decreasing vigor in mixing and development of the shallow stable boundary layer. The role of the mixing and subsequent cleansing associated with a cold frontal passage was well captured and adequately simulated including the formation of an elevated shear-generated smoke layer.

The TROPOZ O_3 lidar observed O_3 vertical profiles at Beltsville from 1400 – 2400 UTC on 12 June matched the WRF-Chem simulated O_3 mixing ratio above 2 km well while the model underestimated the lidar data below 2 km. On the other hand, inclusion of anthropogenic, biogenic, and fire emissions (Ex3) in the simulation captured the O_3 mixing vertical profiles below 1.5 km well, compared with both TROPOZ O_3 lidar and ozonesonde observations.

Based on the previous study by Loughner et al., (2011), the model simulations with resolution of 1.5 km and 0.5 km resolve the boundary layer and the structure of the bay breeze better than coarser resolutions, i.e., 4.5 km and 13.5 km. The model resolution of 3 km in this study well resolved boundary layer, as well as bay breeze. Finer resolution should be better to resolve fine structures.

Finally, this study employed the state-of-the-art lidar observed O_3 vertical profiles to evaluate the mesoscale modeling simulations of an important long-range transported smoke event. Such interrogation of model and performance in the PBL is important because of its impact on air pollution and human health. It also utilized the FINN fire emission, coupled with the anthropogenic emissions and biogenic emissions, to track and reproduce the smoke transport pathway leading to altered surface measurements. Further, by conducting three different numerical experiments, the study quantified the smoke influence on local air pollution in both O_3 and PM. However, the model simulated O_3 vertical profile did not match the O_3 lidar perfectly. In order to improve model performance on simulating the O_3 vertical profile, assimilating O_3 lidar observation into the WRF-Chem model is the future study.

Chapter 4

Assimilating Ozone Lidar Profile and AirNow Surface Ozone Observations over the eastern US during a Canadian Wildfire Smoke Intrusion Event using WRF-Chem/DART

4.1 introduction

The air quality forecast is one application of the chemical weather forecasts, which rely on coupled forecast model-data assimilation systems that ingest a combination of remotely sensed and in situ atmospheric composition observations together with conventional meteorological observations (Mizzi et al., 2016). The application of data assimilation to atmospheric chemistry is more recent because numerical deterministic models of atmospheric chemistry have been used routinely for air quality forecasting only since the mid 1990s (Carmichael et al., 2008; Bocquet et al., 2015). The chemical data assimilation involves reanalysis to produce air pollutant concentration maps, inverse modeling to improve (or identify errors in) emission rates, boundary conditions, and model parameters. Even built on the meteorological data assimilation, the chemical data assimilation can be still challenging due to the interactions among meteorological and chemical variables (Bocquet et al., 2015). A large range of state space variables, such as O_3 (Elbern and Schmidt, 2001; Chai et al., 2007), nitrogen dioxide (NO2, Liu et al., 2017), carbon monoxide (CO, Mizzi et al., 2016), aerosols (particulate matter, PM), and aerosol optical thickness (AOT) had been assimilated into models (Bocquet et al., 2015).

The chemical transport models (CTM) use meteorological fields as inputs and coupled chemistry meteorology models simulate meteorology and atmospheric chemistry jointly (i.e., WRF-Chem). The AOT retrieval products from satellites and ground-based instruments are assimilated into the WRF-Chem model from the previous studies. Since AOT is not a state/analysis variable in models, the observation forward operator links AOT with the model state variables (i.e., aerosol mass concentration). A new one-step algorithm was developed to assimilate MODIS AOT by analyzing the 3-D mass concentration of 14 aerosol variables from

the Goddard Chemistry Aerosol Radiation and Transport (GOCART) model within the National Centers for Environmental Prediction (NCEP) operational Gridpoint Statistical Interpolation (GSI) 3DVAR meteorological DA system coupled to the WRF-Chem model. Both the AOT forward model and corresponding Jacobian model were developed within the Community Radiative Transfer Model (CRTM). The results of the analysis were cross validated with CALIOP and AERONET measurements (Liu et al., 2011). Similarly, the same GSI 3D-VAR with WRF-Chem system was employed to assimilate the surface PM10 observations (Jiang et al., 2013). In addition to the variational methods (3D-VAR, 4D-VAR), the sequential methods and hybrid methods were also employed to assimilate AOT and surface PM concentrations (Schwartz et al., 2014).

Apart from the particle and AOT chemical data assimilation, the gas phase chemical data assimilation is also one big aspect, i.e., O_3, NO_2. Messina et al. (2011) assimilated both O_3 and NO_2 using the Optimal Interpolation method. They employed an Observing System Simulation Experiment (OSSE) approach and showed that NO_2 data assimilation was successful in correcting errors because of NO_X emission biases. However, the NO_2 assimilation increased the O_3 bias at night due to the nocturnal O_3 and NO_2 chemical reactions.

The traditional Ensemble Kalman Filter (EnKF) assumes the error distributions of both the source prior estimates and observations are Gaussian. While chemical species values are bounded, which are equal to or greater than zero. Its error distributions may display non-Gaussian distributions. In terms of solving the non-Gaussian distributions, the following data assimilation techniques exist but still need to put more effort into their further developments. The particle filter allows no assumptions regarding error distribution for the prior model state. The particle filter provides weights to ensemble members (denoted particles), which reflect the

likelihood of observations given each member (van Leeuwen, 2009). The marginal adjustment rank histogram filter is introduced by Anderson (2020) for non-Gaussian prior distributions, non-Gaussian likelihoods, and bounded state variables.

The nonlinearities of the atmospheric chemistry data assimilation problem related to both the nonlinear reaction equations and the uncertainties in transport of the different species make the implementation more complex and the computational cost of the data assimilation more expensive (Carmichael et al., 2008). Some of the important challenges in chemical data assimilation include:

(1) memory shortage (~ 100 concentrations of various species at each grid points, check-pointing required).

(2) stiff differential equations (> 200 various chemical reactions coupled together, lifetimes of different species vary from seconds to months).

(3) chemical observations are limited, compared to meteorological data.

(4) emission inventories are often outdated, and uncertainties are not well-quantified.

(5) uncertainties resulted from the tracer transport.

4.2 Motivation

We investigated the local and remote air pollutants to the D.C.-Maryland-Virginia region. The WRF-Chem model simulations were evaluated using satellite observations (i.e., MODIS, CALIOP) and ground-based observations (i.e., AirNow, wind radar, radiosonde, ozonesonde, O_3 lidar). The model performance evaluation showed some agreement with observations (i.e., wind, surface O_3), but as well some disagreement with O_3 lidar. The disagreement is located above 1.5 km. This disagreement between model and O_3 lidar motivated us to assimilate the O_3 lidar observations into models to improve model forecast (Chapter 3). This disagreement leads us to

employ the data assimilation technique, specifically the EnKF method, to assimilate both meteorological observations and O_3 observations. To the best of our knowledge, this will be the first assimilation attempt of both meteorology and lidar O_3 data coupled together.

4.3 Model configuration, study domain, assimilation method, and datasets

4.3.1 Model configuration

The model employed in this study is WRF-Chem version 3.6, and the data assimilation method is the Ensemble Adjustment Kalman Filter (EAKF), developed by Anderson (2001, 2003).

4.3.2 Study domain

Fig. 4.1 WRF-Chem model domain setup. The mother domain includes most of Canada and continental US, in order to cover both the wildfire source region and our study region. The nested domain includes the eastern US. The fire icons indicate the wildfire source region in Canada.

Two domains are involved in the data assimilation (Fig. 4.1). The outer domain (d01) covers the wildfire source region in Canada, our study region in Continental US with coarse grid spacing, and the wildfire smoke transport path from Canada to US. The nested domain contains the smoke transport path in the US and our study region with fine grid spacing. The reason to set

the mother domain so large is because we need to include the fire emission in the simulation. In addition, the wildfire ignited by lightning on June 6, 2015 and the smoke from this wildfire event arrived at the D.C.-Maryland-Virginia area on June 10, 2020, and the O_3 pollution peak appeared on June 12, 2020 in the Washington-Baltimore metropolitan area. Furthermore, the model requires extra time to spin up. The spin-up time for one-week simulation should be beyond 24 hours. Here the spin-up time was set to initiate at 00:00 UTC June 3, 2015.

4.3.3 Data Assimilation method

4.3.3.1 Meteorological DA

The WRF Data Assimilation system (WRFDA) is a community data assimilation for WRF with the hybrid variational-ensemble algorithm (Barker et al., 2012, Fig. 4.2). The WRFDA system can ingest a wide variety of observation types, i.e., radar radial velocity and reflectivity, satellite radiance data, as well as the standard conventional observation types (surface, rawinsonde, aircraft, wind profiler, and atmospheric motion vectors).

In addition to the hybrid variational-ensemble algorithm that combines the benefits of the physically based variational approach with the statistical, flow-dependent error information provided by ensemble forecasts, a variety of alternative variational data assimilation techniques are available in WRFDA: 3DVAR and 4DVAR. The core of WRFDA is a variational minimization of a cost function designed to optimally blend observations and prior NWP forecasts (Barker et al., 2012).

Data assimilation requires accurate estimation of observation and forecast error to optimize the use of input observational and prior forecast data. The WRFDA system has a table of observation errors for each major observation type. The forecast error statistics calculated for the specific domain of interest is significant to enhance forecast performance (Barker et al., 2012).

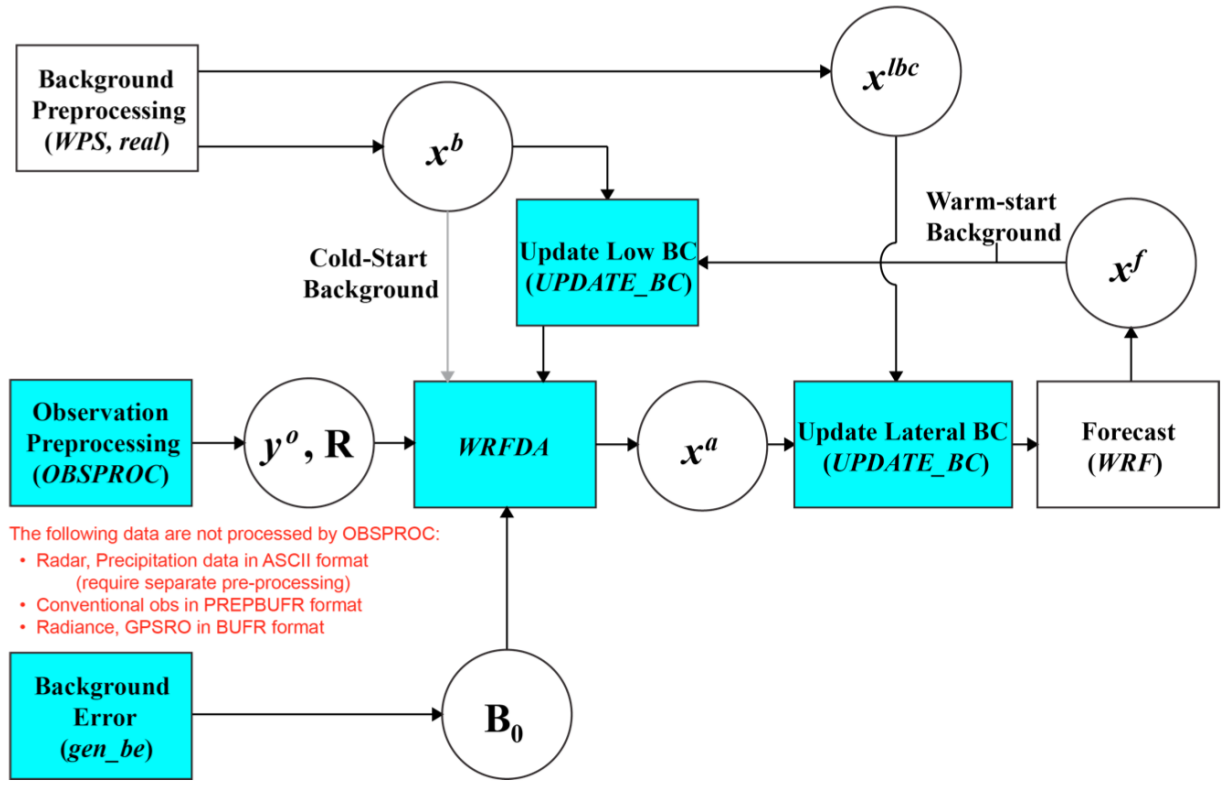

Fig 4.2 WRFDA in the WRF modeling system

x^b first guess, either from a previous WRF forecast or from WPS/real.exe output.

x^{lbc} lateral boundary from WPS/real.exe output.

x^a analysis from the WRFDA data assimilation system.

x^f WRF forecast output.

y^o observations processed by OBSPROC. (note: PREPBUFR input, radar, radiance, and rainfall data do not go through OBSPROC)

$\mathbf{B_0}$ background error statistics from generic BE data (CV3) or gen_be.

R observational and representative error statistics.

4.3.3.2 DART and WRF-Chem/DART

4.3.3.2.1 DART

DART is an open-source community facility, developed and maintained at the National Center for Atmospheric Research (NCAR), which provides well-documented software tools for data assimilation education, research, and development (Anderson et al., 2009, available at https://dart.ucar.edu/). DART includes interfaces to a number of regional and global atmospheric and oceanic models (i.e., Community Earth System Model (CESM), Community Atmosphere Model (CAM), WRF), and many low-order models (i.e., Lorenz 63 and Lorenz 96). Basic ensemble filters require only a prediction model and a forward operator to compute the expected value of an observation given a model state. DART is easy to use while importing a new model or assimilating a new observation type. DART provides the following data assimilation algorithms:

1 = EAKF (Ensemble Adjustment Kalman Filter, see Anderson, 2001)

2 = ENKF (Ensemble Kalman Filter)

3 = Kernel filter

4 = Observation Space Particle filter

5 = Random draw from posterior

6 = Deterministic draw from posterior with fixed kurtosis (ditto)

7 = Boxcar kernel filter

8 = Rank Histogram filter (see Anderson, 2010)

9 = Particle filter (see Poterjoy, 2016)

4.3.3.2.2 WRF-Chem/DART

The forecast-data assimilation system used in this study is the Weather Research and Forecasting model coupled with Chemistry package/Data Assimilation Research Testbed (WRF-Chem/DART, Mizzi et a., 2016), which consists of the following elements: the forecast model, the assimilation engine, and observations of meteorological and chemical states to be assimilated (Liu et al., 2017). The WRF-Chem model has been described in the Chapter 3, along with model configurations.

WRF-Chem/DART is the application of DART to the WRF-Chem model to assimilate chemical observations as well as meteorological observations simultaneously. The data assimilation algorithm selected in this study is the EAKF (Anderson 2001; 2003). This study implements the TROPOZ lidar O_3 vertical profile observations into the WRF-Chem/DART system. Incorporating TROPOZ lidar observations into WRF-Chem/DART only requires creating a forward operator that computes the expected value of O_3, a model state variable.

4.3.3.2.3 Inflation

DART has two choices of the basic types of inflation: observation-space and state-space. The state-space inflation changes the spread of an ensemble without changing the ensemble mean. Both the ensemble mean and standard deviation are calculated for each variable in the state vector. Then the member's values are moved away from the mean in such a way that the mean remains unchanged. The resulting standard deviation is larger than before. It can be applied to the prior state, before observations are assimilated, or it can be applied to the posterior state, after assimilation (Anderson 2007; 2009). Recent study suggests that prior and posterior inflation can be used to address different issues in the filtering problem (El Gharamti et al., 2019). Prior inflation

is able to address issues in the forecast step, such as model errors, while posterior inflation can help mitigate sampling errors in the analysis step.

4.3.3.2.4 localization

DART provides three different localization functions, i.e., Gaspasi-Cohn, Boxcar, and Ramped Boxcar (Fig. 4.3). These functions control the shape of the multiplier function applied to the computed increment as the distance increases between the observation and the state vector item. The Gaspari-Cohn function has a value of 0 at twice the cutoff and 1 at 0 distance and decreases in an approximation of a Gaussian function in between. The Boxcar is 1 from 0 to twice of the cutoff and then 0 beyond the cutoff. The Ramped Boxcar is 1 at the cutoff and then ramps linearly down to zero at the twice of the cutoff.

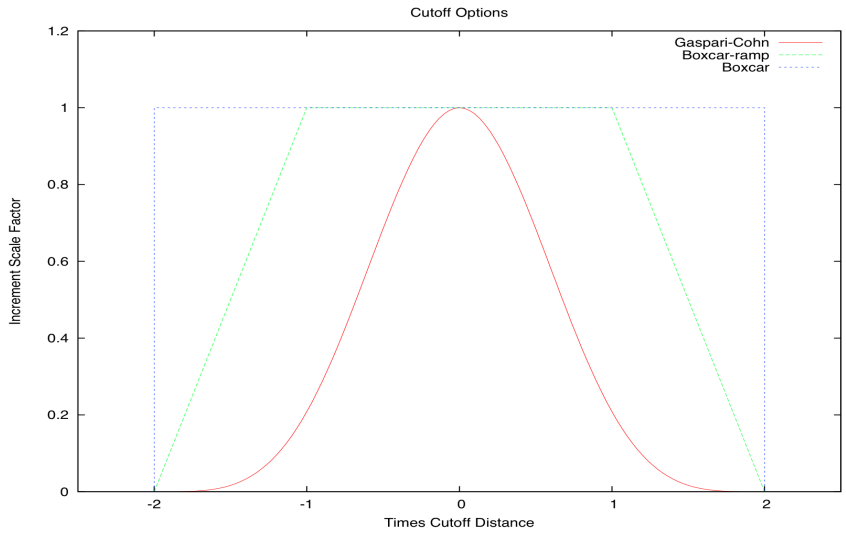

Fig. 4.3 Localization types in DART, Gaspasi-Cohn (red solid line), boxcar-ramp (green dashed line), and boxcar (blue dashed line).

In the chemical data assimilation, another localization is called variable localization, introduced by Arellano Jr. et al., (2007). It reduces spurious correlations among observations and different types of state variables. For instance, the O_3 influences other chemical species and also

meteorological state variables i.e., surface pressure, temperature, horizontal velocity, specific humidity, cloud. However, in this work, these influences are ignored.

4.3.3.2.5 TROPOZ O_3 lidar observation forward operator

TROPOZ O_3 lidar retrieved products include O_3 mixing ratio, which is a model state variable. It means that the observed variable and the model state variable are the same. Its observation forward operator is designed only to interpolate the horizontal and vertical location of the model state variable to the horizontal and vertical location of the observed variable (O_3 mixing ratio). The horizontal interpolation is relatively easy to achieve. The modeled O_3 mixing ratio at the model horizontal grid is interpolated to the observation location. While the vertical interpolation is complicated, since TROPOZ vertical coordinate is in height while the WRF-Chem model vertical coordinate is in eta level. It is necessary to transform eta level to height. Geopotential is included at each level, which can be used to calculate the relation between eta levels and height by using the equation below (Hobbs and Wallace, 2006).

$$H = \frac{\Phi R_e}{gR_e - \Phi} - H_{terrain} \tag{4.1}$$

H is the height above ground level. Φ is the geopotential. g is the gravitational constant. R_e is average Earth radius. $H_{terrain}$ is the terrain height. The TROPOZ O_3 lidar observation forward operator also takes the observation errors into account. TROPOZ O_3 lidar products provide O_3 mixing ratio uncertainty, which sets the initial criteria to accept or reject observations for data assimilation.

4.3.4 Datasets

4.3.4.1 Model input datasets

Dataset	Name	Note
Meteorological ICs/BCs	GFS	Global Forecast System
Chemical ICs/BCs	MOZART-4	Model for OZone And Related chemical Tracers
Anthropogenic Emission	NEI 2011	National Emission Inventory 2011 (Point, area, mobile)
Biogenic Emission	MEGAN	Model of Emissions of Gases and Aerosols from Nature
Smoke Emission	FINN	Fire INventory from NCAR (Open biomass burning, daily, 1 km resolution, global, trace gases and particle)

Table 4.1 Meteorological and chemical emission data sets. ICs: Initial Conditions, BCs: Boundary Conditions.

The model meteorological initial condition (ICs) and boundary condition (BCs), chemical ICs/BCs, and emission date sets are shown in Table 4.1. The Global Forecast System (GFS) provides meteorological ICs/BCs for WRF, with resolution of 0.25-degree grids which include analysis and forecast time steps at a 3-hourly interval from 00Z to 24Z. The GFS model forecast runs occur at 00Z, 06Z, 12Z, and 18Z daily. The GFS data is available at https://rda.ucar.edu/datasets/ds084.1/. In fact, the NCEP North American Regional Reanalysis (NARR) dataset was also employed as IC and BC to test the difference between NARR and GFS (not shown here). The NARR products are on the Eta 221 grid at 29 pressure levels. They were produced using the Eta 32 km model with 45 vertical layers. The input data includes all observations used in NCEP/NCAR Global Reanalysis project, and additional precipitation data, TOVS 1B radiances, profiler data, land surface and moisture data, etc. The output analyses are 3-hourly with additional 9 variables in the 3-hour forecasts to reflect accumulations or averages. The NARR data is available at https://rda.ucar.edu/datasets/ds608.0/index.html. The chemical ICs/BCs

are from the Model for OZone And Related chemical Tracers version 4 (MOZART-4), which is driven by meteorological fields from the NASA GEOS-5 model. It uses anthropogenic emissions based on Arctic Research of the Composition of the Troposphere from Aircraft and Satellites (ARCTAS) and fire emissions from FINN-v1 (Wiedinmyer et al., 2011). Its spatial resolution is 1.9 deg (latitude) by 2.5 deg (longitude) and temporal resolution is 00Z, 06Z, 12Z, and 18Z. The MOZART-4 chemical data is available at https://www.acom.ucar.edu/wrf-chem/mozart.shtml. The anthropogenic emission is from National Emission Inventory 2011, which includes point, area, and mobile emissions. The Model of Emissions of Gases and Aerosols from Nature (MEGAN) is employed as the biogenic emission (Guenther et al., 2006). The fire emission is the Fire INventory from NCAR (FINN). It includes trace gases and particle emissions from open biomass burning globally. And its spatial and temporal resolution are 1 km and hourly, respectively (Wiedinmyer et al., 2011).

4.3.4.2 Assimilated observations

Observations	platform	measured parameters	Resolution (temporal)	Time available
NCEP ADP Global Upper Air and Surface Weather Observations	aircraft	horizontal wind, temperature	hourly to 12 hours	1997-2021
	radiosonde	horizontal wind, specific humidity, temperature		
	satellite (GOES)	horizontal wind		
AirNow	ground	surface O_3	hourly	1980-2021
TROPOZ	ground	O_3 profile	6 min	June 10-12, 2015

Table 4.2 The assimilated observations into WRF-Chem/DART.

In the data assimilation framework, it is necessary to account for the observational errors, including both measurement errors and representative errors. For simplicity, DART has combined measurement errors and representative errors and specifies as an observational error.

4.3.4.2.1 Meteorological observations

The PREPBUFR dataset has not been completely assimilated into the DART. The current assimilated observations from various platforms are radiosonde (horizontal wind, temperature, specific humidity, altimeter), aircraft (horizontal wind, temperature), marine surface (horizontal wind, temperature, specific humidity, altimeter), and land surface (horizontal wind, temperature, specific humidity, altimeter), satellite (horizontal wind) (Table 4.2). The PREPBUFR observations also provide errors or uncertainties in the dataset, which were used in the DART during the data assimilation. For example, the radiosonde temperature errors are 1.2 K at 1000 hPa, 0.8 K at 100 hPa, and 1.5 K at 10 hPa. The PREPBUFR dataset is available at https://rda.ucar.edu/datasets/ds337.0/index.html.

4.3.4.2.2 EPA AirNow

The AirNow program provides the observations of criteria gases (O_3, SO_2, CO, and NO_2), particulates (PM_{10}, $PM_{2.5}$), meteorological (winds, temperature, barometric pressure, relative humidity, and dew point), toxics, ozone precursors, lead, and blanks (blanks are empty cannisters that are measured for speciation quality assurance reasons). The following seven types of files are available: site descriptions, monitor descriptions, annual summary data, daily and daily summary data, hourly data, 8-hour average data, and blanks data (Table 4.2). These data sets are available for downloading at https://aqs.epa.gov/aqsweb/airdata/download_files.html#Raw. In this study, we employed the hourly O_3 data to be assimilated into WRF-Chem/DART. The observational

errors of AirNow surface O_3 are made an educated guess as 20 % of its measurement, neglecting the diurnal variations.

4.3.4.2.3 TROPOZ O_3

Details of TROPOZ O_3 lidar are seen in the section 3.2.2. The retrieval yields an uncertainty of 16–19 % from 0 to 1.5 km, 10–18 % from 1.5 to 3 km, and 11–25 % from 3 to 12 km according to the relevant aerosol concentration aloft (Sullivan et al., 2014). The specific uncertainties are included in the TROPOZ O_3 vertical profile products. The time interval of the vertical profiles every six min. The assimilation window is hourly. In the WRF-Chem/DART assimilation, all the profiles within the assimilation window are included.

4.3.4.3 Experiment design

Experiment	Met/Chem DA		Purpose
Spin-up: June/03-05 Fire: June/06-07 MD: June/10-12	Domain 01 (d01, 27 km)	Domain 02 (d02, 9 km)	d01: fire emission source. d02: smoke influence (Great Lakes, OH, MD)
Baseline	Y/N	N/N	Performance only with Meteorological DA i)Surface met (U-wind)
Control 1	Y/Y(A*)	N/N	Performance with AirNow DA i)Surface Distribution (O_3) ii)Evolution (O_3)
Control 2	Y/Y(T**)	N/N	Performance with TROPOZ DA i)Profile (O_3)
Control 3	Y/Y(AT)	N/N	Performance with both AirNow & TROPOZ DA

Table 4.3 WRF-Chem/DART designed experiments. N: without DA; Y: with DA, *: AirNow; T: TROPOZ.

In order to test the DA performance on assimilating different meteorological and chemical observations, four experiments were conducted with different observations assimilated (Table 4.3). First is the baseline to only assimilate meteorological observations, which is designed to test the how well the model improves after assimilating meteorological observations. Second is the control 1 experiment to assimilate meteorological observations and AirNow O_3, to see the assimilation performance while assimilating both meteorological data and surface O_3 observations. Third is the control 2 experiment to assimilate meteorological observations and TROPOZ O_3, to track the influence of assimilating both meteorological data and TROPOZ O_3 vertical profile. And the last is the control 4 experiment to assimilate meteorological observations, AirNow O_3 and TROPOZ O_3, to evaluate the performance of the best assimilation we could conduct.

4.4 Data assimilation results diagnosis

4.4.1 Diagnostic methods

4.4.1.1 Qualitative diagnostic methods

The observation data quality is significant for the assimilation performance. Each observation has a prior quality control value. In addition, a DART quality control value is added when observation sequences are generated by DART programs. One criterion to control whether the DART filter assimilates an observation is the outlier threshold which is designed to discard observations that are inconsistent with prior. It is defined as the N times of total spread (standard deviations from the square root of the sum of the prior ensemble and observation error variance) and can be specified in the DART namelist. If the difference between the observation and the prior ensemble mean is more than N times of total spread, the observation will be rejected. Outlier threshold can be used to avoid bad observations (ones where the value was recorded in error, or the processing has an error and a non-physical value was generated). It also avoids

observations which have accurate values, but the mean of the ensemble members is so far from the observation value that assimilating it would result in unacceptably large increments that might destabilize the model run.

Reject if (prior mean - observation) > N times total spread

Another qualitative diagnostic method is the DART quality control table, which is an important piece of information. Nine quality control values are defined in DART to distinguish whether observations are assimilated and why their assimilations fail.

0 and 1 indicate both Prior and Posterior are good.

0 Assimilated O.K.

1 Evaluated O.K., not assimilated because namelist specified evaluate only.

2 and 3 show Prior is ok, but Posterior failed.

2 Assimilated O.K. BUT posterior forward operator failed.

3 Evaluated O.K. BUT posterior forward operator failed.

0 and 2 mean that observation is assimilated. 1 and 3 mean Prior observation ensemble is computed, but not assimilated. This is withholding an observation to be used for validation. 2 and 3 mean that one or more posterior forward operators failed. DART cannot use this observation for posterior diagnostics, but it can be used for prior diagnostics.

4 or higher mean that both Prior and Posterior have failed

4 Prior forward operator failed.

5 Not used because of namelist control.

6 Rejected because of incoming data QC higher than namelist control.

7 Rejected because of the outlier threshold test.

8 and above reserved for future use.

5 indicates observation is not used at all, either prior or posterior diagnostics.

4.4.1.2 Quantitative diagnostic methods

The following quantities are normally diagnosed quantitatively, i.e., the number of total observations and the number of observations successfully assimilated for each assimilation window and whole assimilation period, the root mean square error of the ensemble (RMSE), the bias of the ensemble (forecast-observation), the spread of ensemble members, the pooled spread of the observation (knowing its observational error), the total spread of ensemble members and observations, the bias between ensemble and observations.

RMSE is the standard deviation of the residuals (prediction errors) between model and observations, which measures the difference between model prediction and observations. The RMSE mean is the average of RMSE of different ensemble members and observations. The RMSE is calculated by the following equation.

$$RMSE = \sqrt{\frac{\sum_{i=1}^{N} (x_i - y_i)^2}{N}} \tag{4.2}$$

Here x_i is the model state variable. y_i is the observation corresponding to the model state variables. N is the number of observations.

Bias is the difference between the expected value and observation. It is defined as

$$Bias = \frac{\sum_{i=1}^{N} (x_i - y_i)}{N} \tag{4.3}$$

Model spread is the standard deviation of the ensemble members. It is defined as

$$Spread = \frac{\sqrt{\sum_{j=1}^{M} (x_j - \mu)^2}}{M} \tag{4.4}$$

Here μ is the ensemble mean of the model state variable x_i. M is the number of the model state variables.

Total spread is the standard deviations from the square root of the sum of the prior ensemble and observation error variance.

$$Total\ spread = \sqrt{\sigma_{prior}^2 + \sigma_{obs}^2} \tag{4.5}$$

The diagnostic techniques employed to evaluate the data assimilation performance are temporal evolution and vertical profile of these quantities, and rank histogram.

4.4.1.2.1 Time evolution

The evolution contains the temporal evolution of the above-mentioned diagnostic quantities for any specified model levels, along with the number of observations possible and assimilated. The evolution of these diagnostic quantities tracks the assimilation performance from the beginning (first assimilation window) of the first observation assimilated to the end of the assimilation after all the observations are assimilated. For instance, it can show the time evolution of prior and posterior ensemble means, spread, and total spread at every assimilation window, along with the number of assimilated observations and possible observations. It also has the statistics of prior and posterior means through the whole assimilation.

4.4.1.2.2 Vertical profile

The vertical profile shows the diagnostic variables as functions of height (pressure), along with the number of observations possible and assimilated. It includes the vertical profiles of the prior and posterior diagnostic quantities, by comparing them to evaluate the assimilation performance and its variation along the vertical levels.

4.4.1.2.3 Rank histogram

Rank histogram, also called Talagrand diagram, tests the ensemble quality. It shows the rank (ordered ensemble members) as a function of the analyzed values occurrence (Fig. 4.4).

Rank histograms are repeatedly tallying the rank of the observation relative to values from an ensemble sorted from lowest to highest (Hamill, 2001). The different shapes of rank histograms distinguish the qualities of the ensemble. Interpretation of different shapes of rank histograms. (a) Flat: Observation is indistinguishable from any other member of the ensemble. Ensemble is "reliable". Ensemble spread is about right to represent forecast uncertainty; (b) U-shaped: The ensemble spread is too small. Many observations fall outside the extremes of the ensemble. Or the analyzed value falls outside the range of value sampled by the ensemble. The first and the last bin will be overpopulated; (c) Dome-shaped: The ensemble spread is too large. Most observations fall near the center of the ensemble. The analyzed value never falls outside the range of the sampled values. The first and the last bin will contain very few analyzed values; (d) Asymmetric: ensemble contains bias, which fall to one side (Hamill, 2001).

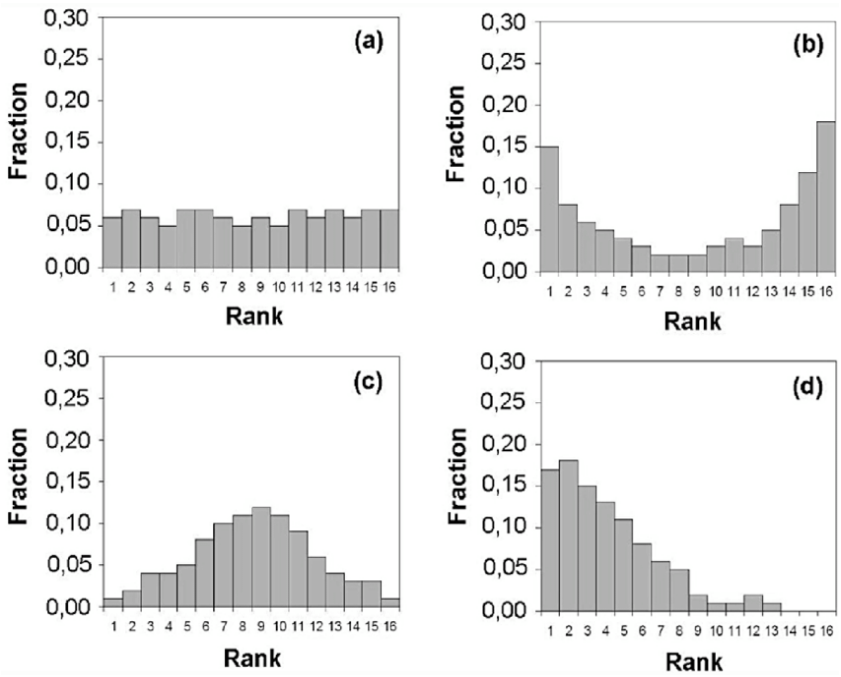

Fig. 4.4 Different shapes of rank histogram. The x axis is the rank (ordered ensemble members), and the y axis is the analyzed values occurrence fraction. (a). Flat. (b). U-shaped. (c). Dome-shaped. (d). Asymmetric.

4.4.2 Meteorological data assimilation

The meteorological observation data used for assimilation include operationally available PrepBUFR global observations from the NCEP Atmospheric Data Project (ADP) archives.

The NCEP ADP Global Upper Air and Surface Weather Observations comprise different types of quality-screened data (filtering of observations based on the error limit as well as background and duplication), i.e., surface, ship, buoys, upper air, Atmospheric Motion Vectors (AMV), scatterometer winds, etc. It contains land surface (SYNOP, METAR), marine surface (buoy, ships), radiosonde, pilot-balloon, and aircraft reports from the Global Telecommunications System (GTS), AMV from geostationary satellites, profiler- and radar-derived winds, Special Sensor Microwave Imager (SSM/I) oceanic winds and satellite wind data from National Environmental Satellite, Data, and Information Service (NESDIS) which are operationally collected by the NCEP (Greeshma et al., 2015). The temporal resolution of PrepBUFR is 6 hours, with time windows of 00Z, 06Z, 12Z, and 18Z of each day. Details about the data are available at the University Corporation for Atmospheric Research (UCAR) data server for registered users (http://rda.ucar.edu/datasets/ds337.0). In the WRF-Chem/DART, the PrepBUFR data is processed to output surface pressure, dry temperature, specific humidity, and wind components (U/V) of conventional radiosonde, aircraft reports, and satellite cloud motion derived wind. BUFR quality control values larger than 3 means observation is suspect. Most people assimilating observations from BUFR use an outlier threshold of 3.

4.4.2.1 Radiosonde

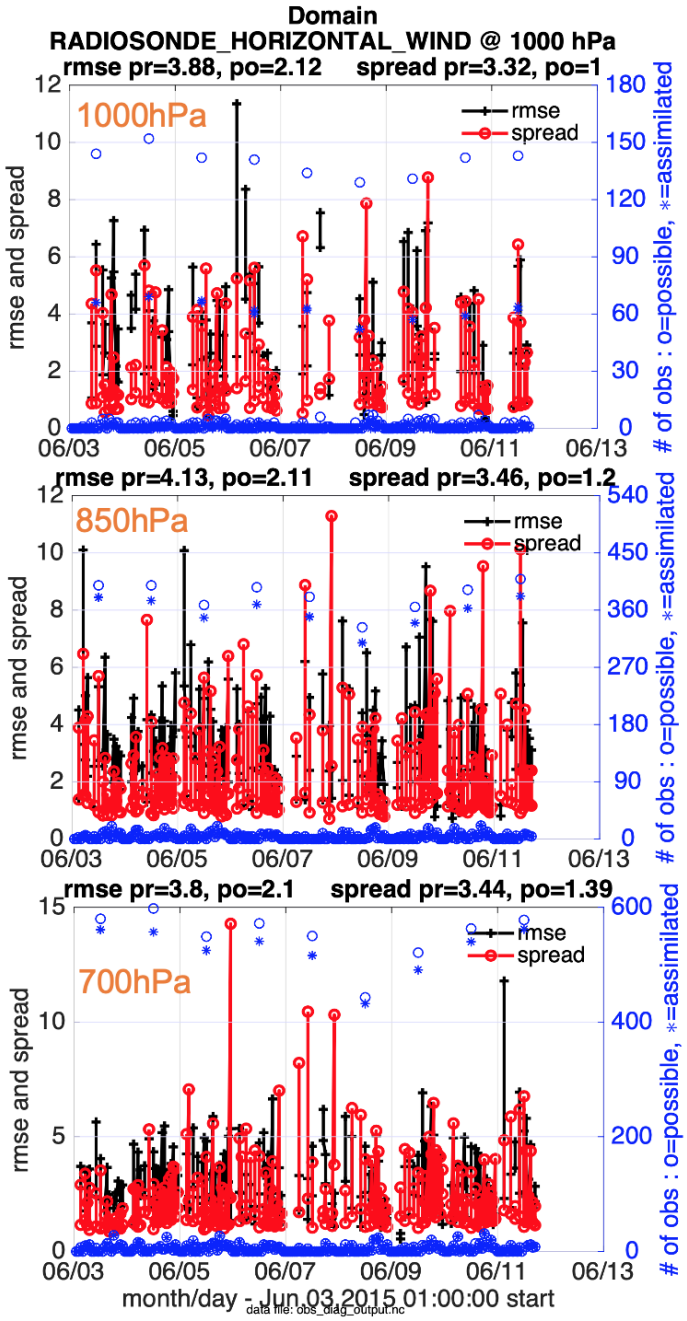

Fig. 4.5 Time series of radiosonde horizontal wind RMSE and model spread at three model levels (1000 hPa, 850 hPa, and 700 hPa) assimilated from WRF-Chem/DART. The left y axis is RMSE (black line) and model spread (red line), and the right y axis is the number of observations

including the total number of observations (denoted as “o”) and the number of assimilated observations (denoted as “*”).

The number of possible radiosonde horizontal wind observations is around 150 at 1000 hPa (Fig. 4.5). However, only 50-60 (50 %) observations are assimilated due to large radiosonde observation errors near the surface. The number of possible observations increases to 300-400 at 850 hPa and 400-600 at 700 hPa. Meanwhile, the assimilated observations increase to 90 %, because radiosonde data becomes more reliable.

Fig. 4.5 shows the time evolution of radiosonde horizontal wind RMSE and model spread for both prior (pr) and posterior (po) of radiosonde horizontal wind assimilation at three model levels 1000 hPa, 850 hPa, and 700 hPa. The assimilation time is from 0000 UTC June 3, 2015 to 0000 UTC, June 12, 2015. The black upper and lower crosses are the prior and posterior RMSEs, respectively. The red upper and lower circles are the prior and posterior model spread, respectively.

The prior and posterior RMSE means at 1000 hPa are 3.88 m s^{-1} and 2.12 m s^{-1}, respectively. The smaller posterior RMSE mean indicates that WRF-Chem/DART reduces the difference between model simulation and observations, which means that model simulation agrees more and more with observations. The prior and posterior model spread means are 3.32 m s^{-1} and 1.0 m s^{-1}, respectively. It shows more agreement among ensemble members after WRF-Chem/DART assimilation. After assimilating the radiosonde horizontal wind, the ensemble member forecasts have smaller standard deviation. Similarly, the prior and posterior RMSE means at 850 hPa are 4.13 m s^{-1} and 2.11 m s^{-1}, respectively. The prior and posterior RMSE means at 700 hPa are 3.8 m s^{-1} and 2.1 m s^{-1}, respectively. The posterior RMSE means at these three model levels have reduced by 40 -50 %, relative to the prior RMSE means.

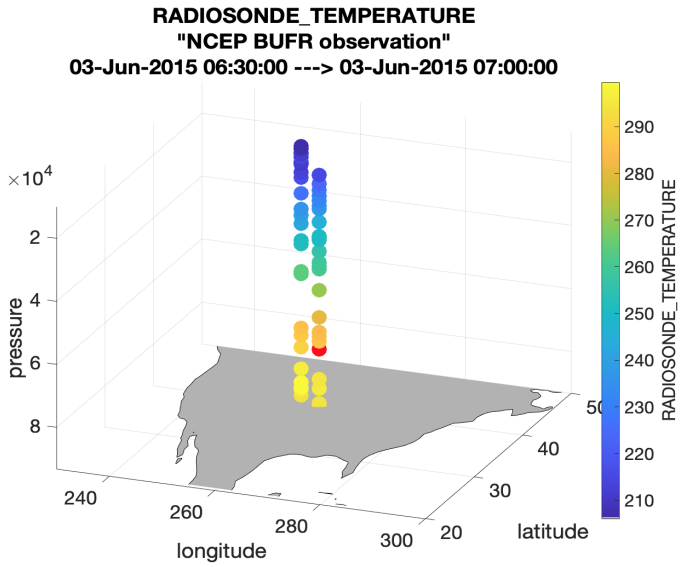

Fig. 4.6 3D color-coded scatter plot of radiosonde temperature vertical profile located in the mid-western U.S. and within assimilation window 0600-0700 UTC, June 03, 2015. Temperature unit is K. The red dot is selected to diagnose its assimilation performance, corresponding to the red dots in the Fig. 4.8 and Fig. 4.9 below.

Figure 4.6 shows the radiosonde temperature vertical profile located in the mid-western U.S. The temperature decreases from the surface to high levels. One observation value is selected to diagnose the assimilation performance at this point (the red dot). The red dots in figures 4.6, 4.7, and 4.8 are connected. If one red dot is selected in Fig. 4.6, Figures 4.7 and 4.8 will also display the selected observation in all the panels (also indicated by red dots).

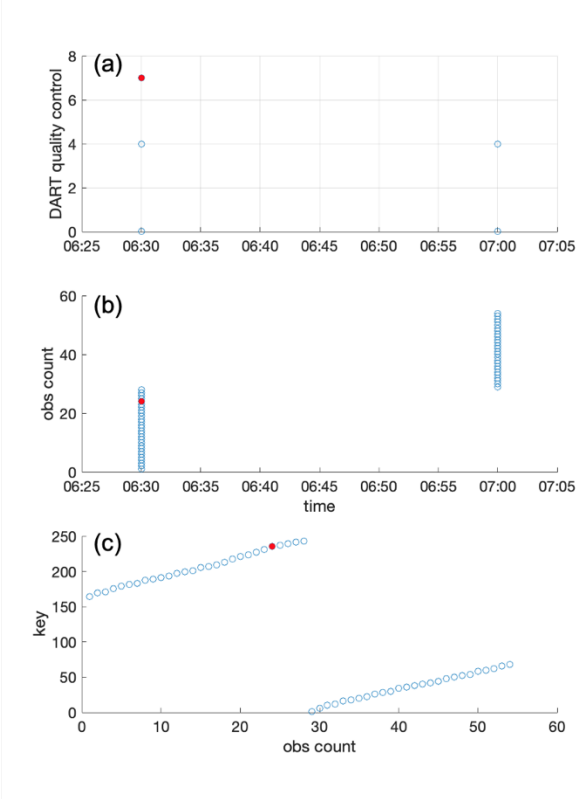

Fig. 4.7 (a) Radiosonde temperature DART quality control at 0630 and 0700 UTC. (b). The observation count at 0630 and 0700 UTC. (c). The key (sequence number) of radiosonde temperature as a function of observation count. The red dots are the observation corresponding to the red dots in the Fig. 4.6 (above) and Fig. 4.8 (below).

Fig. 4.7a shows the radiosonde temperature DART quality control flags, as shown in section 4.4.1.1. The radiosonde temperature at 0630 has three DART quality control flags, 0 (Assimilated O.K.), 4 (Prior forward operator failed), and 7 (Rejected because of outlier threshold test). The selected observation has the DART quality control flag 7, which means this observation was rejected because it's far away from the ensemble mean. The outlier threshold is set to three times of the ensemble mean in this experiment, which is a typical setting. Fig. 4.7b shows the observation counts at 0630 and 0700, which show the number of observations. The observation

count is counted continuously from the previous observation. So the observation count at 0700 starts from 29. Fig. 4.7c shows similar observation sequence count.

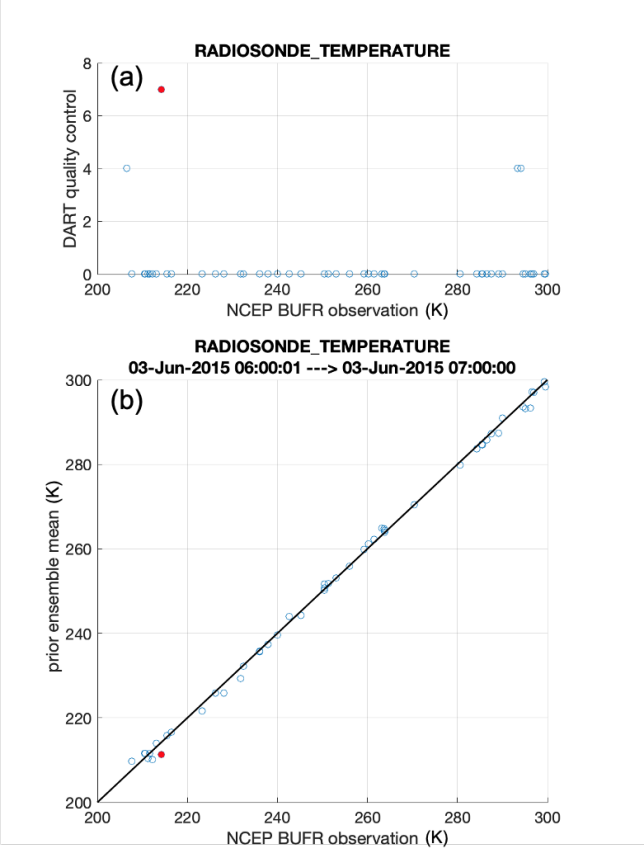

Fig. 4.8 (a) The DART quality control flags of NCEP BUFR observation. (b) The correlation of radiosonde temperature from NCEP BUFR observation and prior ensemble mean.

Fig. 4.8a shows the DART quality control for all the observations at 0630 and 0700. Most observations have the DART quality control flag of 0, which means most observations are accepted by WRF-Chem/DART and assimilated successfully. However, the radiosonde temperature observations also have the DART quality control flags of 4 (three observations) and 7 (one observation), which are rejected by WRF-Chem/DART. The correlation between radiosonde temperature observation and prior ensemble mean is good (Fig. 4.8b), which indicates that the prior ensemble mean agrees with the observation very well.

4.4.2.3 Aircraft

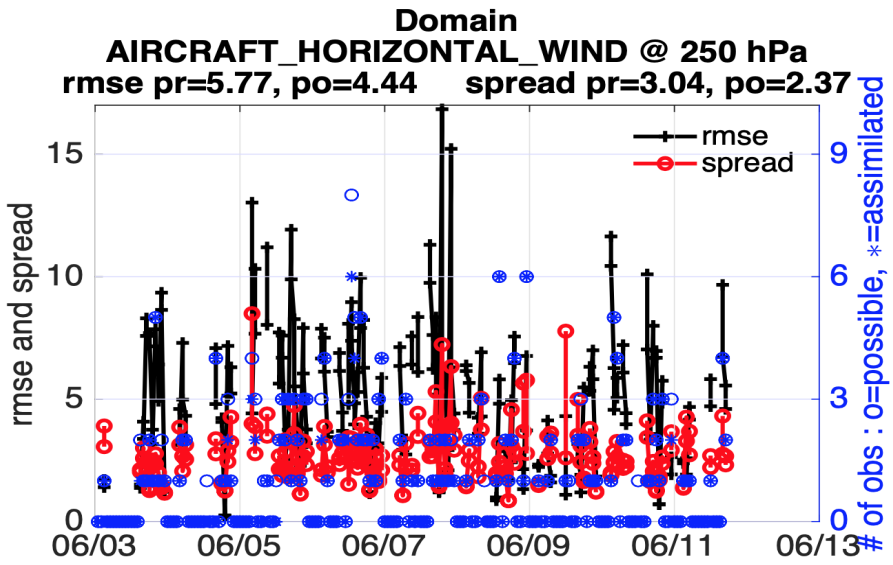

Fig. 4.9 Time series of radiosonde horizontal wind RMSE and model spread at 250 hPa assimilated from WRF-Chem/DART. The left y axis is RMSE (black) and model spread (red), and the right y axis is the number of observations including the total number of observations (denoted as "o") and the number of assimilated observations (denoted as "*").

The time series of radiosonde horizontal wind RMSE and model spread at 250 hPa are shown in Fig. 4.9. Since aircrafts measure high level wind and temperature, its data is used to assimilate upper-level atmosphere. The prior RMSE mean is 5.77 m s^{-1}. After assimilation, the posterior RMSE mean reduces to 4.44 m s^{-1}, decreases by 30 %. The prior model spread is 3.04 m s^{-1}, and posterior model spread reduces to 2.37 m s^{-1}, decreases by 22 %. Through the whole assimilation process, the number of assimilated observations is almost the same as possible observations, which means most observations are assimilated.

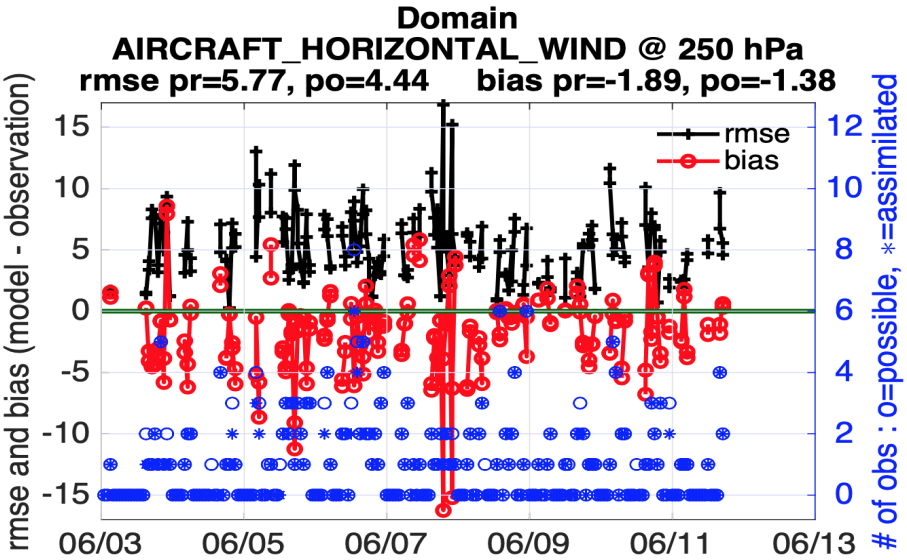

Fig. 4.10 Time series of radiosonde horizontal wind RMSE and bias at 250 hPa assimilated from WRF-Chem/DART. The left y axis is RMSE (black) and bias (red), and the right y axis is the number of observations including the total number of observations (denoted as "o") and the number of assimilated observations (denoted as "*").

Like Fig. 4.9, instead of the model spread, Fig. 4.10 shows that the prior bias is -1.89 m s^{-1}, and the posterior bias is -1.38 m s^{-1}, reduces by 32 %.

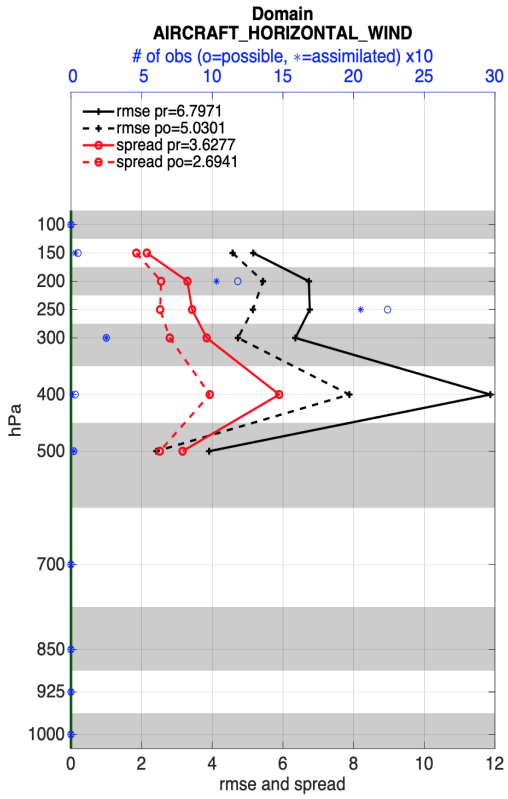

Fig. 4.11 RMSE and model spread vertical profiles of aircraft horizontal wind, and the number of possible and assimilated observations at vertical levels. The prior RMSE is the black solid line and the posterior RMSE is the black dashed line. The prior model spread is the red solid line and the posterior model spread is the red dashed line. The total number of observations is denoted as "o" and the number of assimilated observations is denoted as "*".

The vertical profiles of RMSE and model spread of aircraft horizontal wind are shown in Fig. 4.11. The posterior RMSE and model spread decrease, comparing with the prior. The RMSE and model spread show the largest reduction at 400 hPa, even though only few observations were successfully assimilated. The prior RMSE mean is 6.8 m s^{-1} and posterior RMSE mean reduces to 5.03 m s^{-1}, decreases by 26 %. Meanwhile, the prior model spread is 3.63 m s^{-1}, and posterior model spread mean is 2.69 m s^{-1}, reduced by 26 % as well.

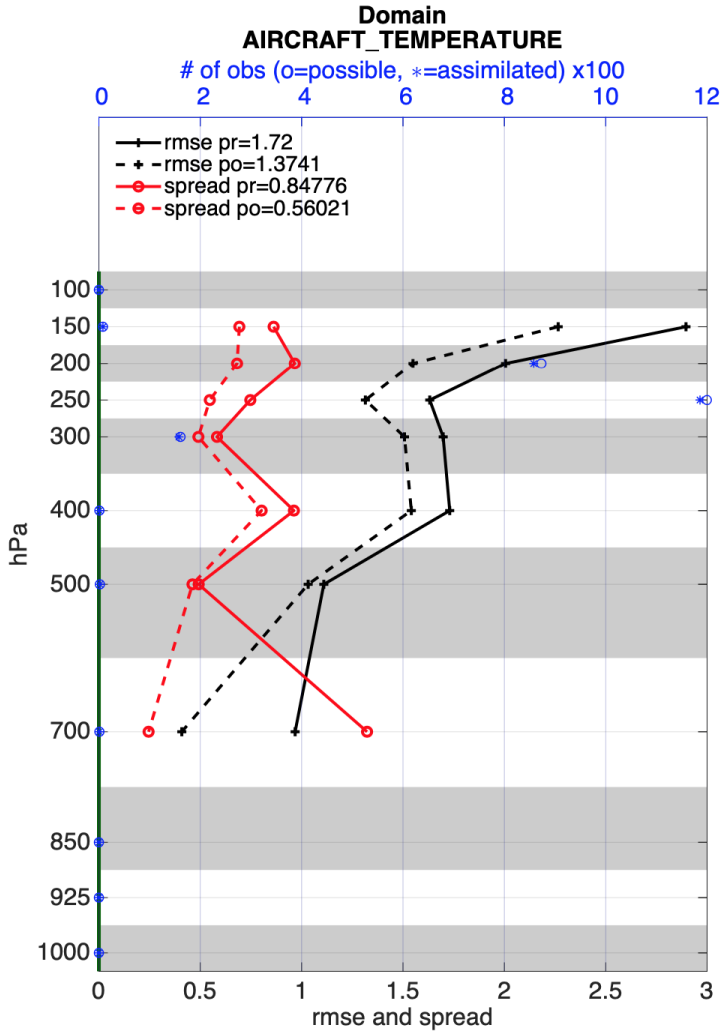

Fig. 4.12 RMSE and model spread vertical profile of aircraft temperature, and number of possible observations and assimilated observations at vertical levels. The prior RMSE is the black solid line and the posterior RMSE is the black dashed line. The prior model spread is the red solid line, and the posterior model spread is the red dashed line. The total number of observations is denoted as "o" and the number of assimilated observations is denoted as "*".

Fig. 4.12 shows the RMSE and model spread vertical profile of aircraft temperature, and the number of possible and assimilated observations. The largest number of possible observations reaches 1200 at 250 hPa. So the most effective assimilation of aircraft temperature

appears at this level since a lot of observations are assimilated. The prior and posterior RMSEs are 1.72 K and 1.37 K, respectively. The prior and posterior model spreads are 0.85 K and 0.56 K, respectively.

4.4.3 AirNow surface O_3 assimilation

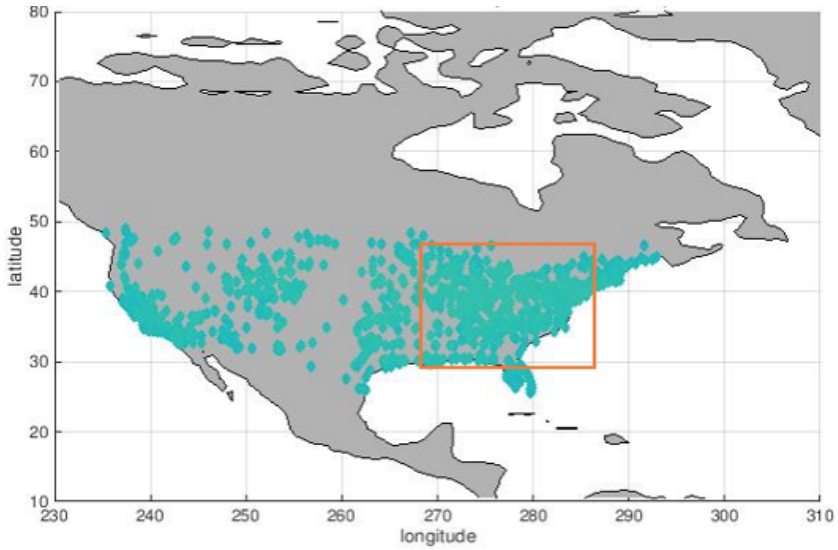

Fig. 4.13 Location of EPA AirNow stations over the Contiguous U.S.

Both observation locations and data quality influence the data assimilation performance. Fig. 4.13 shows the EPA AirNow station locations over the Contiguous U.S. There are over 1000 AirNow stations which are not uniformly distributed. More stations are located over the eastern and western U.S., while the midwestern states have less stations. The nonuniform spatial distribution of AirNow stations and availability of surface O_3 observations contributes to the quality of surface O_3 data assimilation. If more observations are available, it is possible to assimilate more observations into the model. The number of assimilated observations is larger. In this case, the performance of data assimilation is much better. Otherwise, if less observations are available, the number of assimilated observations is also smaller. The data assimilation performance is not good, i.e., the Midwest, since the AirNow monitoring stations are sparse over the Midwest (Fig. 4.13). Another influence on data assimilation performance is the data quality flag or uncertainty. The

data quality of surface O_3 observations at different stations is different. For example, certain stations have continuous and high-quality data, while others have very sparse observations. The AirNow does not have observation error/uncertainty available in the data set. Based on the previous studies, the reasonable observation error for AirNow surface O_3 measurements is about 25 % of the measured value.

The increment is defined as the difference between after (posterior) and before (prior) assimilation. Fig. 4.14 shows the increment of surface O_3 mixing ratio between prior and posterior at 0000 UTC, June 3 2015. It shows the influence of AirNow surface O_3 observations after being assimilated into the model. The positive O_3 mixing ratio increment means the observed surface O_3 mixing ratio is higher than the simulated one. The simulation overestimates the surface O_3 mixing ratio compared with AirNow surface O_3 observations. On the contrary, the negative O_3 mixing ratio increment means observation decreases the prior after assimilation. In Fig. 4.14, positive O_3 mixing ratio increments are located north of Lake Ontario, east of Mid-Atlantic, Virginia, North Carolina, South Carolina, Washington. The prior O_3 mixing ratio is underestimated over these regions. After assimilation of the AirNow surface O_3 mixing ratio, the posterior O_3 mixing ratio increased. While negative O_3 mixing ratio increments appear at Pennsylvania, Texas, Colorado, California, and northwest of Washington. Over these regions, the prior O_3 mixing ratio is overestimated. After assimilating the AirNow surface O_3 mixing ratio, the posterior O_3 mixing ratio decreased. Overall, regions with negative O_3 mixing ratio increments are larger than the positive O_3 mixing ratio regions, which indicates the overall overestimation of surface O_3 mixing ratio.

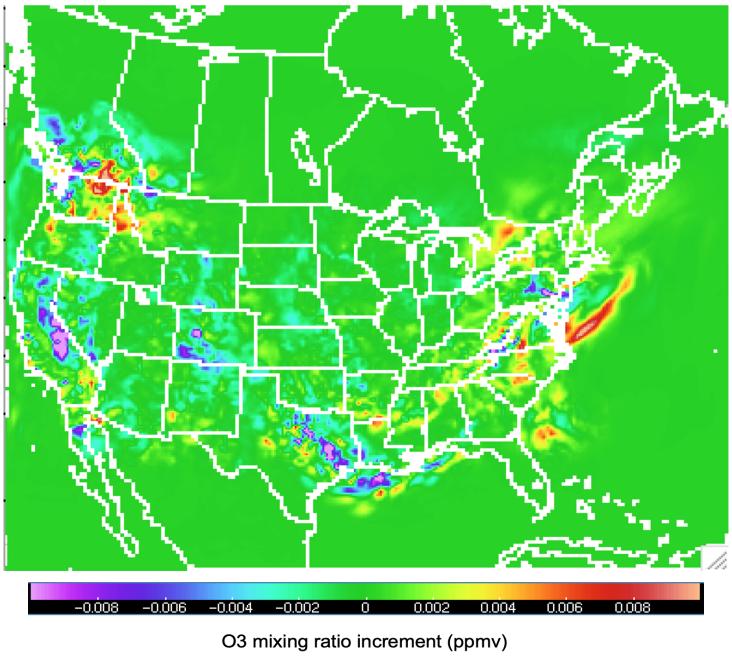

Fig. 4.14 The increment of surface O_3 mixing ratio after assimilating AirNow surface O_3 observations at 0000 UTC, June 3 2015.

The increment of the model spread is the difference of model spread between after (posterior) and before (prior) assimilation. If the increment of the model spread decreases, it means model ensemble members agree more with each other after assimilation. Fig. 4.15 shows the increment of surface O_3 mixing ratio model spread mean after assimilating AirNow surface O_3 mixing ratio observations at 0000 UTC, June 3 2015. The increment of the surface O_3 mixing ratio model spread mean decreases over the eastern, southeastern, and northwestern U.S., which means that after assimilating AirNow surface O_3 mixing ratio observations, the model ensemble members agree more with each other over these regions. Since more AirNow monitoring stations are located in these regions, more observations are assimilated into the model to improve model forecasts. However, the model spread over the Midwestern U.S. does not change much. The increment of the surface O_3 mixing ratio spread mean is around 0.0 ppmv, which means that the assimilated AirNow surface O_3 mixing ratio does not improve model forecasts. The possible reasons are: (1)

The prior surface O_3 mixing ratio agrees well with the AirNow surface O_3 mixing ratio; (2) Not enough AirNow surface O_3 mixing ratio data is assimilated into model due to limited observations, or observations have bad data quality and the observation errors are very large. When WRF-Chem/DART assimilates them, most observations are rejected. So only a few observations are assimilated into the model.

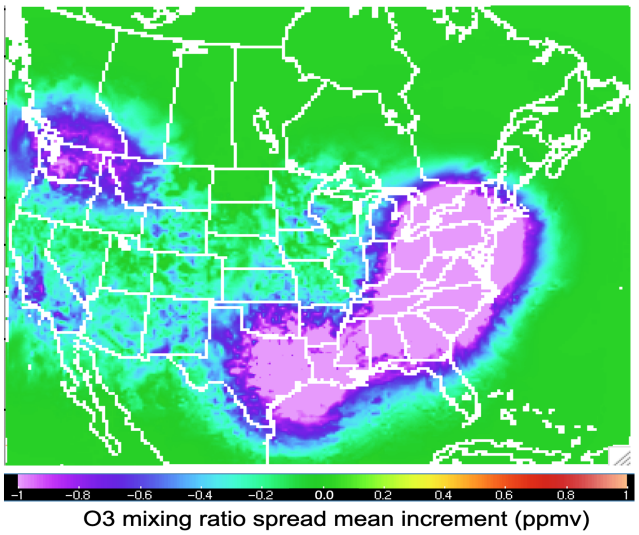

Fig. 4.15 The increment of surface O_3 mixing ratio model spread mean after assimilating AirNow surface O_3 mixing ratio observations at 0000 UTC, June 3 2015.

The time series of AirNow surface O_3 mixing ratio RMSE and model spread at the first model level shows how the assimilation performance evolves as time goes (Fig. 4.16). The posterior RMSE mean is 0.00885 ppmv, which is 0.00145 ppmv (14 %) lower than the prior RMSE mean which is 0.0103 ppmv. This means that the difference between posterior and observation is becoming smaller. In addition, the posterior model spread, which is 0.00233 ppmv, is 0.00183 ppmv (44 %) lower than the prior model spread which is 0.00416 ppmv.

Time evolutions of the number of possible and assimilated observations are also shown in Fig. 4.16. Their time evolutions follow a diurnal variation pattern which show less observations at night and more observations in the day. Similar pattern exists to the assimilated observations. The

assimilation of the AirNow surface O_3 mixing ratio started at 0000 UTC June 3 2015. During the model spin-up, the large difference between prior and observations prevents observations assimilated into the model. The number of assimilated observations is very low at the beginning of the assimilation. The observation rejection rate is very high due to the disagreement between prior and observations. As time goes, prior gradually agrees with observations thus more observations are assimilated into the model. At the end of the assimilation, almost all the possible observations are assimilated into the model (around 1200, Fig. 4.16).

The time evolution of RMSE shows RMSE decreases as time goes (Fig. 4.16). The large RMSE is observed at the beginning of the model spin-up, which reaches at 0.02 ppmv. As time goes, the RMSE decreases to 0.006 at the end of the assimilation and decreases by 70 %.

The posterior model spread mean is 0.00233 ppmv, 50 % lower than the prior model spread mean which is 0.00416 ppmv. From the time evolution of model spread, the model spread has an evident diurnal variation pattern, with high model spread during daytime and low model spread at night. The model spread diurnal pattern is opposite to the RMSE diurnal pattern, due to the high O_3 mixing ratio at daytime and low O_3 mixing ratio at night.

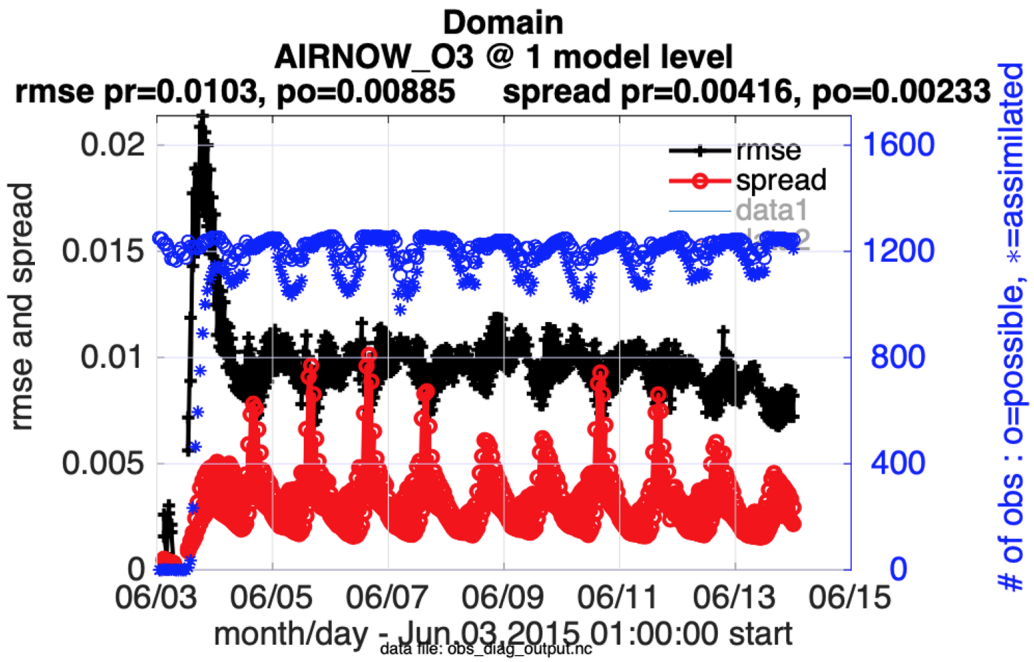

Fig. 4.16 Time series of AirNow surface O_3 mixing ratio RMSE and model spread at the first model level assimilated from WRF-Chem/DART. The left y axis is RMSE (red) and model spread (black), and the right y axis is the number of observations including the total number of observations (denoted as "o") and the number of assimilated observations (denoted as "*").

Similarly, the time evolution of the total spread decreases (Fig. 4.17). The prior total spread mean is 0.0105 ppmv, and the posterior total spread mean is 0.00987 ppmv, decreasing by 6 %.

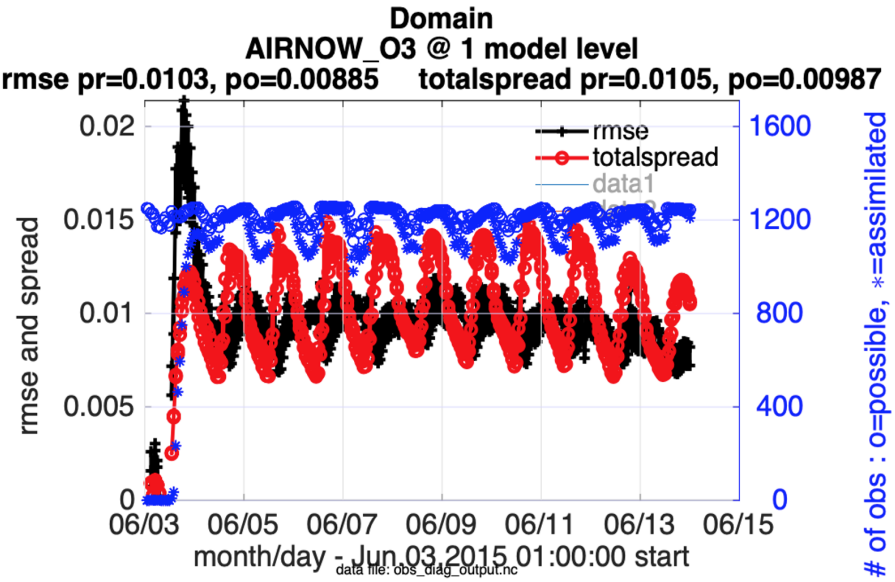

Fig. 4.17 Time series of AirNow surface O_3 mixing ratio RMSE and model spread at the first model level assimilated from WRF-Chem/DART. The left y axis is RMSE (red) and total spread (black), and the right y axis is the number of observations including the total number of observations (denoted as "o") and the number of assimilated observations (denoted as "*").

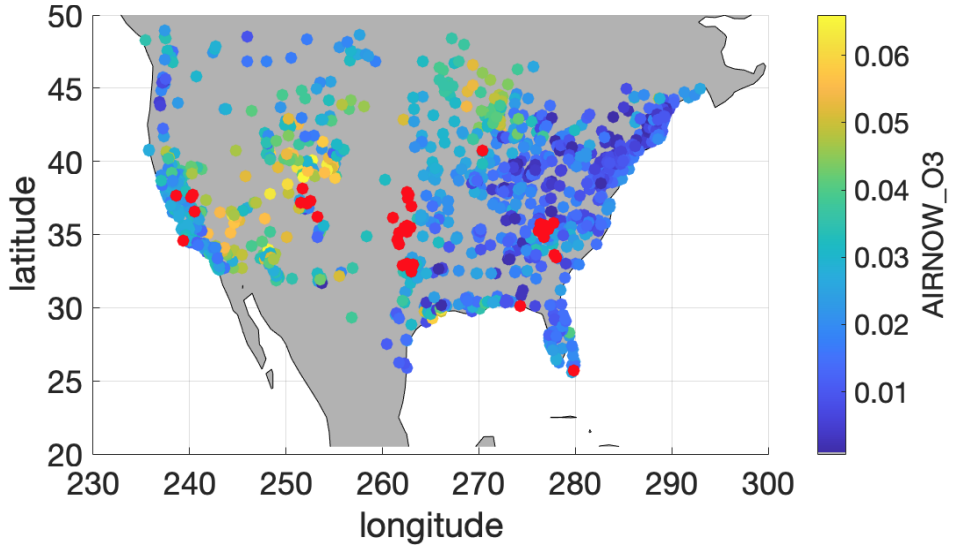

Fig. 4.18 2D color-coded scatter plot of AirNow surface O_3 mixing ratio in the U.S. at the assimilation window 0600-0700 UTC, June 03, 2015. The O_3 mixing ratio unit is ppmv. The red dots are selected observations corresponding to the red dots in Fig. 4.19 and Fig. 4.20 below.

Fig. 4.18 shows the spatial distribution of the AirNow observed surface O_3 mixing ratio, which is above 0.05 ppmv over the Mid-western U.S and around 0.01 ppmv over the eastern U.S. The selected red dots on the map are rejected observations with DART quality control flag of 7 (Rejected because of outlier threshold test). To track the rejected observations, Fig. 4.18, Fig. 4.19, and Fig. 4.20 are combined to show the locations of rejected observations, their DART quality control values, their sequence numbers, and the correlation between prior ensemble mean and AirNow observations.

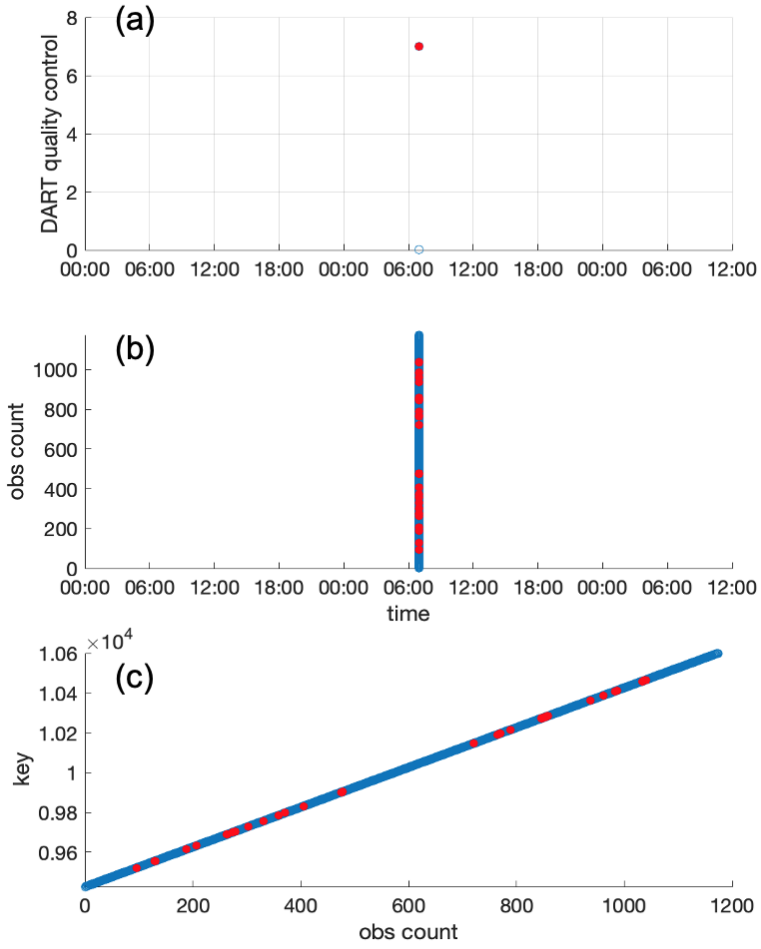

Fig. 4.19 (a) AirNow O_3 DART quality control values at the assimilation window 0600-0700 UTC, June 03, 2015. (b). The observation counts. (c). The key (sequence number) of AirNow O_3 as a

function of observation count. The red dots are the observations linked to the red dots in the Fig. 4.18 (above) and Fig. 4.19 (below).

The DART quality control values of the selected observations are 7 (red dots, Fig. 4.19a). It means that these observations were rejected because of the outlier threshold test. Fig. 4.19b and Fig. 4.19c show the positions of the selected observations in the observation sequence. It is easier to find where the observations are in the observation sequence file.

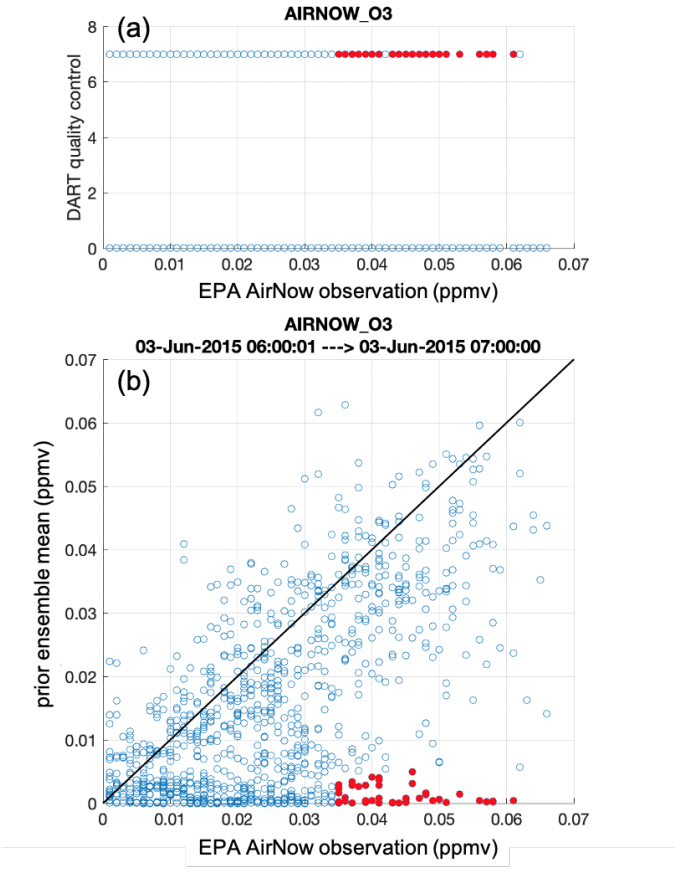

Fig. 4.20 (a) DART quality control flags of AirNow O_3 observation at the assimilation window 0600-0700 UTC, June 03, 2015. (b) The scatter plot of surface O_3 from AirNow observation and prior ensemble mean.

Fig. 4.20a shows the DART quality control as a function of the AirNow O_3 observation. The selected red dots are corresponding to the red dots in Fig. 4.18 and Fig. 4.19. Their DART

quality control values are 7. Fig. 4.20b shows the scatter plot of the prior ensemble mean and AirNow O_3 observation. The red dots indicate that their prior ensemble means are very small and their AirNow O_3 observations are large. The prior ensemble means underestimate AirNow O_3 observations. They were rejected because they are out of the outlier threshold, since observations are too larger than prior ensemble means.

4.4.4 TROPOZ lidar O_3 profile assimilation

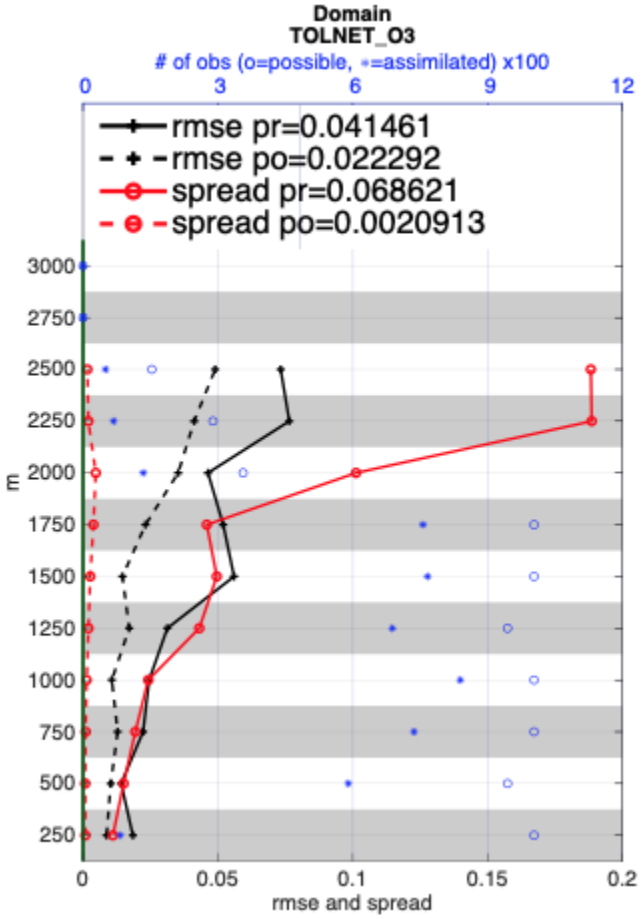

Fig. 4.21 Assimilated TROPOZ O_3 RMSE and model spread vertical profiles. The black solid profile is the prior RMSE, and the black dashed profile is the posterior RMSE. The red solid profile is the prior model spread, and the red dashed profile is the posterior model spread. The upper x

axis is the number of observations including the number of possible observations (denoted as “o”) and the number of assimilated observations (denoted as “*”).

The number of possible observations at the height from 250 m to 1750 m is around 1000 (Fig. 4.21). While the number of assimilated observations at 250 m is only about 100, which means only 10 % of observations were accepted and 90 % of observations were rejected by WRF-Chem/DART due to the high uncertainty of TROPOZ O_3 lidar near the surface. As the height increases, the number of assimilated observations increases to 700-800, which means about 70-80 % of observations were assimilated. The number of possible observations decreases from 1000 at 1750 m to around 300 from 2000 m to 2500 m, due to the cloud block/contamination.

The RMSE decreases after assimilating TROPOZ O_3 lidar vertical profiles. The prior RMSE mean is 0.041 ppmv, and the posterior RMSE mean decreases to 0.022 ppmv, reduced by 46 %. Model spread also decreases from the prior spread mean of 0.069 ppmv to the posterior spread mean of 0.0021, reduced by 97 %.

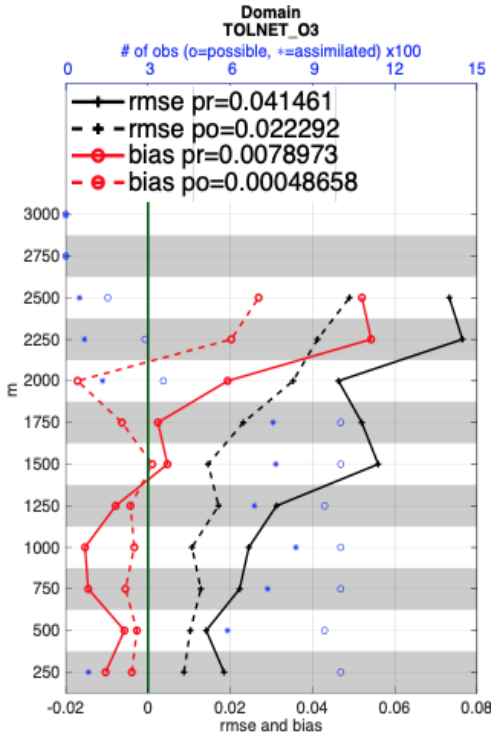

Fig. 4.22 Assimilated TROPOZ lidar O_3 RMSE and bias vertical profiles. The black solid profile is the prior RMSE, and the black dashed profile is the posterior RMSE. The red solid profile is the prior bias, and the red dashed profile is the posterior bias. The upper x axis is the number of observations including the number of possible observations (denoted as "o") and the number of assimilated observations (denoted as "*"). The vertical green line represents the zero RMSE and bias.

Aside from RMSE profiles, Fig. 4.22 shows the prior and posterior O_3 bias profile. The posterior bias is smaller than the prior bias below 1500 m, which means the model forecast is closer to the observation after assimilating TROPOZ O_3 profiles. The prior bias mean is 0.008 ppmv and the posterior bias mean is 0.0005 ppmv, reduced by 93 %.

In summary, the posterior RMSE, spread, and bias show that TROPOZ O_3 profiles were successfully assimilated into the WRF-Chem/DART. After assimilation, the analysis agrees with the observations. After assimilating TROPOZ O_3 vertical profiles, the WRF-Chem O_3 mixing ratio analysis is close to the observations (Fig. 4.23), as shown by the posterior RMSE. The WRF-Chem O_3 mixing ratio analysis has decreased significantly, comparing with the one without assimilating TROPOZ O_3 vertical profiles (Fig. 3.7). The WRF-Chem O_3 mixing ratio analysis is also compared with the independent observations from ozonesonde (Fig. 4.24). The O_3 mixing ratios agree well between analysis and ozonesonde.

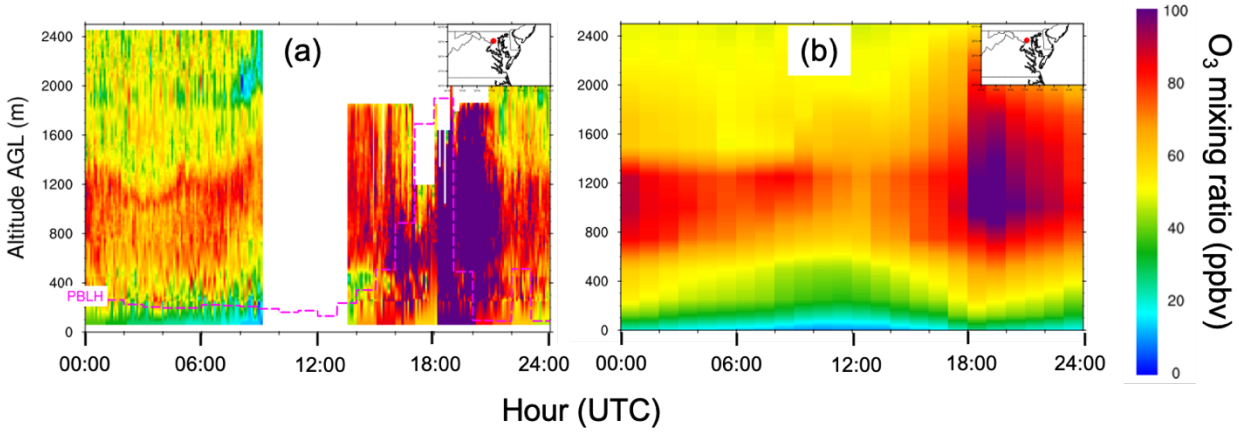

Fig. 4.23 O_3 mixing ratio vertical profile time series on 12 June 2015. (a) TROPOZ O_3 lidar; (b) WRF-Chem after assimilating TROPOZ O_3 vertical profiles.

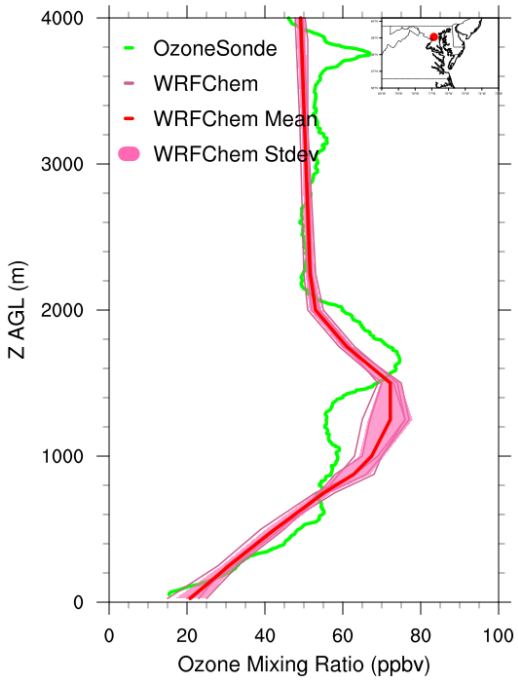

Fig. 4.24 O_3 mixing ratio vertical profiles of WRF-Chem analysis, ozonesonde (thick green curve) at 0800 UTC 12 June 2015. The WRF-Chem O_3 mixing ratio analysis profile mean and standard deviation are shown as a red thick curve and shade, respectively. The upper right inserted map shows the location of the Beltsville site (red dot).

4.5 Conclusions and summaries

In this study, we assimilate EPA AirNow surface O_3 observations and TROPOZ ground-based lidar O_3 vertical profile into the WRF-Chem/DART data assimilation system. We focus on a Canadian wildfire event in June 2015 to study the smoke impact on the local air quality over the Baltimore-Washington D.C. metropolitan region. This is the first attempt to assimilate TROPOZ O_3 lidar measurements into the WRF-Chem/DART. To better assimilate O_3 observations, the meteorological observations from aircraft, radiosonde, and satellites are also assimilated simultaneously. The meteorological initial conditions are from GFS and chemical initial conditions are from CAM-Chem. The emission datasets include anthropogenic emissions from NEI2011, biogenic emissions from MEGAN, and fire emissions from FINN.

The assimilated meteorological fields include horizontal wind and temperature from aircraft observations, horizontal wind, specific humidity, and temperature from radiosonde, horizontal wind from GOES satellite. Both RMSE and model spread decrease after assimilating these meteorological fields. For instance, the time evolution of horizontal wind RMSE shows that the prior RMSE is 3.22 ms^{-1} and the posterior RMSE decreases to 1.63 ms^{-1} after assimilating radiosonde horizontal wind.

The AirNow surface O_3 observations and TROPOZ O_3 lidar vertical profiles are successfully assimilated into WRF-Chem/DART. The AirNow stations map shows the inhomogeneous distribution over the U.S. More AirNow stations are located over the eastern U.S. while less stations at Midwest and west. This inhomogeneous hirontal distribution determines the assimilation performance of AirNow surface O_3 observations. The increments from both ensemble mean and inflation mean show the assimilation of AirNow surface O_3 observations has more impacts over the eastern U.S. The time evolution of surface O_3 RMSE indicates that the surface

O_3 RMSE decreases from 0.0103 ppmv of the prior to 0.00885 ppmv of the posterior. The RMSE reduction is about 20 %. Meanwhile, the prior model spread is 0.00416 ppmv and the posterior model spread decreases to 0.00233 ppmv. The model spread decreases by 50 % after assimilation. Similarly, the total spread decreases from 0.0105 ppmv to 0.00987 ppmv, reducing 6 %.

The assimilation of TROPOZ O_3 lidar vertical profiles also reduces the vertical profiles of O_3 RMSE, model spread, and bias. The prior RMSE is 0.041 ppmv and posterior RMSE decreases to 0.022 ppmv, about 48 % reduction. The model spread decreases from 0.007 ppmv of the prior to 0.002 ppmv of the posterior. Similarly, the bias decreases from 0.008 ppmv to 0.0005 ppmv.

In summary, both meteorological and chemical observations are successfully assimilated into the WRF-Chem/DART model. The statistical parameters show that the impact of assimilation is significant. Unfortunately, no ozonesonde observation is available on June 13 & 14, which could be used to verify the O_3 forecast after assimilating AirNow surface O_3 and TROPOZ O_3 vertical profiles.

Reference

Asch, M., Bocquet, M., & Nodet, M. (2016). Data assimilation: methods, algorithms, and applications. Society for Industrial and Applied Mathematics.

Anderson, D. C., Loughner, C. P., Diskin, G., Weinheimer, A., Canty, T. P., Salawitch, R. J., ... and Dickerson, R. R.: Measured and modeled CO and NOy in DISCOVER-AQ: An evaluation of emissions and chemistry over the eastern US. Atmospheric environment, 96, 78-87. https://doi.org/10.1016/j.atmosenv.2014.07.004, 2014.

Anderson, J., Hoar, T., Raeder, K., Liu, H., Collins, N., Torn, R., & Avellano, A. (2009). The data assimilation research testbed: A community facility. Bulletin of the American Meteorological Society, 90(9), 1283-1296, https://doi.org/10.1175/2009BAMS2618.1.

Anderson, J. L. (2001). An ensemble adjustment Kalman filter for data assimilation. Monthly weather review, 129(12), 2884-2903. https://doi.org/10.1175/1520-0493(2001)129 <2884:AEAKFF>2.0.CO;2

Anderson, J. L. (2020). A Marginal Adjustment Rank Histogram Filter for Non-Gaussian Ensemble Data Assimilation. Monthly Weather Review, 148(8), 3361-3378, https://doi.org/10.1175/MWR-D-19-0307.1.

Andreae, M. O., and Merlet P.: Emissions of trace gases and aerosols from biomass burning, *Global Biogeochem. Cycles*, 15, 955–966, https://doi:10.1029/2000-GB001382, 2001.

Arellano Jr., A. F., Raeder, K., Anderson, J. L., Hess, P. G., Emmons, L. K., Edwards, D. P., Pfister, G. G., Campos, T. L., and Sachse, G. W.: Evaluating model performance of an ensemble-based chemical data assimilation system during INTEX-B field mission, Atmos. Chem. Phys., 7, 5695–5710, https://doi.org/10.5194/acp-7-5695-2007, 2007.

Barker, D., Huang, X. Y., Liu, Z., Auligné, T., Zhang, X., Rugg, S., ... & Zhang, X. (2012). The weather research and forecasting model's community variational/ensemble data assimilation system: WRFDA. Bulletin of the American Meteorological Society, 93(6), 831-843. https://doi.org/10.1175/BAMS-D-11-00167.1

Berkoff, T., Sullivan, J., Pippin, M. R., Gronoff, G., Knepp, T. N., Twigg, L., and Nino, L.: Overview of the Ozone Water-Land Environmental Transition Study: Summary of Observations and Initial Results. AGU Fall Meeting, 11-15 December 2017.

Blaylock, B. K., Horel, J. D., and Crosman, E. T.: Impact of lake breezes on summer ozone concentrations in the Salt Lake valley. Journal of Applied Meteorology and Climatology, 56(2), 353-370. https://doi.org/10.1175/JAMC-D-16-0216.1, 2017.

Bocquet, M., Elbern, H., Eskes, H., Hirtl, M., Žabkar, R., Carmichael, G. R., Flemming, J., Inness, A., Pagowski, M., Pérez Camaño, J. L., Saide, P. E., San Jose, R., Sofiev, M., Vira, J., Baklanov, A., Carnevale, C., Grell, G., and Seigneur, C.: Data assimilation in atmospheric chemistry models: current status and future prospects for coupled chemistry meteorology models, Atmos. Chem. Phys., 15, 5325–5358, https://doi.org/10.5194/acp-15-5325-2015, 2015.

Bowman, K. W.: Toward the next generation of air quality monitoring: Ozone. Atmospheric environment, 80, 571-583, https://doi.org/10.1016/j.atmosenv.2013.07.007, 2013.

Brasseur, G. P., and Jacob, D. J.: Modeling of atmospheric chemistry. Cambridge University Press, United States, 2017.

Brey, S. J., and Fischer, E. V.: Smoke in the city: how often and where does smoke impact summertime ozone in the United States?. Environmental science & technology, 50(3), 1288-1294, https://doi.org/10.1021/acs.est.5b05218, 2016.

Brook, J. R., Makar, P. A., Sills, D. M. L., Hayden, K. L., and McLaren, R.: Exploring the nature of air quality over southwestern Ontario: main findings from the Border Air Quality and Meteorology Study. Atmospheric Chemistry and Physics, 13(20), 10461-10482. https://doi.org/10.5194/acp-13-10461-2013, 2013.

Caicedo, V., Delgado, R., Sakai, R., Knepp, T., Williams, D., Cavender, K., Lefer, B. Szykman, J.: An automated common algorithm for planetary boundary layer retrievals using aerosol lidars in support of the U.S. EPA Photochemical Assessment Monitoring Stations Program, J. Atmos. Oceanic Technol., 37 (10), 1847-1864, https://doi.org/10.1175/JTECH-D-20-0050.1, 2020.

Campbell, J. R., Ge, C., Wang, J., Welton, E. J., Bucholtz, A., Hyer, E. J., ... and Lolli, S.: Applying advanced ground-based remote sensing in the Southeast Asian maritime continent to characterize regional proficiencies in smoke transport modeling. Journal of Applied Meteorology and Climatology, 55(1), 3-22, https://doi.org/10.1175/JAMC-D-15-0083.1, 2016.

Camuffo, D.: Microclimate for cultural heritage: conservation, restoration, and maintenance of indoor and outdoor monuments. Elsevier, 2013.

Canadian Interagency Forest Fire Centre.: http://www. ciffc.ca (accessed August 10, 2020).

Carmichael, G. R., Sandu, A., Chai, T., Daescu, D. N., Constantinescu, E. M., & Tang, Y. (2008). Predicting air quality: Improvements through advanced methods to integrate models and measurements. Journal of Computational Physics, 227(7), 3540-3571. https://doi.org/10.1016/j.jcp.2007.02.024.

Carroll, B. J., Demoz, B. B., and Delgado, R.: An overview of low-level jet winds and corresponding mixed layer depths during PECAN. Journal of Geophysical Research: Atmospheres, 124(16), 9141-9160. https://doi.org/10.1029/2019JD030658, 2019.

Chai, T., Carmichael, G. R., Tang, Y., Sandu, A., Hardesty, M., Pilewskie, P., Whitlow, S., Browell, E. V., Avery, M. A., Nédélec, P., Merrill, J. T., Thompson, A. M., and Williams, E.: Four di- mensional data assimilation experiments with International Con- sortium for Atmospheric Research on Transport and Transfor- mation ozone measurements, J. Geophys. Res., 112, D12S15, https://doi.org/10.1029/2006JD007763, 2007.

Chang, W., Heikes, B. G., and Lee, M.: Ozone deposition to the sea surface: chemical enhancement and wind speed dependence. Atmospheric Environment, 38(7), 1053-1059, https://doi.org/10.1016/j.atmosenv.2003.10.050, 2004.

Cohen, A. E., Cavallo, S. M., Coniglio, M. C., and Brooks, H. E.: A review of planetary boundary layer parameterization schemes and their sensitivity in simulating southeastern US cold season severe weather environments. Weather and forecasting, 30(3), 591-612, https://doi.org/10.1175/WAF-D-14-00105.1, 2015.

Colarco, P. R., Schoeberl, M. R., Doddridge, B. G., Marufu, L. T., Torres, O., and Welton, E. J.: Transport of smoke from Canadian forest fires to the surface near Washington, DC: Injection height, entrainment, and optical properties. Journal of Geophysical Research: Atmospheres, 109(D6), https://doi.org/10.1029/2003JD004248, 2004.

Cooper, O. R., Langford, A. O., Parrish, D. D., and Fahey, D. W.: Challenges of a lowered US ozone standard. Science, 348(6239), 1096-1097. https://doi.org/10.1126/science.aaa5748, 2015.

Crawford, J. H., and Pickering, K. E.: DISCOVER-AQ: Advancing strategies for air quality observations in the next decade. Environ. Manage, 4-7, 2014.

Crosman, E. T. and Horel, J. D.: Sea and lake breezes: A review of numerical studies. Boundary-layer meteorology, 137(1), 1-29. https://doi.org/10.1007/s10546-010-9517-9, 2010.

Crutzen, P. J., Heidt, L. E., Krasnec, J. P., Pollock, W. H., and Seiler, W.: Biomass burning as a source of atmospheric gases CO, H2, N2O, NO, CH3Cl and COS. Nature, 282(5736), 253, https://doi.org/10.1038/282253a0, 1979.

Crutzen, P. J., and Andreae, M. O.: Biomass burning in the tropics: Impact on atmospheric chemistry and biogeochemical cycles. Science, 250(4988), 1669-1678, https://doi.org/10.1126/science.250.4988.1669, 1990.

Daley, R. (1991). Atmospheric data analysis (No. 2). Cambridge university press.

Daum, P. H., Kleinman, L. I., Springston, S. R., Nunnermacker, L. J., Lee, Y. N., Weinstein-Lloyd, J., ... and Berkowitz, C. M.: Origin and properties of plumes of high ozone observed during the Texas 2000 Air Quality Study (TexAQS 2000). Journal of Geophysical Research: Atmospheres, 109(D17). https://doi.org/10.1029/2003JD004311, 2004.

DeBell, L. J., Talbot, R. W., Dibb, J. E., Munger, J. W., Fischer, E. V., and Frolking, S. E.: A major regional air pollution event in the northeastern United States caused by extensive forest fires in Quebec, Canada. Journal of Geophysical Research: Atmospheres, 109(D19), https://doi.org/10.1029/2004JD004840, 2004.

Dreessen, J., Sullivan, J., and Delgado, R.: Observations and impacts of transported Canadian wildfire smoke on ozone and aerosol air quality in the Maryland region on June 9–12, 2015. Journal of the Air & Waste Management Association, 66(9), 842-862, https://doi.org/10.1080/10962247.2016.1161674, 2016.

Dye, T., Chan A., Anderson, C. B., Strohm, D., Wayland, R., and White, J.: From raw air quality data to the nightly news: an overview of how EPA's AirNow program operates. In Sixth Conference on Atmospheric Chemistry. American Meteorological Society annual meeting, Seattle, Washington, United States, 12-16 January 2004.

Dye, T. S., Roberts P. T., and Korc M. E.: Observations of transport processes for ozone and ozone precursors during the 1991 Lake Michigan Ozone Study. J. Appl. Meteor., 34, 1877–1889. https://doi.org/10.1175/1520-0450(1995)034<1877:OOTPFO>2.0.CO;2, 1995.

El Gharamti, M., Raeder, K., Anderson, J., & Wang, X. (2019). Comparing adaptive prior and posterior inflation for ensemble filters using an atmospheric general circulation model. Monthly Weather Review, 147(7), 2535-2553.

Elbern, H., & Schmidt, H. (2001). Ozone episode analysis by four-dimensional variational chemistry data assimilation. Journal of Geophysical Research: Atmospheres, 106(D4), 3569-3590. https://doi.org/10.1029/2000JD900448.

Fast, J. D., Gustafson Jr, W. I., Easter, R. C., Zaveri, R. A., Barnard, J. C., Chapman, E. G., ... and Peckham, S. E.: Evolution of ozone, particulates, and aerosol direct radiative forcing in the vicinity of Houston using a fully coupled meteorology-chemistry-aerosol model. Journal of Geophysical Research: Atmospheres, 111(D21), https://doi.org/10.1029/2005JD006721, 2006.

Flynn, C. M., Pickering, K. E., Crawford, J. H., Weinheimer, A. J., Diskin, G., Thornhill, K. L., ... and Strode, S. A.: Variability of O_3 and NO2 profile shapes during DISCOVER-AQ: Implications for satellite observations and comparisons to model-simulated profiles. Atmospheric Environment, 147, 133-156, https://doi.org/10.1016/j.atmosenv.2016.09.068, 2016.

Foley, T., Betterton, E. A., Jacko, P. R., and Hillery, J.: Lake Michigan air quality: The 1994–2003 LADCO Aircraft Project (LAP). Atmospheric environment, 45(18), 3192-3202, 2011.

Forouzanfar, M. H., Afshin, A., Alexander, L. T., Anderson, H. R., Bhutta, Z. A., Biryukov, S., ... and Cohen, A. J.: Global, regional, and national comparative risk assessment of 79 behavioural, environmental and occupational, and metabolic risks or clusters of risks, 1990–2015: a systematic analysis for the Global Burden of Disease Study 2015. The Lancet, 388(10053), 1659-1724. https://doi.org/10.1016/S0140-6736(16)31679-8, 2016.

Freeborn, P. H., Wooster, M. J., Roy, D. P., and Cochrane, M. A.: Quantification of MODIS fire radiative power (FRP) measurement uncertainty for use in satellite-based active fire characterization and biomass burning estimation. Geophysical Research Letters, 41(6), 1988-1994. https://doi.org/10.1002/2013GL059086, 2014.

Gallagher, M. W., Beswick, K. M., and Coe, H.: Ozone deposition to coastal waters. Quarterly Journal of the Royal Meteorological Society, 127(572), 539-558, https://doi.org/10.1002/qj.49712757215, 2001.

Gan. R. W., Liu J., Ford B., O'Dell K., Vaidyanathan A., Wilson A., Volckens J., Pfister G., Fischer E. V., Pierce J. R., and Magzamen S.: The association between wildfire smoke exposure and asthma-specific medical care utilization in Oregon during the 2013 wildfire season. J. Expo. Sci. Environ. Epidemiol., https://doi.org/10.1038/s41370-020-0210-x, 2020.

Gillett, N. P., Weaver A. J., Zwiers F. W., and Flannigan M. D.: Detecting the effect of climate change on Canadian forest fires, *Geophys. Res. Lett.*, 31, L18211, https://doi.org/10.1029/2004GL020876, 2004.

Goldberg, D. L., Loughner, C. P., Tzortziou, M., Stehr, J. W., Pickering, K. E., Marufu, L. T., and Dickerson, R. R.: Higher surface ozone concentrations over the Chesapeake Bay than

over the adjacent land: Observations and models from the DISCOVER-AQ and CBODAQ campaigns. Atmospheric environment, 84, 9-19, https://doi.org/10.1016/j.atmosenv.2013.11.008, 2014.

Grell, G., Freitas, S. R., Stuefer, M., and Fast, J.: Inclusion of biomass burning in WRF-Chem: impact of wildfires on weather forecasts. Atmospheric Chemistry and Physics, 11(11). https://doi.org/10.5194/acp-11-5289-2011, 2011.

Grell G. A., Peckham S. E., Schmitz R., McKeen S. A., Frost G., Skamarock W. C., and Eder B.: Fully coupled online chemistry within the WRF model. *Atmospheric Environment*, 39: 6957–6975, https://doi.org/10.1016/j.atmosenv.2005.04.027, 2005.

Greeshma, M. M., Srinivas, C. V., Yesubabu, V., Naidu, C. V., Baskaran, R., & Venkatraman, B. (2015). Impact of local data assimilation on tropical cyclone predictions over the Bay of Bengal using the ARW model. In Annales Geophysicae (Vol. 33, No. 7, pp. 805-828). https://doi.org/10.5194/angeo-33-805-2015.

Guenther, A., Karl, T., Harley, P., Wiedinmyer, C., Palmer, P. I., & Geron, C. (2006). Estimates of global terrestrial isoprene emissions using MEGAN (Model of Emissions of Gases and Aerosols from Nature). Atmospheric Chemistry and Physics, 6(11), 3181-3210.

Hamill, T. M. (2001). Interpretation of rank histograms for verifying ensemble forecasts. Monthly Weather Review, 129(3), 550-560.

Hand, E.: China blamed for US ozone. Science, 6202: 1233, https://doi.org/10.1126/science.345.6202.1233, 2014.

He, H., Loughner, C. P., Stehr, J. W., Arkinson, H. L., Brent, L. C., Follette-Cook, M. B., ... and Diskin, G. S.: An elevated reservoir of air pollutants over the Mid-Atlantic States during the

2011 DISCOVER-AQ campaign: Airborne measurements and numerical simulations. Atmospheric environment, 85, 18-30, https://doi.org/10.1016/j.atmosenv.2013.11.039, 2014.

Hobbs, P. V., and Wallace J. M.: Atmospheric Science: An Introductory Survey. 2nd ed. Academic Press, 504 pp, 2006.

Hong S. Y. and Pan H. L.: Nonlocal boundary layer vertical diffusion in a medium-range forecast model. Mon. Weather Rev. 124: 2322–2339, https://doi.org/10.1175/1520-0493(1996)124<2322:NBLVDI>2.0.CO;2, 1996.

Hong S. Y., Noh Y., and Dudhia J.: A new vertical diffusion package with an explicit treatment of entrainment processes. Mon. Weather Rev. 134: 2318–2341, https://doi.org/10.1175/MWR3199.1, 2006.

Houtekamer, P. L., and Mitchell, H. L.: Data assimilation using an ensemble Kalman filter technique. Monthly Weather Review, 126(3), 796-811, https://doi.org/10.1175/1520-0493(1998)126<0796:DAUAEK>2.0.CO;2, 1998.

Houtekamer, P. L. and Mitchell, H. L.: A sequential ensemble Kalman filter for atmospheric data assimilation, Mon. Weather Rev., 129, 123–137, https://doi.org/10.1175/1520-0493(2001)129<0123:ASEKFF>2.0.CO;2, 2001.

Hu, X. M., Doughty, D. C., Sanchez, K. J., Joseph, E., and Fuentes, J. D.: Ozone variability in the atmospheric boundary layer in Maryland and its implications for vertical transport model. Atmospheric Environment, 46, 354-364, https://doi.org/10.1016/j.atmosenv.2011.09.054, 2012.

Hu, X. M., Klein, P. M., Xue, M., Zhang, F., Doughty, D. C., Forkel, R., ... and Fuentes, J. D.: Impact of the vertical mixing induced by low-level jets on boundary layer ozone

concentration. Atmospheric Environment, 70, 123-130, https://doi.org/10.1016/j.atmosenv.2012.12.046, 2013.

Hu, X. M., Klein, P. M., and Xue, M.: Evaluation of the updated YSU planetary boundary layer scheme within WRF for wind resource and air quality assessments. Journal of Geophysical Research: Atmospheres, 118(18), https://doi.org/10.1002/jgrd.50823, 2013.

Hu, X. M., Nielsen-Gammon, J. W., and Zhang, F.: Evaluation of three planetary boundary layer schemes in the WRF model. Journal of Applied Meteorology and Climatology, 49(9), 1831-1844. https://doi.org/10.1175/2010JAMC2432.1, 2010.

Iacono, M. J., Delamere J. S., Mlawer E. J., Shephard M. W., Clough S. A., and Collins W. D.: Radiative forcing by long-lived greenhouse gases: Calculations with the AER radiative transfer models, *J. Geophys. Res.*, 113, D13103, https://doi.org/10.1029/2008JD-009944, 2008.

IPCC, Climate Change 2013: The Physical Science Basis. Contribution of Working Group I to the Fourth Assessment. Report of the Intergovernmental Panel on Climate Change. Cambridge University Press, Cambridge, United Kingdom and New York, NY, USA, 1552pp, edited, 2013.

Jacob, D.: Introduction to atmospheric chemistry. Princeton University Press, United States, 1999.

Janjić, Z. I.: The step-mountain coordinate: Physical package, Mon. Weather Rev., 118, 1429–1443, https://doi.org/10.1175/1520-0493(1990)118<1429:TSMCPP>2.0.CO;2, 1990.

Janjić, Z. I.: The step-mountain Eta coordinate model: Further developments of the convection, viscous sublayer, and turbulence closure schemes, Mon. Weather Rev., 122, 927–945, https://doi.org/10.1175/1520-0493(1994)122<0927:TSMECM>2.0.CO;2, 1994.

Janjić, Z. I.: Comments on “Development and evaluation of a convection scheme for use in climate models”. Journal of the Atmospheric Sciences, 57(21), 3686-3686, https://doi.org/10.1175/1520-0469(2000)057<3686:CODAEO>2.0.CO;2, 2000.

Jenkin, M. E. and Clemitshaw, K. C.: Ozone and other secondary photochemical pollutants: chemical processes governing their formation in the planetary boundary layer. Atmospheric Environment, 34(16), 2499-2527. https://doi.org/10.1016/S1352-2310(99)00478-1, 2000.

Jiang, Z., Liu, Z., Wang, T., Schartz, C. S., Lin, H.-C., and Jiang, F.: Probing into the impact of 3DVAR assimilation of surface PM10 observations over China using process analysis, J. Geophys. Res. Atmos., 118, 6738–6749, doi:10.1002/jgrd.50495, 2013.

Jiménez, P., Jorba, O., Parra, R., and Baldasano, J. M.: Evaluation of MM5-EMICAT2000-CMAQ performance and sensitivity in complex terrain: high-resolution application to the northeastern Iberian Peninsula. Atmospheric Environment, 40(26), 5056-5072. https://doi.org/10.1016/j.atmosenv.2005.12.060, 2006.

Karle, N. N., Mahmud, S., Sakai, R. K., Fitzgerald, R. M., Morris, V. R., and Stockwell, W. R.: Investigation of the Successive Ozone Episodes in the El Paso–Juarez Region in the Summer of 2017. Atmosphere, 11(5), 532, 2020.

Komhyr, W. D., Barnes R. A., Brothers G. B., Lathrop J. A., and Opperman D. P.: Electrochemical concentration cell ozonesonde performance evaluation during STOIC 1989, J. Geophys. Res., 100, 9231–9244, https://doi.org/10.1029/94JD02175, 1995.

Koshin, D., Sato, K., Miyazaki, K., & Watanabe, S.: An ensemble Kalman filter data assimilation system for the whole neutral atmosphere. Geoscientific Model Development, 13(7), 3145-3177, https://doi.org/10.5194/gmd-13-3145-2020, 2020.

Kunzli N., Avol E., Wu J., Gauderman W. J., Rappaport E., and Millstein J.: Health effects of the 2003 Southern California wildfires on children. Am J Respir Crit Care Med. 174:1221–1228, https://doi.org/10.1164/rccm.200604-519OC, 2006.

Levy, R. and co-authors: MODIS Atmosphere L2 Aerosol Product. NASA MODIS Adaptive Processing System, Goddard Space Flight Center, USA, 2015.

Lippmann, M.: Health effects of tropospheric ozone, Environmental Science & Technology, 25, 1954-1962, https://doi.org/10.1021/es00180a002, 1991.

Liu, X., Mizzi, A. P., Anderson, J. L., Fung, I. Y., & Cohen, R. C. (2017). Assimilation of satellite NO 2 observations at high spatial resolution using OSSEs. Atmospheric Chemistry and Physics, 17(11), 7067-7081. https://doi.org/10.5194/acp-17-7067-2017.

Liu, Y., Stanturf, J., and Goodrick, S.: Trends in global wildfire potential in a changing climate. Forest ecology and management, 259(4), 685-697. https://doi.org/10.1016/j.foreco.2009.09.002, 2010.

Liu, Z., Liu, Q., Lin, H.-C., Schwartz, C. S., Lee, Y.-H., and Wang, T.: Three-dimensional variational assimilation of MODIS aerosol optical depth: Implementation and application to a dust storm over East Asia, J. Geophys. Res., 116, D22306, https://doi.org/10.1029/2011JD016159, 2011.

LMOS 2017 Study Team: 2017 Lake Michigan Ozone Study (LMOS) Preliminary Finding Report, 2019.

Loughner, C. P., Allen, D. J., Pickering, K. E., Zhang, D. L., Shou, Y. X., and Dickerson, R. R.: Impact of fair-weather cumulus clouds and the Chesapeake Bay breeze on pollutant transport and transformation. Atmospheric environment, 45(24), 4060-4072. https://doi.org/10.1016/j.atmosenv.2011.04.003, 2011.

Loughner, C. P., Tzortziou, M., Follette-Cook, M., Pickering, K. E., Goldberg, D., Satam, C., ... and Diskin, G. S.: Impact of bay-breeze circulations on surface air quality and boundary layer export. Journal of Applied Meteorology and Climatology, 53(7), 1697-1713, https://doi.org/10.1175/JAMC-D-13-0323.1, 2014.

Lyons W.A. and Cole H.S.: Photochemical oxidant transport: mesoscale lake breeze and synoptic-scale aspects. Journal of Applied Meteorology 15 : 733 – 743. https://doi.org/10.1175/1520-0450(1976)015<0733:POTMLB>2.0.CO;2, 1976.

Lyons, W. A., Tremback, C. J., and Pielke, R. A.: Applications of the Regional Atmospheric Modeling System (RAMS) to provide input to photochemical grid models for the Lake Michigan Ozone Study (LMOS). Journal of Applied Meteorology, 34(8), 1762-1786, https://doi.org/10.1175/1520-0450(1995)034<1762:AOTRAM>2.0.CO;2, 1995.

Martineau Jr., R. and Novello, D.: The Clean Air Act handbook. Chicago, IL: American Bar Association, 1997.

McKeen, S. A., Wotawa, G., Parrish, D. D., Holloway, J. S., Buhr, M. P., Hübler, G., ... and Meagher, J. F.: Ozone production from Canadian wildfires during June and July of 1995. Journal of Geophysical Research: Atmospheres, 107(D14), https://doi.org/10.1029/2001JD000697, 2002.

Messina, P., D'Isodoro, M., Murizi, A., and Fierli, F.: Impact of assimilated observations on improving tropospheric ozone simu- lations, Atmos. Environ., 45, 6674–6681, https://doi.org/10.1016/j.atmosenv.2011.08.056, 2011.

Mizzi, A. P., Arellano Jr, A. F., Edwards, D. P., Anderson, J. L., & Pfister, G. G. (2016). Assimilating compact phase space retrievals of atmospheric composition with WRF-Chem/DART: a regional chemical transport/ensemble Kalman filter data assimilation system.

Geoscientific Model Development (Online), 9(3), 965-978. https://doi.org/10.5194/gmd-9-965-2016.

Mizzi, A. P., Edwards, D. P., & Anderson, J. L. (2018). Assimilating compact phase space retrievals (CPSRs): comparison with independent observations (MOZAIC in situ and IASI retrievals) and extension to assimilation of truncated retrieval profiles. Geoscientific Model Development, 11(9), 3727-3745. https://doi.org/10.5194/gmd-11-3727-2018.

Morris, G. A., Hersey, S., Thompson, A. M., Pawson, S., Nielsen, J. E., Colarco, P. R., ... and Johnson, B. J.: Alaskan and Canadian forest fires exacerbate ozone pollution over Houston, Texas, on 19 and 20 July 2004. Journal of Geophysical Research: Atmospheres, 111(D24), https://doi.org/10.1029/2006JD007090, 2006.

Mudway, I. S. and Kelly, F. J.: Ozone and the lung: a sensitive issue. Molecular aspects of medicine, 21(1-2), 1-48. https://doi.org/10.1016/S0098-2997(00)00003-0, 2000.

National Ambient Air Quality Standards (NAAQS) for Ozone (2015). US-EPA, https://www.epa.gov/ozone-pollution/2015-national-ambient-air-quality-standards-naaqs-ozone

National Centers for Environmental Prediction/National Weather Service/NOAA/U.S. Department of Commerce. 2015, updated daily. NCEP GFS 0.25 Degree Global Forecast Grids Historical Archive. Research Data Archive at the National Center for Atmospheric Research, Computational and Information Systems Laboratory. https://doi.org/10.5065/D65D8PWK. Accessed 07/21/2019.

Newchurch, M. J., Kuang, S., Leblanc, T., Alvarez, R. J., Langford, A. O., Senff, C. J., ... and Al-Saadi, J.: TOLNET–A Tropospheric Ozone Lidar Profiling Network for Satellite

Continuity and Process Studies. In EPJ Web of Conferences (Vol. 119, p. 20001). EDP Sciences, https://doi.org/10.1051/epjconf/201611920001, 2016.

Nowak, D. J., Crane, D. E., and Stevens, J. C.: Air pollution removal by urban trees and shrubs in the United States. Urban forestry & urban greening, 4(3-4), 115-123, https://doi.org/10.1016/j.ufug.2006.01.007, 2006.

Omar, A. H., Winker, D. M., Vaughan, M. A., Hu, Y., Trepte, C. R., Ferrare, R. A., ... and Kuehn, R. E.: The CALIPSO automated aerosol classification and lidar ratio selection algorithm. Journal of Atmospheric and Oceanic Technology, 26(10), 1994-2014, https://doi.org/10.1175/2009JTECHA1231.1, 2009.

Peckham, S. E., et al.: WRF/Chem version 3.7 user's guide. https://permanent.access.gpo.gov/gpo67735/ Users_guide.pdf, 2015.

Peterson, D., Wang, J., Ichoku, C. M., Hyer, E., and Ambrosia V.: A sub-pixel-based calculation of fire radiative power from MODIS observations: 1 Algorithm development and initial assessment, Remote Sens. Environ., 129, 262–279, https://doi.org/10.1016/j.rse.2012.10.036, 2013.

Pierce B.,, R. Kaleel, A. Dickens, T. Bertram, C. Stanier, D. Kenski, White Paper: Lake Michigan Ozone Study 2017 (LMOS 2017), https://www-air.larc.nasa.gov/missions/lmos/docs/Great_Lakes_Ozone_Study_White_Paper_Draft_v6.pdf

Pielke, R. A., Cotton, W. R., Walko, R. E. A., Tremback, C. J., Lyons, W. A., Grasso, L. D., ... and Copeland, J. H.: A comprehensive meteorological modeling system—RAMS. Meteorology and atmospheric Physics, 49(1-4), 69-91. https://doi.org/10.1007/BF01025401, 1992.

Pleim, J. E.: A combined local and nonlocal closure model for the atmospheric boundary layer. Part I: Model description and testing. Journal of Applied Meteorology and Climatology, 46(9), 1383-1395, https://doi.org/10.1175/JAM2539.1, 2007a.

Pleim, J. E.: A combined local and nonlocal closure model for the atmospheric boundary layer. Part II: Application and evaluation in a mesoscale meteorological model. Journal of Applied Meteorology and Climatology, 46(9), 1396-1409, https://doi.org/10.1175/JAM2534.1, 2007b.

Poterjoy, J.: A localized particle filter for high-dimensional nonlinear systems. Monthly Weather Review, 144(1), 59-76, https://doi.org/10.1175/MWR-D-15-0163.1, 2016.

PORG, U.: Ozone in the United Kingdom. United Kingdom Photochemical Oxidants Review Group Report, Department of the Environment, London, 1997.

Roberts, J., Trainer, M., Murphy, D., Brown, S., Brewer, A., Gao, R.S., and Fahey, D. Fire Influence on Regional to Global Environments and Air Quality (FIREX-AQ). Available online: https://www.esrl.noaa.gov/csd/projects/firex-aq/whitepaper.pdf (accessed on 20 July 2020).

Seinfeld, J. H., and Pandis, S. N.: Atmospheric chemistry and physics: from air pollution to climate change. John Wiley & Sons, United States, 2016.

Schoennagel, T., Balch, J. K., Brenkert-Smith, H., Dennison, P. E., Harvey, B. J., Krawchuk, M. A., ... and Turner, M. G.: Adapt to more wildfire in western North American forests as climate changes. Proceedings of the National Academy of Sciences, 114(18), 4582-4590. https://doi.org/10.1073/pnas.1617464114, 2017.

Schwartz, C. S., Liu, Z., Lin, H.-C., and Cetola, J. D.: Assimilating aerosol observations with a “hybrid” variational-ensemble data assimilation system, J. Geophys. Res. Atmos., 119, 4043–4069, https://doi.org/10.1002/2013JD020937, 2014.

Skamarock, W., and Coauthors: A description of the Advanced Research WRF version 3. NCAR Tech. Note NCAR/TN-475+STR, United States, http://dx.doi.org/10.5065/D68S4MVH, 2008.

Spracklen, D. V., Mickley, L. J., Logan, J. A., Hudman, R. C., Yevich, R., Flannigan, M. D., and Westerling, A. L.: Impacts of climate change from 2000 to 2050 on wildfire activity and carbonaceous aerosol concentrations in the western United States, *J. Geophys. Res*., 114, D20301, https://doi.org/10.1029 /2008JD 010966, 2009.

Stauffer, R. M., Thompson, A. M., Martins, D. K., Clark, R. D., Goldberg, D. L., Loughner, C. P., ... and Tzortziou, M. A.: Bay breeze influence on surface ozone at Edgewood, MD during July 2011. Journal of atmospheric chemistry, 72(3-4), 335-353. https://doi.org/10.1007/s10874-012-9241-6, 2015.

Stull, R. B.: An introduction to boundary layer meteorology (Vol. 13). Springer Science & Business Media, United States, 1988.

Su, W., Liu, C., Hu, Q., Fan, G., Xie, Z., Huang, X., ... & Liu, J.: Characterization of ozone in the lower troposphere during the 2016 G20 conference in Hangzhou. Scientific reports, 7(1), 1-11, https://doi:10.1038/s41598-017-17646-x, 2017.

Sullivan, J. T.: Improving the Current Understanding of the Evolution and Vertical Processes of Tropospheric Ozone Using a Ground Based Differential Absorption Lidar. University of Maryland, Baltimore County, 2015.

Sullivan, J. T., Berkoff, T., Gronoff, G., Knepp, T., Pippin, M., Allen, D., ... & McGee, T. J. (2019). The ozone water–land environmental transition study: An innovative strategy for understanding Chesapeake Bay pollution events. Bulletin of the American Meteorological Society, 100(2), 291-306.

Sullivan, J. T., McGee, T. J., Sumnicht, G. K., Twigg, L. W., and Hoff, R. M.: A mobile differential absorption lidar to measure sub-hourly fluctuation of tropospheric ozone profiles in the Baltimore–Washington, D.C. region. *Atmos. Meas. Tech.*, 7, 3529–3548, doi:https://doi.org/10. 5194/amt-7-3529-2014, 2014.

Sullivan, J. T., Rabenhorst, S. D., Dreessen, J., McGee, T. J., Delgado, R., Twigg, L., & Sumnicht, G. 2017. Lidar observations revealing transport of O_3 in the presence of a nocturnal low-level jet: Regional implications for "next-day" pollution. Atmospheric environment, 158, 160-171.

The NCAR Command Language (Version 6.6.2) [Software].: Boulder, Colorado: UCAR/NCAR/CISL/ TDD. http://dx.doi.org/10.5065/D6WD3XH5, 2019.

Van Leeuwen, P. J. (2009). Particle filtering in geophysical systems. Monthly Weather Review, 137(12), 4089-4114, https://doi.org/10.1175/2009MWR2835.1.

Wang, J., Ge, C., Yang, Z., Hyer, E. J., Reid, J. S., Chew, B. N., Mahmud, M., Zhang, Y., and Zhang, M.: Mesoscale modeling of smoke transport over the Southeast Asian Maritime Continent: Interplay of sea breeze, trade wind, typhoon, and topography, Atmos. Res., 122, 486–503, https://doi.org/10.1016/j.atmosres.2012.05.009, 2013.

Welton, E. J., Campbell, J. R., Spinhirne, J. D., and Scott, V. S.: Global monitoring of clouds and aerosols using a network of micropulse lidar systems. In Lidar Remote Sensing for Industry and Environment Monitoring (Vol. 4153, pp. 151-159). International Society for Optics and Photonics, February 2001.

Wesely, M. L., and Hicks, B. B.: A review of the current status of knowledge on dry deposition. Atmospheric environment, 34(12-14), 2261-2282, https://doi.org/10.1016/S1352-2310(99)00467-7, 2000.

Westerling A. L., Hidalgo, H. G., Cayan, D. R., and Swetnam, T.W.: Warming and earlier spring increases western US forest wildfire activity. *Science* 313: 940–943, https://doi.org/10.1126/science.1128834, 2006.

Wotawa, G., and Trainer, M.: The influence of Canadian forest fires on pollutant concentrations in the United States. Science, 288(5464), 324-328, https://doi.org/10.1126/science.288.5464.324, 2000.

Wu, Y., Arapi, A., Huang, J., Gross, B., and Moshary, F.: Intra-continental wildfire smoke transport and impact on local air quality observed by ground-based and satellite remote sensing in New York City. Atmospheric Environment, 187, 266-281, https://doi.org/10.1016/j.atmosenv.2018.06.006, 2018.

Xu, X., Wang, J., Henze, D. K., Qu, W., & Kopacz, M. (2013). Constraints on aerosol sources using GEOS-Chem adjoint and MODIS radiances, and evaluation with multisensor (OMI, MISR) data. Journal of Geophysical Research: Atmospheres, 118(12), 6396-6413, https://doi.org/10.1002/jgrd.50515.

Yang, Z., Wang, J., Ichoku, C., Hyer, E., and Zeng, J.: Mesoscale modeling and satellite observation of transport and mixing of smoke and dust particles over northern sub-Saharan African region, *J. Geophys. Res. Atmos*., 118, 12,139–12,157, https://doi.org/10.1002/2013JD020644, 2013.

Young, J. A.: Static stability, J.R. Holton, J.A. Curry, J.A. Pyle (Eds.), Encyclopaedia of Atmospheric Sciences, v.5, Academic Press (2003), pp. 2114-2120, 2003.

Zaveri, R. A., Easter R. C., Fast J. D., and Peters L. K.: Model for Simulating Aerosol Interactions and Chemistry (MOSAIC), J. Geophys. Res., 113, D13204, https://doi:10.1029/2007JD 008782, 2008.

Zaveri, R. A., and Peters, L. K.: A new lumped structure photochemical mechanism for large-scale applications, *J. Geophys. Res*., 104, 30387–30415, https://doi.org/10.1029/1999JD900876, 1999.

Zaveri, R. A., Easter, R. C., Fast, J. D., and Peters, L. K.: Model for Simulating Aerosol Interactions and Chemistry (MOSAIC), *J. Geophys. Res.*, 113, D13204, https://doi.org/10.1029/2007JD 008782, 2008.

Zhang, R., Lei, W., Tie, X., and Hess, P.: Industrial emissions cause extreme urban ozone diurnal variability. Proceedings of the National Academy of Sciences of the United States of America, 101(17), 6346-6350, https://doi.org/10.1073/pnas.0401484101, 2004.

Zhang, Y., Dubey, M. K., Olsen, S. C., Zheng, J., and Zhang, R.: Comparisons of WRF/Chem simulations in Mexico City with ground-based RAMA measurements during the 2006-MILAGRO, Atmos. Chem. Phys., 9, 3777-3798, https://doi.org/10.5194/acp-9-3777-2009, 2009.